QCD2019 Workshop Summary

S.J. Brodsky,[1] V.D. Burkert,[2] D.S. Carman,[2] J.P. Chen,[2] Z.-F. Cui,[3,4] M. Döring,[2,5] H.G. Dosch,[6] J. Draayer,[7] L. Elouadrhiri,[2] D.I. Glazier,[8] A.N. Hiller Blin,[2] T. Horn,[9] K. Joo,[10] H.C. Kim,[11] V. Kubarovsky,[2] Y. Lu[3,4] W. Melnitchouk,[2] C. Mezrag,[12] V.I. Mokeev,[2] J.W. Qiu,[2] M. Radici,[13] D. Richards,[2] C.D. Roberts,[3,4] J. Rodríguez-Quintero,[14] J. Segovia,[4,15] A.P. Szczepaniak,[2,16] G.F. de Téramond,[17] D. Winney[16]

[1] *SLAC National Accelerator Laboratory, Stanford University, Stanford, CA 94039*
[2] *Thomas Jefferson National Accelerator Laboratory, Newport News, VA 23606*
[3] *School of Physics, Nanjing University, Nanjing, Jiangsu 210093, China*
[4] *Institute for Nonperturbative Physics, Nanjing University, Nanjing, Jiangsu 210093, China*
[5] *Institute for Nuclear Studies and Department of Physics, The George Washington University, Washington, DC 20052*
[6] *Institut für Theoretische Physik, Philosophenweg 16, 69120 Heidelberg, Germany*
[7] *Louisiana State University, Baton Rouge, LA 70803*
[8] *University of Glasgow, Glasgow G12 8QQ, United Kingdom*
[9] *The Catholic University of America, Washington, DC 20064*
[10] *The University of Connecticut, Storrs, CT 06269*
[11] *Department of Physics, Inha University, 22212 Incheon, The Republic of Korea*
[12] *IRFU, CEA, Université Paris-Saclay, F-91191 Gif-sur-Yvette, France*
[13] *INFN Sezione di Pavia, via Bassi 6, I-27100 Pavia, Italy*
[14] *Department of Integrated Sciences and Center for Advanced Studies in Physics, Mathematics and Computation; University of Huelva, E-21071 Huelva; Spain*
[15] *Dpto. Sistemas Físicos, Químicos y Naturales, Univ. Pablo de Olavide, E-41013 Sevilla, Spain*
[16] *Indiana University, Bloomington, IN 47405 and*
[17] *Universidad de Costa Rica, 11501 San Pedro de Montes de Oca, Costa Rica*

(Dated: June 10, 2020)

The topical workshop *Strong QCD from Hadron Structure Experiments* took place at Jefferson Lab from Nov. 6-9, 2019. Impressive progress in relating hadron structure observables to the strong QCD mechanisms has been achieved from the *ab initio* QCD description of hadron structure in a diverse array of methods in order to expose emergent phenomena via quasi-particle formation. The wealth of experimental data and the advances in hadron structure theory make it possible to gain insight into strong interaction dynamics in the regime of large quark-gluon coupling (the strong QCD regime), which will address the most challenging problems of the Standard Model on the nature of the dominant part of hadron mass, quark-gluon confinement, and the emergence of the ground and excited state hadrons, as well as atomic nuclei, from QCD. This workshop aimed to develop plans and to facilitate the future synergistic efforts between experimentalists, phenomenologists, and theorists working on studies of hadron spectroscopy and structure with the goal to connect the properties of hadrons and atomic nuclei available from data to the strong QCD dynamics underlying their emergence from QCD. These results pave the way for a future breakthrough extension in the studies of QCD with an Electron-Ion Collider in the U.S.

CONTENTS

I. Preface 3

II. Executive Summary 3

III. Hadron Spectra: From Strong QCD Symmetries to Cosmology 5
- A. Highlights and Prospects in the Exploration of Meson Spectra 5
- B. Highlights and Prospects in the Exploration of Baryon Spectra 7
- C. Synergy Between Experiments with EM and Hadronic Probes in Hadron Spectra Exploration 8
- D. Strong QCD Symmetries from Hadron Spectra 9

IV. Meson and Baryon Structure as a Window into Strong QCD Dynamics 9
- A. Exposing the Emergence of Hadron Mass Through Studies of Pion and Kaon Structure 9
- B. Highlights and Prospects for Nucleon Collinear Parton Distributions 12
  1. Introduction 12
  2. Modern Global QCD Analysis 13
  3. Flavor Separation 13
  4. Spin-Dependent Structure 14
  5. PDFs from Lattice QCD 15
- C. Strong QCD Insights from N^* Structure Studies with EM Probes 15
  1. $\gamma_v pN^*$ Electrocouplings from Exclusive Meson Production and Their Impact on the Exploration of the Ground State Nucleon PDFs 16
  2. From $\gamma_v pN^*$ Electrocouplings to Strong QCD Dynamics 17
- D. Insight into 3D Structure of the Ground State Nucleons in Impact Parameter Space from DVCS and DVMP 18
- E. Insight into 3D Structure of the Ground State Nucleons in Momentum Space from SIDIS 21
- F. Mapping the Energy-Momentum Tensor of Ground State Nucleons from DVCS Data 25
- G. Insights into Strong QCD from Combined Studies of Baryon Ground and Excited States 27
- H. Exploring the Emergence of Nuclear Structure from Strong QCD 29
- I. Nucleon Shape from Continuum QCD 31
  1. Validating Theory Predictions on the Nucleon Shape 32
  2. From Nucleon Structure to the Structure of Atomic Nuclei 32

V. Phenomenology for the Extraction of QCD Interpretable Hadron Parameters 33
- A. Advances in Multi-Channel Amplitude Analyses 33
  1. From Photo to Electroproduction 33
  2. Recent Progress with the Juelich-Bonn and SAID Analysis Frameworks 35
- B. Extension of Amplitude Analyses, Development of Reaction Models for the Extraction of Hadron Parameters from Data 35

VI. Multi-Prong Hadron Structure Theory for Exploration of Strong QCD Emergence 37
- A. Description of Hadron Spectrum and Structure Within LQCD 37
- B. Continuum Strong QCD: Achievements and Prospects 38
- C. Further Developments of Quark Models for the Description of the Hadron Spectrum, Structure, and GPDs 42
- D. Light-Front Holography and Supersymmetric Conformal Algebra: A Novel Approach to Hadron Spectroscopy, Structure, and Dynamics 44

VII. Contributions to the USA EIC Physics Program 48

VIII. Recommendations on Future Joint Activities Between Experiment, Phenomenology, and Theory 50
- A. Hadron Spectroscopy 50
- B. Elucidating N^* Structure in Experiments with Electromagnetic Probes 51
- C. Exposing the Emergence of Hadron Mass 51
- D. The Structure of Atomic Nuclei from Strong QCD 53
- E. The Longitudinal Structure of Nucleons 53
- F. 3D Nucleon Structure and its Emergence from QCD 54

Acknowledgments 55

References 55

I. PREFACE

Following successful meetings in France and South Korea, the third workshop on "*Strong QCD from Hadron Structure Experiments*", was held at Jefferson Laboratory (JLab) during the period of Nov. 6-9, 2019. It gathered a select group of world experts and early career researchers in hadron physics in order to forge an array of synergistic efforts. The workshop consisted of 42 invited talks and a long, concluding discussion session. This document is a summary of the workshop, based on contributions from the conveners of the topical sessions. It aims to provide the scientific background for future joint projects between the experts from these diverse areas in hadron physics.

Studies of the spectrum of hadrons and their structure in experiments with electromagnetic probes offer unique insight into many facets of the strong interaction in the regime of large running coupling of Quantum Chromodynamics (QCD). The experimental program that is part of the new 12-GeV era in the four halls at Jefferson Lab in the U.S., as well as the ongoing and planned experiments at the European facilities ELSA, MAMI, and GSI, and the Asian facilities BES, SPring-8, and JPARC, have considerably extended the scope of research in hadron physics in joint efforts between experiment and phenomenological data analysis.

Studies of the excited nucleon (N^*) spectrum over the last decade have led to the discovery of new "missing" resonances in the global multi-channel analysis of exclusive photoproduction data. Nine new N^* and Δ^* resonances have been reported in the recent PDG edition with three- and four-star status [1]. Experimental studies of the pion and nucleon elastic and transition electromagnetic form factors, including nucleon resonance electroexcitation amplitudes, have allowed us to gain insight into the strong QCD dynamics underlying their mass generation [2–6]. Contemporary knowledge on the ground state nucleon and pion structure has been extended considerably by the results on the proton and pion parton distribution functions (PDFs) [7, 8].

The first results on the ground state nucleon structure in three-dimensions (3D) have started to emerge from semi-inclusive deep inelastic scattering (SIDIS) in 3D momentum space [9]. Analyses of the deeply virtual Compton scattering (DVCS) and deeply virtual meson production (DVMP) exclusive electroproduction data have revealed the light-front structure of the ground state nucleon in the 3D space composed by the 1D space of the longitudinal parton momentum fraction x of the nucleon and by the 2D coordinates for the parton location in the plane transverse to the incoming photon [10]. Recent advances in DVCS studies have delivered a breakthrough result that provides insight into the parton pressure distribution in protons [11].

Extensive efforts on the exploration of the nucleon resonance electroexcitation amplitudes, mostly from CLAS exclusive meson electroproduction data, have provided unique information on many facets of strong QCD, especially connected with the generation of excited nucleon states of different quantum numbers with distinctively different structural features [2, 4].

Impressive progress has been achieved during the past decade in relating hadron structure observables inferred from data to the strong QCD mechanisms underlying hadron generation. These efforts cover a broad research area from the *ab initio* QCD description of hadron structure to continuum QCD approaches capable of exposing emergent phenomena in hadron physics with a traceable connection to the QCD Lagrangian, as well as advances in quark models, including the hypercentral constituent quark model, relativistic approaches, light-front holography, and the chiral quark soliton model. Furthermore, progress in studies of the structure of atomic nuclei within symmetry-based symplectic models [12] opens up the opportunity to improve our understanding of the emergence of the structure of atomic nuclei from strong QCD [13].

The above sketch, which presents selected highlights from diverse areas of the research activity on the exploration of hadron structure with electromagnetic probes, demonstrates the promising potential of such studies to provide insights into the strong QCD dynamics underlying the generation of ground and excited state hadrons and to shed light on the emergence of the hadron properties from the QCD Lagrangian. In order to achieve these challenging objectives, synergistic efforts between experimentalists, phenomenologists, and hadron structure theorists across diverse research directions in hadron physics are especially critical.

II. EXECUTIVE SUMMARY

The impressive progress in charting the spectrum of hadrons and revealing their structure using data from experiments with electromagnetic probes and drawing heavily upon advances in theory has considerably extended our capabilities for gaining insight into the strong QCD dynamics underlying hadron generation. New and continuing efforts using these tools will address the most challenging open problems in the Standard Model, *e.g.* the emergence of hadron mass, the nature of quark-gluon confinement, and the role of dynamical chiral symmetry breaking (DCSB) in the generation of hadron mass and structure. It is anticipated that, with time, new and continuing studies will deliver explanations of the many facets of strong QCD dynamics that are expressed in hadron spectra and structure, beginning with only the QCD Lagrangian. This document provides an overview of the rapidly developing research paths that were highlighted by the workshop conveners as particularly promising avenues toward reaching these challenging goals.

Studies of the excited nucleon (N^*) spectrum over the last decade have delivered numerous breakthroughs. Several long-awaited missing resonances have been dis-

covered in the global multi-channel analysis of exclusive photoproduction data with a decisive impact from the CLAS results on exclusive $K\Lambda$ and $K\Sigma$ photoproduction [14]. Nine new N^* and Δ^* resonances have been reported in the recent Particle Data Group (PDG) edition with three- and four-star status [1]. In addition, a new $N'(1720)3/2^+$ resonance has been observed in combined studies of the CLAS $\pi^+\pi^- p$ photo- and electroproduction data [15]. The first results on the electrocoupling of missing resonances have become available, allow for insight on the particular structural features of missing baryon states that make them so difficult to detect in experiments.

Investigations of meson and baryon spectra have highlighted the symmetries of the strong interaction that underlie the generation of hadrons. Completion of the excited nucleon and light meson spectrum using data from experiments with real and virtual photons will provide the ultimate experimental benchmarks for the theoretical description of the hadron spectrum starting from the QCD Lagrangian. Such studies are of particular importance for understanding early Universe evolution in the transition between a deconfined mixture of gluons and quarks to a gas of hadrons. Highlights and prospects for mapping hadron spectra are presented in Sections III A and III B.

Experiments capitalizing on 12 GeV at JLab and studies foreseen with the U.S. Electron-Ion Collider (EIC) promise to considerably expand opportunities for the exploration of meson structure. The first results on the pion and kaon elastic electromagnetic form factors and their PDFs are expected in the still almost unexplored range of high photon virtualities $Q^2 > 5.0$ GeV^2. Results on pseudoscalar meson structure offer unique insights into the dual nature of these particles as a bound $q\bar{q}$ system and as the Goldstone boson whose emergence is driven by dynamical chiral symmetry breaking in the process of dressed quark mass generation. Furthermore, credible information on the pion Bethe-Salpeter amplitude constrained by experimental results on the pion elastic form factor and PDF offer clean insight into the dynamics of emergent hadronic mass. Comparative studies of pion and kaon structure will provide insight on the difference in the dressed quark mass generation for u, d, and s quark flavors, which will a starting point for the exploration of the flavor dependence of hadron mass generation. The current status, prospects, and the impact on understanding of strong QCD from meson structure studies are presented in Section IV A.

Consistent results on the strong QCD dynamics underlying hadron generation from independent studies of both meson and baryon structure are of particular importance. Contemporary knowledge of the structure of the ground state nucleon has been considerably extended by the results on their electromagnetic elastic form factors [16] and PDFs [7]. Analyses of the resonance electroexcitation amplitudes from CLAS data [5, 6] will extend our knowledge about the ground state nucleon PDF at large x_B values in the resonance region. Experimental studies of the d/u ratio in nucleon PDFs at x_B values close to unity, which are in progress in Hall A/C at JLab, offer a sensitive test for the QCD-rooted predictions of ground state nucleon structure. Data on inclusive and semi-inclusive electron scattering provide essential contributions to the store of detailed information on the flavor-separated quark/parton and gluon distributions in nucleons. Progress in lattice QCD and the development of novel quasi- and pseudo-PDF concepts pave the way for the description of nucleon PDFs starting from the QCD Lagrangian [17–19]. The results and prospects for the exploration of the structure of the ground state nucleon in 1-dimension (1D) are presented in Section IV B.

The extensive efforts dedicated to the extraction of the nucleon resonance electroexcitation amplitudes, mostly from CLAS exclusive meson electroproduction data, have provided unique information on many facets of strong QCD as they appear in the generation of excited nucleon states of different quantum numbers with distinctively different structural features [2, 4]. During the last decade, the electroexcitation amplitudes for most excited nucleon states in the mass range up to 1.8 GeV have become available at photon virtualities $Q^2 \leq 5.0$ GeV^2 [5, 6]. Analyses of these results within continuum QCD approaches and quark models have revealed the structure of nucleon resonances to emerge from a complex interplay between an inner core of three dressed quarks and an external meson-baryon cloud. A successful description of the electroexcitation amplitudes of the low-lying N^* states achieved with continuum QCD approaches, which employ the same momentum dependence of the dressed quark mass inferred from the QCD Lagrangian [16, 20, 21], have demonstrated the capability of gaining insight into the dynamics of hadron mass generation from the combined studies of pion and nucleon electromagnetic form factors, including $N \to N^*$ electroexcitation amplitudes.

Verified predictions for meson electromagnetic form factors and Parton Distribution Functions (PDFs) with a dressed quark mass function constrained by data on the structure of ground and excited state nucleons will validate insight into this key ingredient of strong QCD in a nearly model-independent way. With the well-established dressed quark mass function and diquark correlation amplitudes from the studies of nucleon ground and excited states, the emergence of the shape of the nucleon in its intrinsic frame can be predicted within continuum QCD approaches, paving the way towards understanding the emergence of nuclear structure from strong QCD. The status and prospects for exploration of the structure of excited state nucleons are presented in Section IV C. Their impact on studies of the emergence of the structure of atomic nuclei from strong QCD is discussed in Section IV H.

The first results on the ground state nucleon structure in 3D have started to emerge. Data from semi-inclusive meson and di-hadron electroproduction experiments not

only offer insight into the parton momentum distribution in the plane transverse to the virtual photon momentum, but have also provided detailed information on the correlations between the parton and nucleon spins, and between the partons' spin and their orbital momenta. Global analyses of these results have already produced 3D images of the parton distribution in the momentum space of the ground state nucleons [9].

Analyses of DVCS and DVMP exclusive electroproduction data have revealed additional information about the light-front structure of the ground state nucleon in the 3D space composed by the 1D space of the longitudinal parton momentum fraction x of the nucleon and the 2D coordinates for the parton location in the plane transverse to the incoming photon [10]. These two complementary perceptions of the ground state nucleon – 3D in momentum and coordinate space – offer new opportunities for insights into the dynamics driving the formation of the ground state nucleon. Such studies will drive future exploration of hadron structure at JLab in the 12 GeV era and at the future Electron-Ion Collider through partnerships between BNL and JLab.

Recent advances in DVCS studies have also delivered a breakthrough that reveals features of the parton pressure distribution in protons [11]. This information allows us to map out the components of the nucleon energy-momentum tensor underlying the balance of the explosive and implosive pressures within the nucleon. It opens a path toward understanding the strong QCD dynamics behind pressure generation, and may provide insight into the emergence of confinement.

Achievements and future potential of 3D imaging and derived insights into the energy-momentum tensor of the ground state nucleon via synergistic efforts using SIDIS, DVCS, and DVMP studies are discussed in Sections IV E and IV F.

Available and anticipated results on the spectrum and structure of ground and excited hadron states, and the novel potential of hadron femto-imaging in 3D space, offer qualitatively new opportunities for exploration of the strong QCD dynamics underlying the emergence of hadronic mass and gluon and quark confinement, and for developing insights into the facets of strong QCD that are responsible for generating the entire diverse array of hadrons with apparently distinct structural features. Strong theory support is essential in order to ensure full capitalization on the wealth of new data. Expanded efforts are needed in the development of reaction models and amplitude analysis approaches that are capable of extracting needed information from data, *i.e.* hadron elastic and transition electromagnetic form factors, and the 1D and 3D parton distributions. This activity is discussed in Sections IV E, V A 1, and V B. The development of a multi-prong theoretical framework for the description of the hadron spectrum and structure and its emergence from QCD are presented in Sections IV G and VI.

Initial ideas for joint research activities between experimentalists, phenomenologists, and theorists that are aimed at drawing insights into strong QCD from studies of hadronic spectra and structure are outlined in the closing Section VIII. After further discussion within the hadron physics community, these ideas will be updated and developed at the next workshop in this strong QCD series, which will be hosted by the Institute for Nonperturbative Physics at Nanjing University in 2021. A bright future marked by rewarding collaboration on concrete new projects is anticipated.

III. HADRON SPECTRA: FROM STRONG QCD SYMMETRIES TO COSMOLOGY

A. Highlights and Prospects in the Exploration of Meson Spectra

The turn of the century has seen a renaissance in meson spectroscopy. Unexpected results from older experiments (BELLE, BABAR, CLEO); new experiments specifically designed to hunt for exotica (COMPASS, GlueX); and analysis of new large datasets (LHCb, BESIII) have coincided to generate great excitement and opportunity in the exploration of the meson spectra.

The textbook description of hadrons postulates colorless three valence quark states as baryons with a quark-antiquark pair forming mesons. Quark models with these building blocks have historically done a remarkable job in reproducing the observed states. Typically such models take heavy spin 1/2 constituent quarks, $m_{u,d} \simeq 1/3 M_{proton}$, with an attractive potential mediated by single gluon exchange and a confining potential proportional to the distance between the quarks. Different couplings of the relative orbital angular momentum to the quark spins combined with the three light quark flavors (u, d, s) produces groups of meson nonets with specific J^{PC} quantum numbers. Such constituent quark models provide an important benchmark with which to compare both experimental observations and sophisticated QCD-based calculations such as Lattice QCD or Light Front Holography as outlined in Section VI.

QCD however does not restrict states bound by the strong interaction to consist of only these configurations. Although it is remarkable that after fifty or so years of study we are still seeking to establish which types of hadrons may exist there are now significant experimental candidates that clearly do not fit the quark model picture alone. Such states are termed "exotic" and their structure is likely to come from the following color neutral possibilities: meson-meson molecules, tetraquarks, glueballs, and hybrids. In molecules two color-singlet mesons are bound by virtual meson exchanges, similar to nucleons in a nucleus; while in tetraquarks a diquark and antidiquark are tightly bound by the exchange of gluons similar to a quark and antiquark in a meson. Due to gluons being self-interacting it seems possible that they can form bound states with no valence quarks, giving rise to

so called glueballs; while states consisting of mixed quark and gluon constituents are termed hybrids.

The trigger for the increased focus on meson spectroscopy was the unexpected discovery of the $X(3872)$, now known as $\chi_{c1}(3872)$ due to its $J^{PC} = 1^{++}$, by Belle in 2003 [22]. A number of experiments at this time were searching for missing quark model states above the open charm $D\bar{D}$ threshold and the Belle discovery was soon verified by others. Since then many more similar states have been found containing hidden charm $c\bar{c}$ and are commonly referred to as X, Y, and Z mesons depending on their quantum numbers. However, none of these seem to match the expectations for the missing quark model states and so they are all regarded as candidates for exotic mesons. In particular the charmonium-like charged $Z_c(4430)$ state would require tetraquark or molecular compositions. While dynamic explanations, such as triangle singularities, for the observed structures seen in experiments also exist, it seems neither these nor specific exotic configurations can single handily explain the wealth of states now observed [23]. For a detailed review of the subject see Ref. [24].

In the light quark sector the lightest scalar meson nonet containing the $f_0(980)$ and $a_0(980)$ has been regarded as somewhat of a puzzle. Its masses are too low compared to quark model expectations and the mass ordering of the states does not follow the usual isoscalar-isovector pattern. It is possible to explain these features via a molecular or tetraquark composition [25]. Establishing a further nonet with non-exotic quantum numbers but without quark model predictions, by for example being too close in mass to a nonet with the same J^{PC}, would add further weight to this picture. For example the axial-vector states $f_1(1420)$ and $a_1(1420)$ [26] could be part of such a nonet as there are no free suitable quark model assignments.

Hybrid mesons can have exotic quantum numbers, that is quantum numbers that cannot be reached by straightforward quark models. Lattice QCD predicts 5 nonets consisting of exotic quantum numbers [27] and suggests a constituent gluon with mass around $1 - 1.5$ GeV and $J^{PC} = 1^{+-}$. Discovery of a nonet with quantum numbers $0^{+-}, 1^{-+}$, or 2^{+-} would provide conclusive evidence for the requirement of gluons as an underlying degree of freedom in the formation of the hadronic spectrum. To this end, the COMPASS experiment using a 190 GeV π^- beam has provided strong experimental evidence for the existence of the exotic isovector 1^{-+}. Early measurements with lower statistics already found indications of such a state in several final states: 3π, $\eta'\pi$, $b_1\pi$, $f_1\pi$, for a full review see Ref. [28]. The new 3π data with 4.6M events allowed for analysis of unprecedented detail [29]. In addition, the combination of the new $\eta\pi^-$ and $\eta'\pi^-$ final states allowed a sophisticated coupled channel analysis by JPAC to resolve two possible states, the $\pi_1(1400)$ and $\pi_1(1600)$, as coming from a single pole consistent with the $\pi_1(1600)$, and is presented in Section V B. The mass of this single state is in good agreement with the Lattice calculation expectations for an exotic hybrid.

A promising avenue for extending the search of exotic hybrids beyond the 1^{-+} isovector is to use photon beams and such is the plan at the upgraded Jefferson Lab with the flagship hybrid meson experiment GlueX and the MesonEx experiment with the CLAS12 detector. The spin-1 photon acts as an effective beam of ρ, ω, and ϕ mesons with isovector and isocalar components allowing production of states from all of the lightest five hybrid nonets. Charge exchange production mechanisms allow separation of isospin. In addition linear polarization of the photon acts as a filter for the naturality of the exchange particle giving more control over the production mechanism through, for example, separating t-channel pion and ρ exchanges.

For the already seen $\pi_1(1600)$ its decay modes to $\rho\pi$ and $\eta'\pi$ should be readily accessible and other decay modes such as $b_1\pi$ and $f_1\pi$ should be possible with large statistic datasets. Importantly, the isoscalar η_1 can also be measured with decays to $f_2\eta$ and $a_2\pi$, while the η_1' can decay to K^*K. For the 2^{+-} sector decays of the b_2 to $\omega\pi$ and $\rho\eta$, and the h_2 to $\rho\pi$, could provide the first evidence for this nonet.

A possibility for investigating glueballs is to use the photoproduction of two identical pseudoscalar mesons, *i.e.* $\pi^0\pi^0$, $\eta\eta$, or K_0K_0, which filters out $f_{0,2,4}$ states to allow measurement of photocouplings and branching ratios of the scalar mesons [30].

The GlueX experiment started taking data in 2014. It features a linearly polarized tagged photon beam through coherent bremsstrahlung on a diamond radiator and a large acceptance detector providing coverage from 1 to 120°. This allows it to measure many different final states in parallel and reconstruct mesons decaying to many particles. The linearly polarized portion of the beam covers photon energies from around 8 to 9 GeV, beyond where contributions from s-channel baryon resonances can provide significant background.

The first results consist of photon beam asymmetry measurements of pseudoscalar mesons, using the linear polarization to determine the naturality of the exchange mechanism [31, 32]. This provides a useful test of the reaction models that will be used to investigate the production of other mesons. In addition the photoproduction of the J/ψ close to threshold provided a means to hunt for s-channel resonances with hidden charm such as the LHCb pentaquark [33].

CLAS12 started production data taking in 2018 and first analyses are in progress [34]. In this experiment the production rate of mesons is increased through detecting electrons with small scattering angles in a forward calorimeter, thus tagging quasi-real photons with similar polarization and energy to the GlueX experiment [35]. In this way similar final states to GlueX will be investigated giving complementary results.

B. Highlights and Prospects in the Exploration of Baryon Spectra

Over the past six years eight light-flavored baryon states in the mass range from 1.85 to 2.15 GeV have been discovered or evidence for the existence of states has been strengthened significantly, as visualized in the increase of the star ratings assigned by the Particle Data Group (PDG) in their bi-annual Review of Particle Properties (RPP). To a large degree this has been the result of adding very precise photoproduction data in open strangeness channels to the database that are included in multi-channel partial-wave analyses. The possibility to measure polarization dependent observables with high statistics in these processes has been critical. These discoveries shown in Fig. 1 and cataloged in the 2018 edition of the Review of Particle Properties [1], while essential in completing the light-quark baryon spectrum, have so far not brought any surprises, as all the new states have quantum numbers that fit well in the spectrum predicted by SU(6)×O(3) symmetry as well as in Lattice QCD with a pion mass of 400 MeV. Because of the large pion mass in LQCD and of constituent quark masses in the quark model, an agreement of mass predictions in LQCD with the physical resonance masses is not expected.

State N((mass)J^P	PDG 2010	PDG 2018
N(1710)1/2$^+$	***	****
N(1880)1/2$^+$		***
N(2100)1/2$^+$	*	***
N(1895)1/2$^-$		****
N(1900)3/2$^+$	**	****
N(1875)3/2$^-$		***
N(2120)3/2$^-$		***
N(2060)5/2$^-$		***
Δ(1600)3/2$^+$	***	****
Δ(1900)1/2$^-$	**	***
Δ(2200)7/2$^-$	*	***

FIG. 1. Evidence for 11 N^* and Δ states in RPP 2010 compared with RPP 2018.

As shown in Fig. 2, the resonant states appear to form mass-degenerate, spin-parity multiplets [36]. At 1900 MeV four of the newly established resonances in the N^* sector (with green frames) form a nearly mass degenerate quartet. Also in the Δ sector six states are mass degenerate near 1950 MeV; five of them were known before, but a new state falls into the same mass window. Neither quark models nor current LQCD simulations with 400 MeV pion masses predict such a behavior. Note that the same degeneracy is observed in the high-energy spectrum of light mesons and that some possible explanation has been proposed in Ref. [37], where the degeneracy is due to the screening of the linearly rising confinement potential due to the spontaneous creation of quark-antiquark pairs. It is possible that a similar mechanism could play a role in the baryon sector.

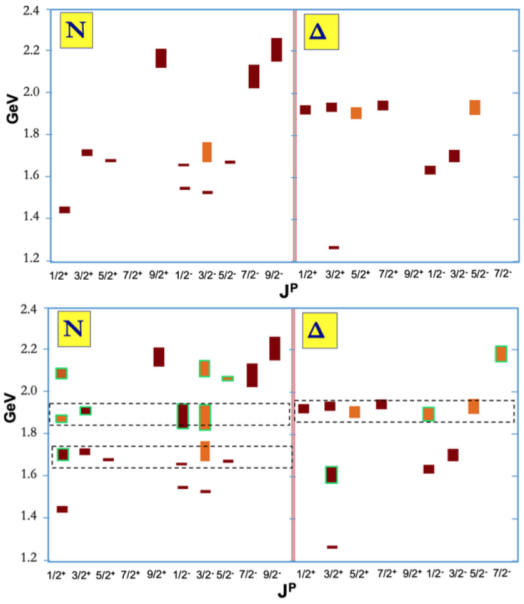

FIG. 2. Top panel: Nucleon and Δ resonance spectrum below 2.2 GeV in the RPP 2010 [38]. Bottom panel: Nucleon and Δ resonance spectrum below 2.2 GeV in RPP 2018 [1]. The green frames highlight the new states and states with improved star ratings compared to 2010. The light brown color indicate 3* states, the dark color indicates 4* states. The dashed frames indicate apparent mass degeneracy of states with masses near 1.7 GeV and 1.9 GeV and different spin and parity. The Bonn-Gatchina analysis includes all of the $K^+\Lambda$ and $K^+\Sigma^0$ photoproduction cross section and polarization data, as well as the pion photoproduction data.

The more realistic tests of strong QCD will come when Lattice predictions of the light-quark baryon spectrum with physical pion masses are undertaken, *i.e.* when resonances are allowed to decay. Forays in this arena have recently been undertaken in the meson sector [2]. Another critical aspect in testing strong QCD in baryon resonance production is the excitation of hybrid baryons, *i.e.* excited states with a dominant component of glue in the wave function. In contrast to the meson sector, gluonic baryons come with the same quantum numbers as ordinary quark model baryons, *i.e.* they are not exotic in the sense that such states are not possible in the standard SU(6)×O(3) quark model symmetry. We therefore will have to resort to other means to uniquely distinguish hybrid baryons from ordinary baryons with the same quantum numbers. Searching for more states than predicted within the quark model is one possibility, however not fully satisfying because of the remaining ambiguities.

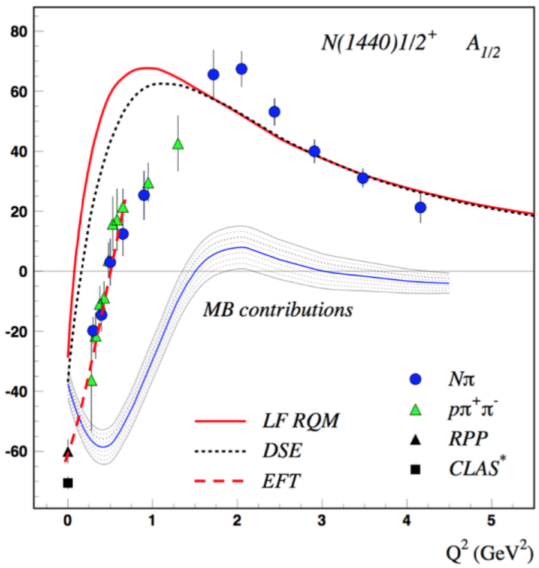

FIG. 3. The transverse helicity amplitudes $A_{1/2}$ for the Roper resonance $N(1440)1/2^+$. Data are from CLAS compared to the LF-RQM with running quark masses (solid line), and with projections from the Dyson-Schwinger Equation (DSE/QCD) approach (dotted line). The shaded band indicates non-3-quark contributions inferred from the difference of the LF-RQM curve and the CLAS data. The red dashed line is the Effective Field Theory (EFT) calculation that describes the data at small Q^2.

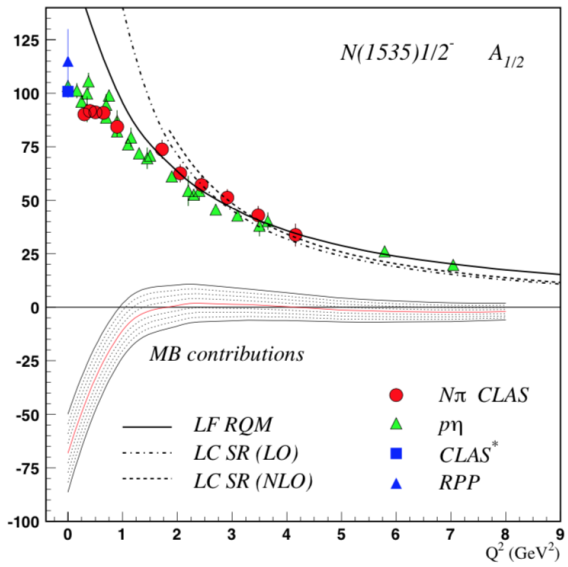

FIG. 4. The transverse amplitude $A_{1/2}$ for the $N(1535)1/2^-$ resonance compared to LF-RQM calculations (solid line) and QCD computations within the Light Cone Sum Rule approach.

Meson electroproduction is a possible tool that can provide separation of states with a different number of partonic degrees of freedom, 3 in the case of quark excitations and 4 (3 quarks + 1 gluon) for gluonic excitations. The latter is expected to show a faster drop of the transition form factor with Q^2, than the drop expected for regular 3-quark model states. For a realistic separation it is essential to develop models for the transition form factor dependence of hybrid states. There is currently only one calculation available, and that is for the Roper resonance [39], which was originally considered a candidate for the lowest mass hybrid baryon in the nucleon sector [4]. This possibility has been eliminated based on the electroproduction data from CLAS. The transition amplitudes are in excellent agreement with the LF-RQM and with the DSE/QCD calculations that find that the Roper at its quark core is the first radial excitation of the nucleon [2]. Figure 3 shows the comparison of the CLAS data with the two calculations [20, 40], demonstrating good agreement of the data at $Q^2 > 2$ GeV^2 with the LF-RQM and DSE/QCD calculations.

Another example is the $N(1535)1/2^-$ state, where there is experimental information in the largest range of Q^2. In Fig. 4 the data are compared with the light front relativistic quark model (LF-RQM) and the Light-Cone sum rule (SR) results in leading-order (LO) and in next-to-leading-order (NLO) [41, 42]. There is obviously excellent agreement of the data with the LF-RQM at $Q^2 > 1.5$ GeV^2, and with the QCD-based results from Light-Cone LO and Light-Cone NLO at $Q^2 > 2$ GeV^2. The ongoing experiments with CLAS12 at the highest available energy of ∼11 GeV should allow for the extension of the range in Q^2 to beyond 10 GeV^2 for both of these prominent excited states of the nucleon [43].

C. Synergy Between Experiments with EM and Hadronic Probes in Hadron Spectra Exploration

Understanding the full nucleon spectrum, including gluonic excitations, within strong QCD will constitute a breakthrough of similar importance as happened with the full understanding of the excitation spectrum of hydrogen and other atoms as a consequence of the discovery of Quantum Electrodynamics (QED). Agreement between strong QCD projections and the experimental data of resonance masses (amplitude pole positions in the complex energy plane), width (imaginary part of the resonant amplitude), should be commensurate with the uncertainties of the experimental data. In order to achieve such quantitative agreement between strong QCD and experiment, much more experimental data, both in hadron scattering experiments and in photo-/electroproduction must be produced and analyzed in multi-channel analyses. This is especially the case for multiple mesons in the final state as in $\gamma p \to p\pi^-\pi^+$. The $N\pi\pi$ final state is the dominant final state coupling to the nucleon and N^* resonances at masses from 1.65 to 1.9 GeV. There are very limited data in the hadron sector for this channel.

D. Strong QCD Symmetries from Hadron Spectra

A full understanding of the excited baryon spectrum is very relevant in order to describe the transition of the microsecond old universe from the quark-gluon plasma phase (perfect liquid) to the hadron phase of fully formed nucleons. It is now well understood that this transition is not a simple first-order phase transition that occurs instantaneously when the boundary between two phases in the QCD phase diagram is crossed.

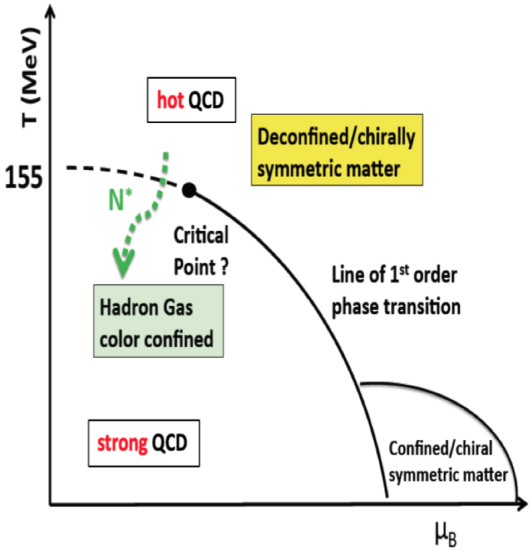

FIG. 5. A generic phase diagram for the transition from the de-confined quark-gluon state to the confined hadron state.

This is shown in Fig. 5 where the temperature is plotted versus the baryon chemical potential. An analogy might be water vapor transitioning to liquid water when the temperature versus pressure boundary is crossed. In our case a cross-over between the two phases occurs that is governed and moderated by the excitation of baryons of all flavors. Figure 6 shows the ratio of the baryon chemical potential for strange baryons and all baryons using all baryons present in the editions of the PDG 2012 and 2016 for all baryons with ratings 3* (existence likely) and 4* (existence certain) [44]. The lines are hadron resonance gas (HRG) models compared to the latest hot Lattice QCD (LQCD) calculations. The HRG models undershoot the LQCD results, indicating that many baryon resonances are still missing, and need to be searched for, both in the strangeness sector and in the non-flavored sector. There are a lot more data already published or are currently under analysis that have not been included in multi-channel analyses, especially in vector meson photoproduction, including a significant amount of polarization data of all kinds.

An even more dramatic shortage of excited baryons exists in the charm sector, where the discrepancy in the HRG models in comparison with the LQCD band is much more dramatic compared to the strange- and the non-

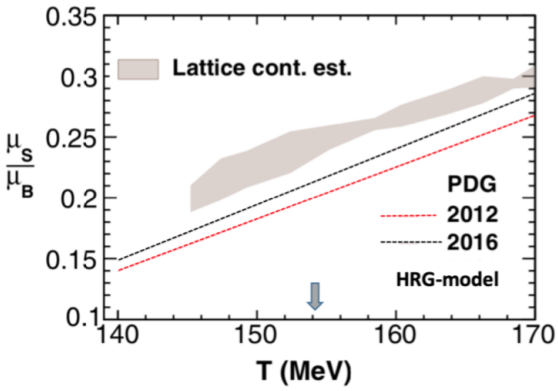

FIG. 6. The ratio of baryon chemical potential of the strangeness versus all baryons for the RPP 2014 and RPP 2016. The hashed gray area shows the LQCD calculation in "hot QCD". The straight lines are calculations within a hadron gas model. The 2016 line, which includes more N/Δ baryon states, moves closer to the LQCD area. Note that only 3* and 4* states are included. If the newly discovered states in RPP 2018 (seven states that are now at 3* or 4* status) were included, this line would move even closer to the LQCD area.

flavored baryon sector, *i.e.* excited hyperons and excited nucleons [45]. This should be an excellent motivation for a charm baryon spectroscopy program at the Electron-Ion Collider.

IV. MESON AND BARYON STRUCTURE AS A WINDOW INTO STRONG QCD DYNAMICS

A. Exposing the Emergence of Hadron Mass Through Studies of Pion and Kaon Structure

Continuum Schwinger function methods (CSMs) provide a systematic, symmetry preserving approach to solving problems in QCD [2, 3, 46–49]. Notably, where fair comparisons can be drawn, predictions from continuum analyses are practically identical to those obtained via numerical simulations of LQCD; and while lattice calculations maintain a tighter connection with the QCD Lagrangian, the range of observables accessible to CSMs is greater. Evidently, the approaches are complementary and there is real synergistic potential.

The merits of combining the strengths of the continuum and lattice QCD approaches are highlighted in Fig. 7, which depicts the process-independent effective charge of QCD [50–53]. It was obtained by combining the best available results from continuum and lattice analyses of the gauge sector. Owing to the dynamical breaking of scale invariance, evident in the emergence of a gluon mass scale [54], $m_0 = 0.43(1)$ GeV, this coupling saturates at infrared momenta: $\hat{\alpha}(0)/\pi = 0.97(4)$. Among other things: $\hat{\alpha}(k^2)$ is almost identical to the process-dependent (PD) effective charge defined via the

Bjorken sum rule [55–57]; and also that PD charge which, employed in integrating the one-loop DGLAP evolution equations [58–61], delivers agreement between pion parton distribution functions computed at the hadronic scale and experiment [53, 62–64]. The diversity of unifying roles played by $\hat{\alpha}(k^2)$ suggests that it is a strong candidate for that object that represents the interaction strength in QCD at any given momentum scale [65]; and its properties support a conclusion that QCD is a mathematically well-defined quantum field theory in four dimensions.

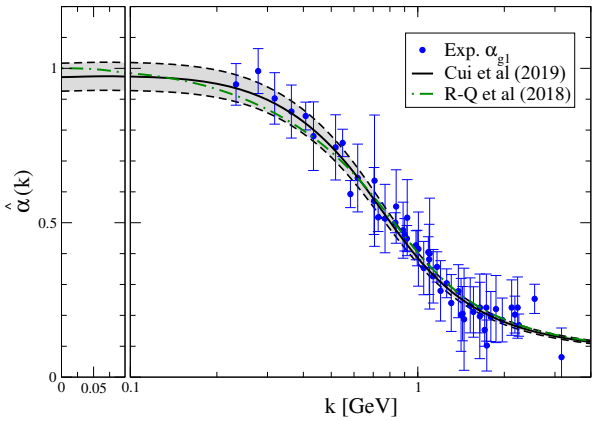

FIG. 7. Solid black curve within gray band – RGI PI running-coupling $\hat{\alpha}(k^2)/\pi$, obtained using lattice configurations for QCD generated with three domain-wall fermions at a physical pion mass [53]; and dot-dashed green curve – earlier result [52]. Also depicted, world data on the process-dependent effective coupling α_{g_1}, defined via the Bjorken sum rule, the sources of which are listed elsewhere [53]. For additional details, see Refs. [51, 55–57]. The k-axis scale is linear to the left of the vertical dashed line and logarithmic otherwise.

The journey to this effective charge began in the late 1960s with the discovery of quarks. Much has since been learned about the role of QCD's elementary excitations in building observable matter by studying hadron elastic and transition electromagnetic form factors and also via DIS. The former provide empirical access, *e.g.* to the distributions of charge and magnetization within hadrons; and the latter to momentum probability distributions. Crucially, some of the earliest and most rigorous predictions of QCD relate to these observables; and new era detectors and facilities are expected to finally bring their validation within reach.

Perhaps the best known QCD predictions are those made for the electromagnetic form factors of pseudoscalar mesons, *e.g.* the pion and kaon. Within the nuclear physics context, these states are abnormally light: they are pseudo-Nambu-Goldstone modes [66, 67]. Yet, modern theory predicts that their properties provide the cleanest window onto emergent hadronic mass (EHM) within the Standard Model [68]. This connection is expressed in many ways; but, most forcefully, in the behavior of meson form factors at large momentum transfers. On this domain, QCD relates measurements simultaneously to low- and high-energy features of QCD, *viz.* to subtle features of meson wave functions and to the character of quark-quark scattering at high-energy [69–71]. These relationships are expressed concretely in modern continuum analyses, with predictions that expose the crucial role of EHM [72–74]. Hence, experiments focused in this area are of the greatest importance.

Exploiting such strengths as high-luminosity and high-energy, new era facilities have the potential to deliver precision results on pion and kaon electromagnetic form factors at large-Q^2 using the Sullivan process [75]. Contemporary phenomenology and theory indicate that, with achievable kinematics, the proton's "meson cloud" can provide reliable access to a meson target [3, 76]. An array of such experiments is already approved at JLab [77, 78]; and could also be performed with an electron-ion collider (EIC) in the USA and, potentially, in China (EicC).

To proceed experimentally, one needs to ensure that the Sullivan process is a valid tool for meson structure experiments. To check whether these conditions are satisfied empirically, one can take data covering a range in t, particularly low $|t|$, and compare with phenomenological and theoretical expectations. Furthermore, for the extraction of precision elastic form factors, one must ensure that the virtual photon is longitudinally polarized. In the W, Q^2 regime accessible at JLab, the key to such form factor extractions is longitudinal-transverse (L/T) separated cross sections and control over systematic uncertainties. The latter include checking the consistency of the model used to extract the form factor from electroproduction data. This can be done by extracting the form factor at two values of t_{min} for fixed Q^2 and verifying that the pole diagram is the dominant contribution to the reaction mechanism. Extensive studies [3, 79] over the last decades have generated confidence in the reliability of this method and precision form factor data have been extracted to Q^2=2.5 GeV^2 [80, 81] (see Fig. 8 – upper panel).

The approved experiments at JLab [82, 83] will provide a comprehensive set of L/T separated pion and kaon electroproduction data up to Q^2 values of 8.5 GeV^2 (pion) and 5.5 GeV^2 (kaon), also enabling measurements of the pion and kaon form factors. Beyond JLab, at the high Q^2, W accessible with the EIC [7, 8] and possibly at EicC [84], phenomenological models predict $\sigma_L \gg \sigma_T$ at small $-t$. There, a practical method of isolating the longitudinal virtual photon is to use a model to distinguish the dominant differential cross section, $d\sigma_L/dt$, from the measured, unseparated differential cross section, $d\sigma/dt$. Focusing on the pion because the kaon is similar, one can then experimentally validate the model, *i.e* the condition $\sigma_L \gg \sigma_T$, by using the π^-/π^+ ratio of charged pion data extracted from electron-deuteron beam collisions in the same kinematics as charged pion data from electron-proton collisions.

The connection between pion and kaon form factors and mass generation in the Standard Model is illustrated in Fig. 8 [74]. The lower panel depicts two similar but

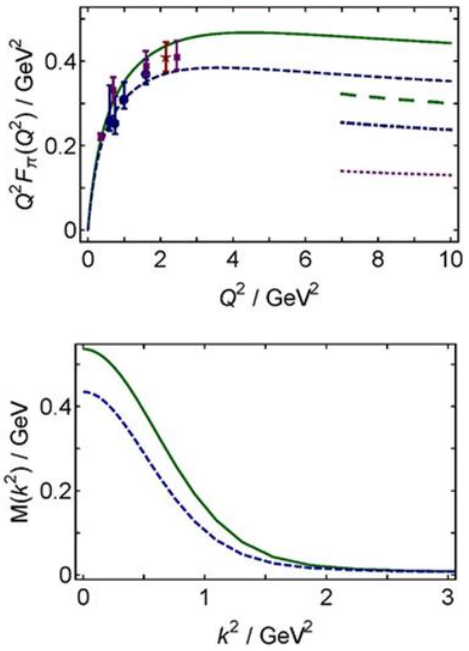

FIG. 8. Top: $F_\pi(Q^2)$ obtained with the mass function in the lower panel: $r_\pi = 0.66$ fm with the solid green curve and $r_\pi = 0.73$ fm with the dashed blue curve. The long-dashed green and dot-dashed blue curves are predictions from the QCD hard-scattering formula, obtained with the related, computed pion parton distribution amplitudes (PDAs). The dotted purple curve is the result obtained from that formula if the asymptotic profile is used for the PDA: $\varphi(x) = 6x(1-x)$. Bottom: Two dressed-quark mass functions distinguished by the amount of dynamical chiral symmetry breaking: emergent mass generation is 20% stronger in the system characterized by the solid green curve, which describes the more realistic case.

distinct dressed light-quark mass-functions, $M(k^2)$, characterized by a different strength for EHM. The solid green curve was computed using a QCD effective charge whose infrared value is consistent with modern continuum and lattice analyses of QCD's gauge sector [53], whereas the dashed blue curve was obtained after reducing this value by 10%. In a fully consistent calculation, such a modification is transmitted to every element in the calculation; and subsequently to all observables. The resulting impact on $F_\pi(Q^2)$ is depicted on the top: evidently, this experiment is a keen probe of the strength of EHM. Figure 8(top) also depicts results obtained using the QCD hard scattering formula derived for pseudoscalar mesons [69–71]: at empirically accessible energy scales they, too, are sensitive to the emergent mass scale in QCD [72–74].

At a similar level of rigor is the QCD prediction for the behavior of the meson structure functions; namely, the experimental observables that probe the quark momentum distributions. More than forty years ago [85–87], it was shown that the momentum distributions of valence-quarks within the pion have the following behavior at large-x (x is the quark's fraction of the pion's light-front momentum): $u^\pi(x;\zeta=\zeta_H) \sim (1-x)^2$, where ζ_H is an energy scale characteristic of non-perturbative dynamics. Ongoing analyses are providing increasing support for the identification $\zeta_H = m_0$, *i.e.* the renormalization-group-invariant gluon-mass. m_0 is an essentially non-perturbative scale whose existence ensures that parton modes with $k^2 \lesssim m_0^2$ are screened from interactions. Hence, it appears as a natural boundary between soft and hard physics. The most recent measurements of $u^\pi(x;\zeta)$ are thirty years old [88–93]; and conclusions drawn from those experiments have proved controversial [94]. For example, using a leading-order (LO) perturbative QCD (pQCD) analysis, Ref. [93] (the E615 experiment) reported ($\zeta_5 = 5.2$ GeV): $u^\pi_{\rm E615}(x;\zeta_5) \sim (1-x)^1$, a striking contradiction of the QCD prediction. Subsequent CSM calculations [95] confirmed the QCD prediction and eventually prompted reconsideration of the E615 analysis, with the result that, in a complete next-to-leading-order (NLO) study [96, 97], the E615 data can be viewed as consistent with QCD. Notwithstanding these advances, uncertainty over $u^\pi(x)$ remains because more recent analyses of the E615 data have failed to consistently treat NLO effects and, crucially, modern data are lacking.

Pressure is also being applied by modern advances in theory. Novel LQCD algorithms [17, 18, 98–100] are beginning to yield results for the point-wise behavior of $u^\pi(x)$ [101–106]; and recent continuum analyses are also yielding new insights. As displayed in Fig. 9, the first parameter-free predictions of the valence, glue and sea distributions within the pion [62, 63] reveal that, like the pion's parton distribution amplitude, $u^\pi(x)$ is hardened as a direct consequence of emergent mass. Very significantly, the new continuum prediction for $u^\pi(x;\zeta_5)$ matches that obtained using lattice-QCD [104]. Consequently, the Standard Model prediction: $u^\pi(x;\zeta=\zeta_H) \sim (1-x)^2$, is stronger than ever before; and an era is approaching in which new experiments with novel design specifications will enable the ultimate validation of this fundamental prediction.

To access the structure functions via experiment through the Sullivan process, one can work with the differential cross section, which is transverse in the Bjorken limit, and trust both (*i*) the phenomenology and theory, which predict that meson structure can reliably be extracted on a sizeable low-$|t|$ domain and (*ii*) comparisons with results from other experimental techniques on their common domain. The first data is expected from the tagged DIS program at JLab, including pion [107] and kaon [108] structure functions. At the EIC, a large range in x_π and Q^2, roughly covering down to $x_\pi = 10^{-3}$ at $Q^2 = 1$ GeV^2 and up to $x_\pi = 1$ at $Q^2 = 1000$ GeV^2, is accessible [8]. Experiments that will deliver new pion and kaon Drell-Yan data are also proposed for the CERN M2 beam line by the AMBER collaboration [109]. Such data would constrain the separated valence and sea quark pion PDFs above $x_\pi = 0.2$. The previously published HERA results on the pion Sullivan process would continue to

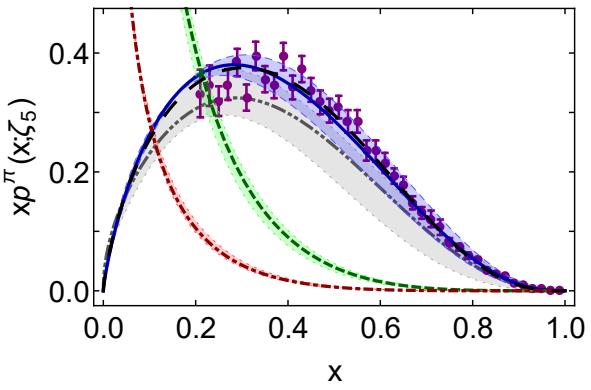

FIG. 9. Pion valence-quark momentum distribution function, $xu^\pi(x;\zeta_5)$: dot-dot-dashed (gray) curve within shaded band – LQCD result [104]; long-dashed (black) curve – early continuum analyses [95]; and solid (blue) curve embedded in shaded band – modern, continuum calculation [62, 63]. Gluon momentum distribution in pion, $xg^\pi(x;\zeta_5)$ – dashed (green) curve within shaded band; and sea-quark momentum distribution, $xS^\pi(x;\zeta_5)$ – dot-dashed (red) curve within shaded band. (In all cases, the shaded bands indicate the size of calculation-specific uncertainties, as described elsewhere [62, 63].) Data (purple) from Refs. [93, 97].

be used to constrain the pion PDFs on $x_\pi < 10^{-3}$ at $Q^2 = 1$ GeV^2.

The potential of such measurements to expose emergent mass is greatly enhanced if one includes similar kaon experiments because the combined power of continuum and lattice QCD analyses has revealed that strange-quark physics lies at the boundary between dominance of strong (emergent) mass generation and weak (Higgs-connected) mass [68]. Hence, comparisons between distributions of truly light quarks and those describing strange quarks are well suited to exposing measurable signals of emergent mass in counterpoint to Higgs-driven effects. A striking example can be found in the contrast between the valence-quark PDFs of the pion and kaon. A significant disparity between these distributions would indicate a marked difference between the fractions of pion and kaon momentum carried by the other bound state participants, particularly gluons.

The measurement of cross sections from which one can extract GPDs and transverse-momentum-dependent parton distributions (TMDs); and, therefrom, 3-D images of hadrons, presents a fascinating new frontier within the Standard Model, promising to deliver tomographic pictures of hadron structure. JLab and COMPASS have provided us with sketches; and EicC and EIC are being designed to complete the pictures [7, 8, 84].

The key to extracting GPDs from experiment are QCD factorization theorems. DVCS cross sections and polarized asymmetries can provide detailed and precise information about GPDs, but are only sensitive to a particular flavor combination. Exclusive meson production provides key additional information allowing the separation of different quark and anti-quark flavors. To validate the meson factorization theorems and potentially extract flavor separated GPDs from experiment, one must measure the separated longitudinal and transverse cross sections and their dependence on (t, Q^2). The experimental program at JLab takes advantage of the complementarity of four experimental halls and will provide a comprehensive exclusive electroproduction data set [110]. Supposing, as accumulating evidence suggests, that a material non-zero domain in $-t$ exists whereupon one can extract physical π (K) information using the Sullivan process, then within the projected EIC luminosity reach and detection capabilities, one can envision measurements of the pion's GPD. Projected experimental results would be, at least, at the level achieved previously at HERA for the proton. Moreover, should the data validate the assumption that reliable π (K) structure data can be extracted for $-t \leq 0.6\,(0.9)$ GeV^2, then one would even gain an order-of-magnitude in statistics as compared to HERA proton data [8].

It should be recognized, however, that science faces many new challenges in extracting 3-D images from new generation experiments. Phenomenological models of a wide variety of parton distribution functions will be crucial. They will provide guidance on the size of the cross sections to be measured and the best means by which to analyze them [111]. On the other hand, as experience with meson structure functions has shown, in order to fully capitalize on such experiments, one must use computational frameworks that can veraciously connect measurements with qualities of QCD. Complementing LQCD, CSM analyses promise to fill this role because, as evidenced by calculations of meson wave functions, GPDs, and TMDs [112–115], even simplified CSM calculations can provide valuable insights.

B. Highlights and Prospects for Nucleon Collinear Parton Distributions

1. *Introduction*

There have been exciting developments recently in the study of nucleon structure at its most fundamental level in terms of the quark and gluon (or generically parton) degrees of freedom of QCD. High-quality data from modern accelerator facilities, such as the 12 GeV program at Jefferson Lab, COMPASS and LHC at CERN, and RHIC at BNL, along with plans for the future EIC [7], are pushing our knowledge of the momentum and spin distributions of the partons in the nucleon and nuclei.

With the accumulation of the new high-statistics, high-precision data comes the growing need for analysis methods that can adequately analyze the results. This is particularly important when dealing with correlations between observables and their inter-related dependence on the underlying PDFs. The standard method for obtaining information about PDFs has been through global

QCD analysis of various high-energy scattering observables, which because of QCD factorization can be described in terms of the same universal distributions [116–118].

Much has been learned, but significant questions still remain, such as the nature of the d/u valence quark distribution ratio and the quark polarizations at large parton momentum fractions x, the flavor content of the proton's sea distributions, the shape of the strange and antistrange PDFs, both unpolarized and polarized, as well as the possible modification of the PDFs in nucleons bound inside nuclei, to name just a few. In the following we summarize recent developments in the study of PDFs, both experimentally and theoretically, and outline the opportunities and challenges that are expected to arise in the near future.

2. *Modern Global QCD Analysis*

Traditional approaches to extracting PDFs have been based on the maximum likelihood method, which estimates an optimal set of parameters for some chosen parametric form of the PDFs. A major difficulty with such single-fit analyses is that, when data are scarce or the distributions are poorly known, these can introduce significant bias into the extraction. Moreover, since the χ^2 distribution is usually highly nonlinear in the parameters, it is common for local minima to exist in which a single fit can often get stuck.

To overcome these problems more sophisticated methods, such as Monte Carlo (MC) sampling, are necessary to thoroughly scan the parameter space and take into account the multiple solutions. This methodology has recently been adopted by the Jefferson Lab Angular Momentum (JAM) Collaboration [119], which has embarked on an ambitious program to *simultaneously* constrain PDFs and parton to hadron fragmentation functions (FFs) in global QCD analyses. The analyses utilize inclusive DIS, Drell-Yan lepton-pair production, and other high-energy scattering data that are sensitive to PDFs, along with SIDIS data that depend on both PDFs and FFs. To better constrain the latter, data on single-inclusive e^+e^- annihilation (SIA) are also used in the fits.

The JAM global analysis methodology implements MC algorithms that employ data resampling, with multi-step fitting strategies tailored to the specific needs of the various extractions. Previous JAM studies of collinear distributions have included an iterative MC analysis of spin-dependent PDFs of the nucleon [120], the first MC analysis of fragmentation functions from e^+e^- SIA [121], first simultaneous extraction of spin-dependent PDFs and FFs [122], simultaneous analysis of unpolarized PDFs and FFs from DIS, SIDIS and SIA data [123], and a first MC analysis of pion PDFs [124]. In the following we summarize some of these developments and how they relate to the upcoming experimental programs.

3. *Flavor Separation*

The flavor and spin decomposition of the proton's valence and sea quark PDFs provides fascinating glimpses into the non-perturbative QCD dynamics that govern quark and gluon interactions at long distances [125]. For spin-averaged PDFs, in Fig. 10 we show various flavor combinations from several recent global QCD analyses. One of the important questions addressed by the 12 GeV JLab physics program is what is the nature of the proton's d-quark PDF relative to the u-quark at large x, where most of the proton's light-cone momentum is carried by a single parton [94]. The d/u ratio has been traditionally extracted from measurements of the neutron and proton structure functions at large x, but the absence of free neutron targets has required the use of deuterons as effective neutron targets, with subsequent complications due to nuclear correction uncertainties at high x [94, 125, 126].

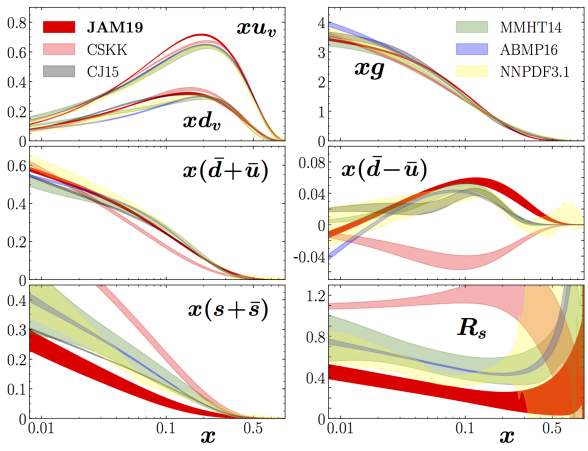

FIG. 10. Comparison of spin-averaged PDFs from various recent global QCD analyses, at a common scale $Q^2 = 4$ GeV^2, including valence quark, antiquark, and gluon PDFs, and the strange to nonstrange ratio $R_s = (s+\bar{s})/(\bar{u}+\bar{d})$ [123].

The JLab 12 GeV program addresses this problem by focusing on the construction of more effective free-neutron targets, with either spectator-tagging in electron scattering on a deuteron (BONuS in Hall B [127]) or through comparison of the isospin-mirror nuclei ^{3}He and ^{3}H (MARATHON in Hall A [128]), both of which seek to minimize the nuclear corrections. The MARATHON experiment ran in 2019, while the BONuS experiment started taking data in early 2020. The experimental setup of the BONuS experiment is shown in Fig. 11, which shows the new detector built to measure low-momentum spectator protons next to the CLAS12 detector that tags electrons scattered from a nearly free neutron.

An alternative approach proposes measuring the d-quark PDF directly using parity-violating DIS (PVDIS) from the proton [129], which is being planned as part of the SoLID detector upgrade at JLab [130]. The projected

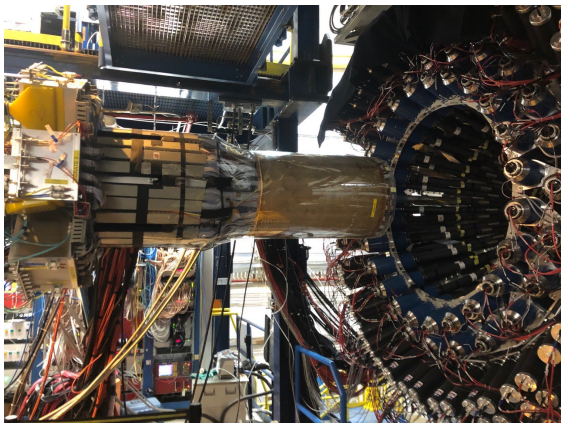

FIG. 11. BONuS radial time projection chamber being inserted into the CLAS12 detector in Hall B.

impact of all three experiments on the d/u ratio is illustrated in Fig. 12, which compares the ratio extracted from the CJ15 global analysis [126] with the expected statistical uncertainties from the experiments. Note that the error bars on the MARATHON ^{3}He/^{3}H pseudo-data do not include systematic uncertainties from theoretical approximations, which may underestimate the final uncertainties in a global QCD analysis. Nonetheless, the availability of data from all these experiments will be vital for obtaining more robust constraints on the d-quark PDF at large x.

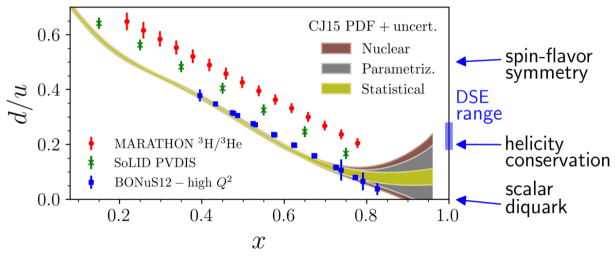

FIG. 12. Ratio of d- to u-quark PDFs from the CJ15 fit [126], including uncertainties from various sources, compared with some projections from JLab 12 GeV experiments and theoretical predictions. The uncertainties on the experiment points do not include all of the systematic and model-dependent theoretical uncertainties.

In the strange-quark sector, the quantitative nature of the strange sea has remained even more elusive. Traditionally, the strange-quark PDF has been constrained by inclusive charm meson production in charged current neutrino–nucleus DIS. Analyses of ν and $\bar{\nu}$ cross sections from Fermilab and CERN experiments have generally found a strange to nonstrange sea quark ratio $R_s = (s+\bar{s})/(\bar{u}+\bar{d}) \sim 0.5$. Unfortunately, the interpretation of the νA data suffers from uncertainties in the nuclear corrections associated with relating nuclear to free nucleon structure functions [131], and in the treatment of charm energy loss and D meson–nucleon interactions during hadronization inside the nucleus [132, 133].

From another perspective, an independent source of information on strange PDFs is SIDIS with charged final state kaons as flavor tags. A recent JAM analysis [123] performed the first simultaneous extraction of unpolarized PDFs and FFs from a combination of inclusive DIS, SIDIS, Drell-Yan, and SIA data. Inclusion of the SIDIS multiplicities in particular revealed a strong suppression of the strange PDF at $x \gtrsim 0.01$, in contrast with earlier observation of enhanced strangeness by ATLAS at the LHC [134]. This is illustrated in Fig. 10, where the $x(s+\bar{s})$ distribution and the related R_s ratio are seen to be rather smaller than other parameterizations at intermediate x values.

The SIDIS production can in principle also discriminate between the s and $\bar{s}$ PDFs through tagging of K^+ vs. K^- mesons, although existing data are not precise enough to allow this discrimination. Future high-precision SIDIS data from Jefferson Lab or EIC should allow more stringent determinations of the s and $\bar{s}$ PDFs [135], along with PVDIS, as would W + charm production in pp collisions [136].

4. *Spin-Dependent Structure*

The decomposition of the proton's spin into its quark and gluon helicity and orbital angular momentum components has been one of the driving problems in hadron physics for the past three decades [137]. While the behavior of the polarized Δu and Δd distributions has been reasonably well established at moderate x values, as seen in Fig. 13, the shape, and even sign, of the strange-quark polarization Δs is much more uncertain. Moreover, even for the non-strange spin distributions, there are significant uncertainties in kinematic regions, such as at large x, where data are scarce.

The latter observation is rather pertinent, given that polarized PDFs are quite sensitive to the details of nonperturbative quark-gluon dynamics in the nucleon at high x [125]. To address these questions a comprehensive program of high-x spin structure function measurements for the proton, deuteron and ^{3}He has been initiated in JLab Halls B and C, the latter taking data since Fall of 2019. These measurements will also improve the determination of higher twist contributions to structure function moments, and test quark-hadron duality in the spin sector.

For strange quarks, the results of the combined analysis [122] of polarized DIS, SIDIS and SIA data in Fig. 13, which was the first performed *without* imposing flavor SU(3) symmetry, indicate that Δs is small across all x, within large uncertainties. This turns out to be largely due to the SIDIS K^- production data, which are most sensitive to strange quark spin. The K^- polarization asymmetry computed with a negative Δs, for instance, gives a significantly worse description of the data than the full result in Fig. 13. Of course, preference for a positive or negative Δs depends on the FFs used in the evaluation of the asymmetry, so the solution is clearly

to simultaneously determine both PDFs and FFs, as was performed in Ref. [122]. Upcoming SIDIS K production data from JLab will be helpful in further constraining the shape of Δs, and the future EIC offers the possibility of performing polarized PVDIS to obtain unique sensitivity to strange quark polarization [129, 138].

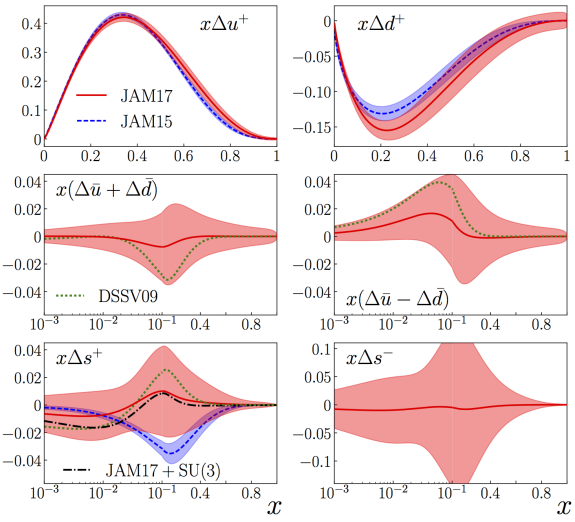

FIG. 13. Comparison of spin-dependent PDFs from various recent global QCD analyses, at a common scale $Q^2 = 1$ GeV^2 [122].

5. *PDFs from Lattice QCD*

Complementing the experimental and phenomenological developments in PDF studies, recent progress in lattice QCD simulations of parton quasi-distributions (qPDFs) [99, 139] and pseudo-distributions [140] is paving the way towards the study of the x dependence of PDFs from first principles. The observables accessible in lattice calculations are matrix elements of nonlocal operators, such as $h(z) = \langle N|\bar{\psi}(0,z)\Gamma W_3(z)\psi(0,0)|N\rangle$, which can be related to the PDFs via a Fourier transform and matching the off-light-cone qPDFs to the physical PDFs. An example of such simulations is shown in Fig. 14 for the isovector unpolarized $u-d$ and polarized $\Delta u - \Delta d$ combinations from the ETM Collaboration [140].

A new approach currently being developed [141] combines global QCD analysis of experimental data with lattice results for $h(z)$, within the same analysis framework. The comparison in Fig. 14 illustrates that the recent lattice data [140] for the spin-dependent $\Delta u - \Delta d$ PDFs are reasonably compatible with the empirical results, while some systematic discrepancies exist for the more precise spin-averaged $u-d$ PDFs. The convergence of the phenomenological and lattice results is currently an active area of research.

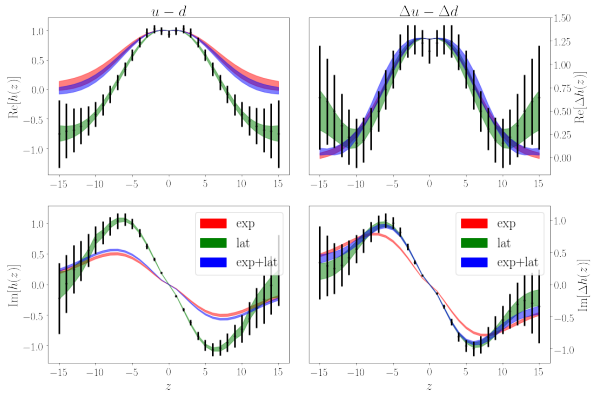

FIG. 14. Lattice QCD simulations (green lines) of the real (top row) and imaginary (bottom row) parts of nonlocal matrix elements of twist-2 operators for unpolarized $u-d$ (left column) and polarized $\Delta u - \Delta d$ PDFs (right column), compared with phenomenological fits to experimental data (red lines) and fits to experimental + lattice data (blue lines) [141]. The real and imaginary parts of the matrix elements are sensitive to different combinations of quark and antiquark PDFs.

C. Strong QCD Insights from N^* Structure Studies with EM Probes

Studies of the structure of excited nucleon states in terms of the Q^2-evolution of the $\gamma_v pN^*$ electrocouplings represents the only source of information on many facets of strong QCD that underlie the generation of these N^* states with different quantum numbers and with distinctively different structural features. Continuum QCD approaches [142–147] and most quark models [148–152], which reproduce the nucleon elastic form factors equally well, predict different behaviors for the $\gamma_v pN^*$ electrocouplings. Confronting theory expectations on the $\gamma_v pN^*$ electrocouplings with the data, allows us for insight into how resonances of different structure emerge from QCD. The data on the $\gamma_v pN^*$ electrocouplings are of particular importance for gaining insight into the strong QCD dynamics that underlie hadron mass generation. Advances in continuum QCD approaches [50, 153] make it possible to describe the momentum dependence of the dressed quark mass (*i.e.* the so-called dressed quark mass function), starting from the QCD Lagrangian.

Consistent results on the dressed quark mass function from independent analyses of the data on the nucleon elastic form factors and the $\gamma_v pN^*$ electrocouplings of different resonances with a core of three dressed quarks in different radial, spin-isospin-flip, and orbital excitations, will validate credible access to the dynamics responsible for hadron mass generation. The N^* program with the CLAS12 detector [43, 154] will allow us to map out the dressed quark mass function at the distances where the transition between the almost bare, massless QCD-quarks and fully dressed constituent quarks of ≈400 MeV mass is expected, addressing the key open question of the Standard Model on the emergence of >98% of hadron

mass from QCD [68].

1. $\gamma_v pN^*$ Electrocouplings from Exclusive Meson Production and Their Impact on the Exploration of the Ground State Nucleon PDFs

The transverse $A_{1/2}(Q^2)$, $A_{3/2}(Q^2)$, and longitudinal $S_{1/2}(Q^2)$ $\gamma_v pN^*$ electrocouplings have been extracted from the measured differential cross sections and polarization asymmetries for the exclusive meson electroproduction channels by fitting the data within several different reaction models. A successful fit of the data allows us to isolate the resonant contributions for the extraction of the resonance parameters. Consistent results on the $\gamma_v pN^*$ electrocouplings from the independent analyses of the exclusive channels with different non-resonant contributions validates the credible extraction of these quantities. The CLAS detector has produced the dominant part of the available world-wide data on all of the relevant meson electroproduction channels off the nucleon in the resonance region for Q^2 up to 5.0 GeV^2 [4]. The data are stored in the CLAS Physics Database [155]. So far, most of the results on the $\gamma_v pN^*$ electrocouplings have been extracted from independent analyses of $\pi^+ n$, $\pi^0 p$, ηp and $\pi^+\pi^- p$ electroproduction data off the proton [4, 6, 21, 156–159]. The parameterization of the $\gamma_v pN^*$ electrocouplings for $Q^2 < 5.0$ GeV^2 can be found in Ref. [160].

The $\gamma_v pN^*$ electrocouplings from the πN electroproduction data were determined from analyses of a total of nearly 160,000 data points (d.p.) on unpolarized differential cross sections, longitudinally polarized beam asymmetries, and longitudinal target and beam-target asymmetries within two conceptually different approaches: a Unitary Isobar Model (UIM) and Dispersion Relations (DR) [4, 156]. The $\pi^+\pi^- p$ electroproduction data from CLAS [6] provide information on nine independent single differential and fully integrated cross sections binned in W and Q^2 in the mass range $W < 2.0$ GeV and for Q^2 from 0.25 – 5.0 GeV^2. The $\gamma_v pN^*$ electrocouplings of most N^* in the mass range up to 1.8 GeV have become available from analyses of $\pi^+\pi^- p$ electroproduction data within the data driven meson-baryon model JM [5, 21, 159, 161, 162]. A good description of the $\pi^+\pi^- p$ differential cross sections for $W < 2.0$ GeV and Q^2 from 0.2 – 5.0 GeV^2 has been achieved with $\chi^2/d.p. < 3.0$ accounting only for the data statistical uncertainties [6].

Consistent results on the $\gamma_v pN^*$ electrocouplings for the $N(1440)1/2^+$ and $N(1520)3/2^-$ resonances, which have been determined in independent analyses of the dominant meson electroproduction πN and $\pi^+\pi^- p$ channels demonstrate that the extraction of these quantities is reliable (see Fig. 15). The results on the $\gamma_v pN^*$ electrocouplings from the CLAS data analysis have been published in the recent PDG edition [1].

For the first time, the resonance contributions for inclusive electron scattering has been evaluated based on the experimental results in Ref. [160]. A realistic accounting of these contributions is of particular importance in order to gain insight into the parton distributions of the ground state nucleons at large values of the Bjorken variable x_B. A gradual extension of the experimental results for the $\gamma_v pN^*$ electrocouplings towards higher W and Q^2 from CLAS/CLAS12, as well as from Halls A/C on the transverse and longitudinal inclusive cross sections will extend the knowledge of the nucleon parton distributions at large x_B. The novel pseudo- and quasi-PDF concepts [163, 164], which make it possible to relate the PDFs to the QCD Lagrangian, are helping to drive the exploration of PDFs, including the resonant region at large x_B. The studies of the resonant contributions in inclusive electron scattering represent an important step in the exploration of 1D nucleon in synergistic efforts in Halls A, B, and C, JPAC, and the JLab Theory Center.

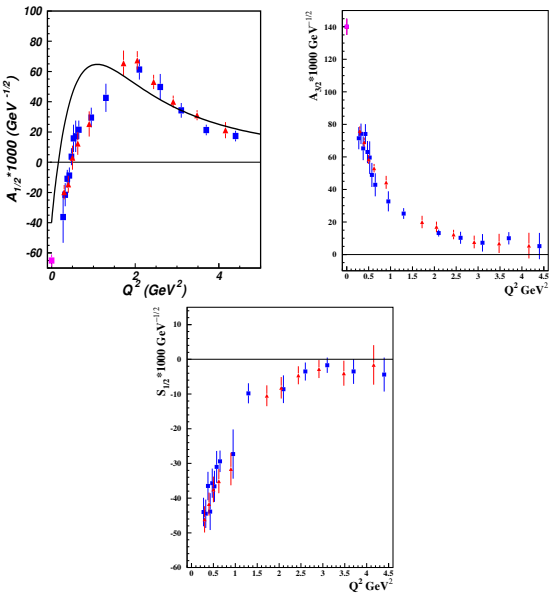

FIG. 15. $\gamma_v pN^*$ electrocouplings $A_{1/2}$ of the $N(1440)1/2^+$ (UL), $A_{3/2}$ (UR), and $S_{1/2}$ (bottom) of $N(1520)3/2^-$ resonances vs. Q^2 from the studies of πN [156, 157] (red triangles) and $\pi^+\pi^- p$ [6, 21, 159] (blue squares) electroproduction data from CLAS. The $N(1440)1/2^+$ $A_{1/2}$ electrocouplings computed within the continuum QCD approach [20] starting from the QCD Lagrangian are shown by the curve in the UL plot.

The experimental results on the $\gamma_v pN^*$ electrocouplings also offer important information for the development of the novel $N \to N^*$ transition GPD concepts. This is a promising new avenue in gaining insight into strong QCD from the data on the structure of excited nucleon states in 3D. The development of reaction models relating the transition GPDs to observables is needed in order to access this information from the CLAS12 data.

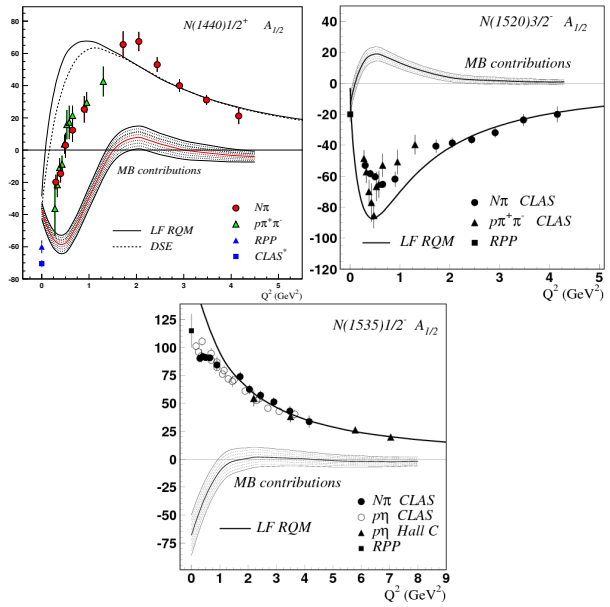

FIG. 16. The quark core and meson-baryon cloud contributions to the $A_{1/2}$ electrocouplings of the $N(1440)1/2^+$ (UL), $N(1520)3/2^-$ (UR), and $N(1535)1/2^-$ (bottom) resonances. The quark core contributions for the $N(1440)1/2^+$ were computed within the continuum QCD approach [2] (dashed line). For each of the states the quark core contributions were obtained from the light-front quark model [40, 149] (solid line).

The analyses of the CLAS results on the $\gamma_v pN^*$ electrocouplings within the continuum QCD approach [2, 16, 20, 144–147, 165] and different quark models [40, 149, 150, 166] have revealed N^* structure for $Q^2 < 5.0$ GeV^2 as a complex interplay between an inner core of three dressed quarks and an external meson-baryon cloud. Representative examples for the contributions from the quark core and the meson-baryon cloud to N^* structure are shown in Fig. 16. The relative contributions of the meson-baryon cloud depend strongly on the quantum numbers of the excited nucleon state. For all resonances studied using CLAS data, this contribution decreases with Q^2 in a gradual transition towards quark-core dominance for $Q^2 > 5.0$ GeV^2. Understanding the emergence of the meson-baryon cloud from the quark core represents an important avenue in the exploration of strong QCD. In order to address this problem, analyses of the data on the $\gamma_v pN^*$ electrocouplings at Q^2 where both the quark core and the meson-baryon cloud contribute is needed to bridge the efforts between the multichannel amplitude analyses of meson photo-, electro-, and hadroproduction [167, 168] and the N^* quark models [148–152]. Modeling of both components of the N^* structure has been forged by the advances in the AdS/CFT approaches that have provided a successful description of the CLAS results on the $N(1440)1/2^+$ and $N(1535)1/2^-$ electrocouplings [169, 170] for $Q^2 < 5.0$ GeV^2. The studies of the transition between the confined quarks in the quark core and the deconfined mesons and baryons in the external cloud are of particular interest for LQCD as it is the only approach with the potential to account for the effects of all relevant degrees of freedom in the N^* structure.

The electrocouplings of the $N(1440)1/2^+$ and $\Delta(1232)3/2^+$ resonances were evaluated starting from the QCD Lagrangian within the continuum QCD approach [16, 20]. The predictions for the $N(1440)1/2^+$ state are shown in Fig. 15 (solid line). In the range of applicability, $Q^2 > 2.0$ GeV^2, the approach [20] offers a good description of the experimental results on the $N(1440)1/2^+$ electrocouplings, which was achieved with *exactly the same* dressed quark mass function as that employed in the evaluations of the electromagnetic elastic nucleon form factors and the magnetic $p \to \Delta(1232)3/2^+$ transition form factor [16]. This success conclusively demonstrates the capability of gaining insight into the strong QCD dynamics underlying the dominant part of hadron mass generation from the experimental results on the nucleon elastic form factors and the $\gamma_v pN^*$ electrocouplings.

In the upcoming experiments with the CLAS12 detector [43], the electrocouplings of all prominent nucleon resonances will become available at the highest photon virtualities (Q^2 from 5 – 12 GeV^2) ever achieved in the studies of exclusive electroproduction, allowing us to map out the dressed quark mass function for distances where the transition between the pQCD and strong QCD regimes is expected. Consistent results on dressed quark mass function from independent studies of the electrocouplings of the resonances of distinctively different structure will validate credible access to this key ingredient of strong QCD, addressing one of the most important open questions of the Standard Model on the emergence of >98% of hadron mass from QCD and quark-gluon confinement [171]. The results on the $\gamma_v pN^*$ electrocouplings for all prominent N^* will offer insight into the qq correlations in the resonances of different spin-parities. This information will enable us to predict the wave functions of the mesons consisting of $q\bar{q}$ with the same spin and opposite parity as for the qq correlations from N^* studies, emphasizing the need to combine the efforts in the exploration of both meson [8] and baryon [171] structure.

With the dressed quark mass function and the qq-correlation amplitudes checked against the experimental results on the nucleon elastic form factors and the $\gamma_v pN^*$ electrocouplings, the continuum QCD approaches are capable of evaluating the Faddeev amplitude for the ground state nucleon state. The light-front wave function that contains the complete information on ground state nucleon structure can be computed from the Faddeev amplitude. Obtained in this way, the ground state nucleon light-front wave function can be used for the exploration of the intrinsic nucleon deformation. This will improve our understanding on the emergence of atomic nuclear structure from strong QCD by employing the symmetry-

driven solution of the many-body nuclear physics problem [13]. Decomposition of the nucleon light-front wave function over eigenvectors of the Elliot SU(3) irreducible representations will deliver full information on the nucleon shape. The intrinsic nucleon deformation can also be identified from the non-zero value of the computed TMD-pretzelosity that can be measured in semi-inclusive DIS experiments.

Continuum QCD approaches offer the prospect of evaluating all of the chiral-even and chiral-odd GPD structure functions (H, E, $\tilde{H}$, $\tilde{E}$) from the ground state nucleon Faddeev amplitude [172]. These GPD structure functions predicted from analyses of the data on the nucleon elastic form factors and the $\gamma_v pN^*$ electrocouplings can be plugged into models that relate the GPDs to the DVCS and DVMP observables. The predicted DVCS and DVMP cross sections, as well as the beam-, target-, and beam-target asymmetries for the longitudinal and the transverse target polarizations, can be confronted with the experimental data that will be available from the experiments with CLAS12 and in Halls A/C [43]. Consistent results on the dressed quark mass function and the different qq-correlations inferred from data analyses in the two independent and complementary experimental areas, i) nucleon elastic form factors and $\gamma_v pN^*$ electrocouplings and ii) studies of the ground state nucleon structure in 3D, will validate the credible insight into strong QCD underlying the generation of the ground and excited state nucleons in a nearly model independent way.

Therefore, continuum QCD approaches [2, 8, 143, 153] offer a sound theoretical framework for the interpretation of the results on the ground and excited state nucleon structure aimed at gaining insight into strong QCD dynamics underlying the generation of hadrons composed of light u and d quarks with a traceable connection to QCD. These approaches also allow for the exploration of the emergence of atomic nuclear structure from strong QCD.

D. Insight into 3D Structure of the Ground State Nucleons in Impact Parameter Space from DVCS and DVMP

It is now well recognized [173–176] that deeply virtual Compton scattering, *i.e.* the process $ep \to e'p'\gamma$, is most suitable for accessing the twist-2 vector GPDs H, E and the axial GPDs $\tilde{H}$, $\tilde{E}$ in x, ξ, and t. Here ξ is the longitudinal momentum transfer to the struck quark, and t the four-momentum transfer to the nucleon. Having access to a 3-dimensional image of the nucleon (two dimensions in transverse space, one dimension in longitudinal momentum) opens up completely new insights into the complex internal structure and dynamics of the nucleon that, eventually, QCD must reproduce.

The beam helicity dependent cross section asymmetry is defined as $A_{LU} = \Delta\sigma_{LU}/2\sigma$, where $\Delta\sigma_{LU}$ is the cross section difference for electron spin parallel and spin antiparallel, respectively. In leading twist $\Delta\sigma_{LU}$ is given by 3 GPDs H, $\tilde{H}$ and E and two form factors as:

$$\Delta\sigma_{LU} \propto \sin\phi[F_1 H + \xi(F_1 + F_2)\tilde{H}]d\phi \ ,$$

where ϕ is the azimuthal angle between the electron scattering plane and the hadronic production plane. The kinematically suppressed term with GPD E is omitted. $F_1(t)$ and $F_2(t)$ are the well-known Dirac and Pauli form factors. The asymmetry is mostly sensitive to the GPD $H(x,\xi,t)$. In a wide kinematics [177, 178] the beam asymmetry A_{LU} was measured at Jefferson Lab at modestly high Q^2, ξ, and t, and in a more limited kinematics [179] the cross section difference $\Delta\sigma_{LU}$ was measured with high statistics. Moreover, the first measurements of the target asymmetry $A_{UL} = \Delta\sigma_{UL}/2\sigma$ were carried out [180–182], where

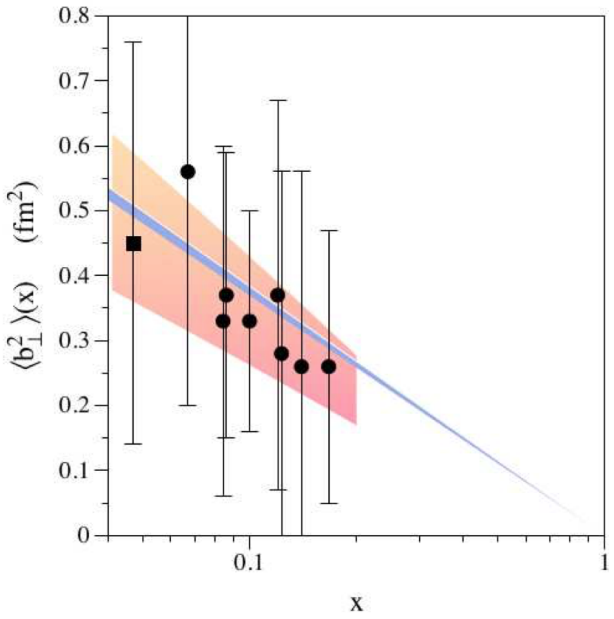

FIG. 17. The impact parameter $b_\perp^2$ as a function of the quark momentum fraction x. The negative slope of the points is an indication of the decrease of the protons transverse size with increasing quark momentum x.

$$\Delta\sigma_{UL} \propto \sin\phi[F_1\tilde{H} + \xi(F_1 + F_2)H] \ . \quad (1)$$

The combination of A_{LU} and A_{UL} allows the separation of GPD $H(x=\xi,\xi,t)$ and $\tilde{H}(x=\xi,\xi,t)$. Using a transversely polarized target the asymmetry $A_{UT} = \Delta\sigma_{UT}/2\sigma$, with:

$$\sigma_{UT} \propto \cos\phi\sin(\phi-\phi_s)\frac{t}{4M^2}(F_2 H - F_1 E)$$

can be measured, where ϕ_s is the azimuthal angle of the target polarization vector relative to the electron scattering plane. A_{UT} depends in leading order on GPD E. Measurement of A_{UT} is the most efficient and most direct way to determine the GPD E, as H will be well

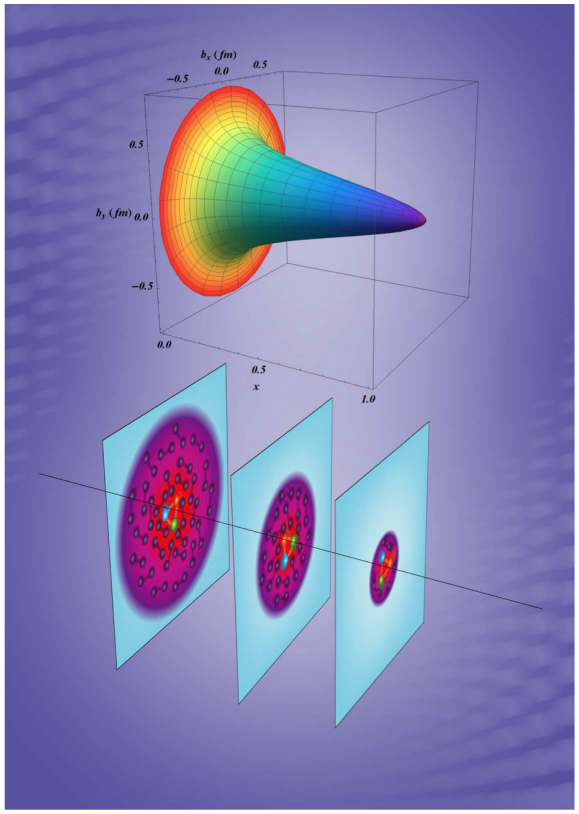

FIG. 18. The 3D image of the valence quarks in the proton versus quark fractional momentum x using the data and fit parameters shown in Fig. 17.

constrained by the other polarization observables $\Delta\sigma_{LU}$ and $\Delta\sigma_{UL}$.

First DVCS experiments carried out at JLab [177, 179, 183] and DESY [184] showed results in terms of the applicability of the handbag mechanism to probe GPDs. The 12 GeV upgrade offers much improved possibilities for validating the dominance of the handbag mechanism, and accessing the GPDs.

Measurements of all 3 asymmetries and the unpolarized cross section will enable the separation of GPDs H, $\tilde{H}$, and E at some specified kinematics. To obtain a complete picture of the quark distribution in the nucleon, the GPDs need to be measured for both flavors u-quarks and d-quarks. This requires measurement of DVCS not only on the proton but also on the neutron. Experiment [185] will measure the beam-spin asymmetry for the neutron. If the t-dependences are known, a Fourier transformation of, *e.g.* GPD $H^u(x=\xi,t)$ gives information about the u-quark distribution in impact parameter space. Similarly for GPD $\tilde{H}^d$ and GPD E^d.

An essential aspect of DVCS measurements is the promise that 3D images of the nucleon may be extracted once high precision data are available covering a large part of the phase space in x_B, t, and Q^2, and to have these data collected with polarized lepton beams, with longitudinally and with transverse polarized nucleon targets. While some of the required measurements are currently underway, the information currently available is not sufficient for a full analysis with no or only minimal external constraints. The covered kinematics in x_B and in t is too limited for such an analysis. Nevertheless attempts have been made to get a first glimpse of the 3D structure of the proton [186]. Results of this analysis, that uses all available DVCS data, are shown in Fig. 17. The impact parameter $b_\perp^2$ is plotted as a function of the quark momentum fraction x. The negative slope of the fit indicates a decrease in the transverse space the quarks occupy with increasing quark momentum.

This information can be employed to extract a 3D image of the proton's quark distribution a function of the quark x momentum fraction, which is presented in Fig. 18.

Although these images are based on experimental data, the results include large uncertainties from insufficient kinematic coverage and incomplete data. It is therefore desirable to carry out analyses of generated data that include all expected future data with their coverage and expected statistical and systematic uncertainties. This has been done in a trial study [187]. In this study the Compton Form Factors $\mathcal{H}(\xi,t)$ and $\mathcal{E}(\xi,t)$ were extracted from the simulated data. They are shown in Fig. 19.

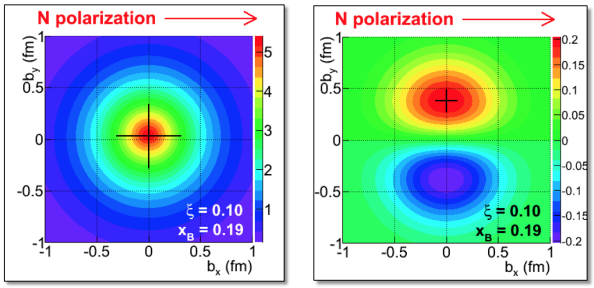

FIG. 19. The quark distributions in impact parameter space at fixed value of x_B based on the CFF $\mathcal{H}+\mathcal{E}$ (left) for a transversely polarized target. The direction of the nucleon polarization is indicated by the arrow on top. The slight vertical shift of the center point is due to the non-zero value of $\mathcal{E}$. The right panel shows the quark distributions as projected from the CFF $\mathcal{E}$ separately, indicating an induced electric dipole moment due to the positive and negative charged quarks shifting in opposite directions. The graphs are extracted from simulated data weighted with the expected uncertainties for all projected measurements with polarized electron beams, longitudinally and transverse polarized targets.

GPDs are encoded in the off-forward matrix elements of two currents separated along the light cone. The formulation of lattice QCD in Euclidean space precludes their direct calculation, and therefore the approach of exploiting the operator product expansion to express the moments with respect to Bjorken x as the matrix elements of local operators that are accessible to calcula-

tion on a Euclidean lattice, yielding Generalized Form Factors [188–191]. These computations have provided important information on the three-dimensional imaging of the nucleon, notably in the decomposition of angular momentum within the nucleon [188, 189].

Recently, approaches have been adopted that enable the x-dependent distributions to be systematically related to quantities that are amenable to calculation on a Euclidean lattice; these approaches are described in detail in Section VI. These methods can be applied to the computation of GPDs [192]

While DVCS is regarded as the most promising exclusive channel for constraining the nucleon GPDs in leading order, DVMP has evolved into a dynamic field giving access to higher twists as well as to the GPD flavor decomposition. GPDs admit a particularly intuitive physical interpretation at zero skewness, where after a Fourier transform GPDs describe the spatial distribution of quarks with given longitudinal momentum in the transverse plane. There are eight independent twist-two GPDs, four correspond to parton helicity-conserving (chiral-even) processes, denoted by H^q, $\tilde{H}^q$, E^q and $\tilde{E}^q$, and four correspond to parton helicity-flip (chiral-odd) processes, H_T^q, $\tilde{H}_T^q$, E_T^q, and $\tilde{E}_T^q$ [193]. The chiral-odd GPDs are difficult to access since subprocesses with quark helicity-flip are usually strongly suppressed. By this reason very little is known about the chiral-odd GPDs. One of which, H_T, is related to the transversity distribution $H_T^q(x,\xi=0,t=0)=h_1^q(x)$ and the tensor charge $\kappa_T^q=\int dx\, H_T^q(x,\xi,t=0)$ while $\bar{E}_T$ is related to the anomalous tensor magnetic moment of the nucleon $\delta_T^q=\int dx\, \bar{E}_T^q(x,\xi,t=0)$.

The DVMP processes $\gamma^* N \to MN$ may include the exchange of vacuum quantum numbers in the t-channel and non-vacuum exchanges. To the first class we can assign the processes with $M=\rho^0,\omega,\phi,J/\psi,\Upsilon$, where we can access the gluon GPDs. The second class $M=\pi^0,\pi^+,\rho^+,K^+,K^*$ gives us access to the valence quark GPDs. The variety of reactions with mesons with different quark contents gives us the opportunity to make the GPD flavor decomposition.

The special attention was attracted to the pseudoscalar meson production such as $\gamma^*(p/n)\to(\pi^0/\eta)(p/n)$. The early efforts to explain π^0/η electroproduction focused on the chiral even (no helicity flip) GPDs, $\tilde{H}$ and $\tilde{E}$, as a means to parameterize only the longitudinal virtual photon amplitudes. However, these predictions were an order of magnitude lower than the recent experimental results [194–199]. During the past few years, several approaches [200–204] have been developed utilizing chiral odd GPDs in the calculation of pseudoscalar electroproduction. It was found that the the contribution from transverse polarized photons is strongly enhanced by the chiral condensate for pseudoscalar mesons. The role of the transversity GPDs, H_T and $\bar{E}_T=2\tilde{H}_T+E_T$, has been examined and a strong increase of the π^0/η cross section found. This conclusion was supported by the recent Rosenbluth separation of the structure functions σ_L and σ_T [197, 198] where it was found that the contribution of transverse σ_T is dominant. The structure functions in the electroproduction of the pseudoscalar mesons read

$$\frac{d\sigma_T}{dt}=\frac{4\pi\alpha}{2kQ^4}\left[\left(1-\xi^2\right)\left|\mathcal{H}_T(\xi,t)\right|^2-\frac{t'}{8m^2}\left|\bar{\mathcal{E}}_T(\xi,t)\right|^2\right]$$

$$\frac{d\sigma_{TT}}{dt}=\frac{4\pi\alpha}{kQ^4}\frac{t'}{16m^2}\left|\bar{\mathcal{E}}_T(\xi,t)\right|^2$$

The generalized form factors $\mathcal{H}_T(\xi,t)$ and $\bar{\mathcal{E}}_T(\xi,t)$ denote the convolution of the elementary process $\gamma^* q\to q\pi^0$ with the GPDs H_T and $\bar{E}_T$. As shown in the formulae above the form factors $\mathcal{H}_T(\xi,t)$ and $\bar{\mathcal{E}}_T(\xi,t)$ are directly accessible from the experimental observables σ_T and σ_{TT} [205, 206].

In contrast to the form factors $\mathcal{H}_T(\xi,t)$ and $\bar{\mathcal{E}}_T(\xi,t)$ there is no direct way to get along without models for the GPDs in order to describe data on hard exclusive reactions. One such parameterization was presented in Ref. [201]. The proposed model is physically motivated on one hand by Regge phenomenology in the limit $x\to 0$ and, on the other hand, by the physical intuition gained in the impact parameter representation of GPDs. The main feature of this ansatz is an exponential t behavior $\bar{E}^q(x,\xi=0,t)=N^q x^{-\alpha_0^q}(1-x)^{n^q}\exp[t(b^q-\alpha'^q\ln x]$. The ξ-dependence is generated by the double distribution representation of the GPDs [207]. There are 4 parameters for each quark flavor in the model. The $\bar{E}_T$ parameters for u and d-quarks were determined in the global fit of all available data from CLAS, Hall A, and COMPASS [194–199] on the σ_{TT} structure functions for the reactions $ep\to e'(\pi^0/\eta)p'$ and $en\to e'\pi^0 n'$. According to Refs. [208, 209], the Fourier transform of $\bar{E}_T$

$$\bar{E}_T(x,\vec{b})=\int\frac{d^2\vec{\Delta}}{(2\pi)^2}e^{-i\vec{b}\cdot\vec{\Delta}}\bar{E}_T(x,t=-\Delta^2).$$

controls the density of polarized quarks in the unpolarized nucleon

$$\delta(x,\vec{b})=\frac{1}{2}[H(x,\vec{b})-\frac{b_y}{m}\frac{\partial}{\partial b^2}\bar{E}_T(x,\vec{b})].$$

The transverse density of polarized quarks in an unpolarized proton, based on the global fit of the world data, is presented in Fig. 20 [206]. This density depends on two GPDs $H(x,\vec{b})$ and $E_T(x,\vec{b})$. The GPD $H(x,\vec{b})$ describes the density of unpolarized quarks and $\bar{E}_T(x,\vec{b})$ is related to the distortion of the polarized quarks in the transverse plane. Note that the width of the quark cloud is diminished as $x\to 1$. This behavior is typical for the GPD models. The visible vertical shift in the positive b_y direction of the center point is due to $\bar{E}_T$ that has the same sign for both u and d-quarks.

The study of the pseudoscalar electroproduction is ongoing at Jefferson Lab using data sets that were collected

during 2018-2020 years with higher statistics and kinematic reach. Extracting $d\sigma_L/dt$ and $d\sigma_T/dt$ and performing new measurements with transversely and longitudinally polarized targets would also be very useful, and are planned for the future Jefferson Lab at 12 GeV. The measurement of beam and target spin asymmetries can provide further constraints on the theoretical handbag models considered here. The physics community is actively planning DVMP experiments at the EIC that will definitely expand our understanding of the nucleon structure.

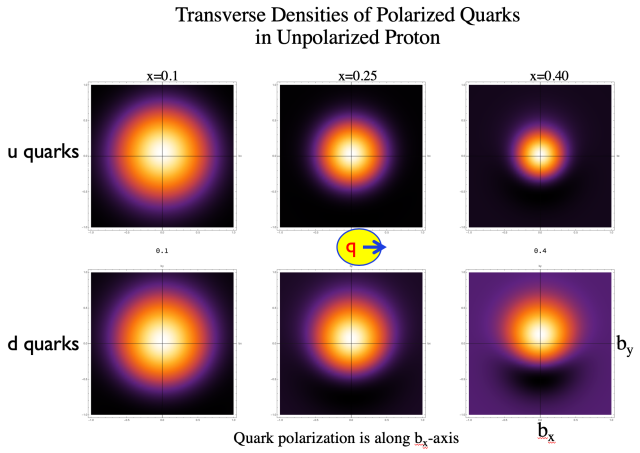

FIG. 20. The impact parameter density of the transversely polarized quarks along the b_x-axis in an unpolarized proton for Feynman $x = 0.1$, $x = 0.25$ and $x = 0.40$, u-quarks distributions are in the top row and d-quarks in the bottom row. The quark polarization is indicated by the arrow in the middle of the figure. The density depends on $H(x,\vec{b})$ and $E_T(x,\vec{b})$ as $\delta(x,\vec{b}) = \frac{1}{2}[H(x,\vec{b}) - \frac{b_y}{m}\frac{\partial}{\partial b^2}\bar{E}_T(x,\vec{b})]$. The $E_T(x,\vec{b})$ parameters were determined by the global fit of the world data on the π^0/η electroproduction out of the proton and neutron. The GPD $H(x,\vec{b})$ describes the density of unpolarized quarks and $\bar{E}_T(x,\vec{b})$ is related to the distortion of the polarized quarks in the transverse plane. Note that the width of the quark cloud is diminished as $x \to 1$. The visible vertical shift of the center point is due to $\bar{E}_T$.

E. Insight into 3D Structure of the Ground State Nucleons in Momentum Space from SIDIS

SIDIS data enables us to build 3D maps of the partonic structure of nucleons in momentum space. In fact, by measuring the transverse momentum P_{hT} (with respect to the virtual photon direction) of an inclusively produced hadron h we can reconstruct the transverse momentum k_T of the confined parton, provided that a suitable factorization theorem holds. The necessary condition for this to happen is $P_{hT}/z \ll Q$, where z is the fraction of the fragmenting parton energy carried by h, and Q is the four-momentum of the virtual photon, the SIDIS hard scale [210–213]. Namely, factorization holds if SIDIS is a two-scale process.

In this case, the cross section can be factorized into a hard photon-absorption vertex and two non-perturbative objects, one describing the probability density of finding in the nucleon a parton with k_T and longitudinal momentum fraction x, one describing the probability density for a parton to fragment into the observed hadron with z and P_{hT}. These non-perturbative objects are called TMD PDFs and fragmentation functions (TMD FFs), respectively; in short TMDs. In Fig. 21, we list all the leading-twist TMD PDFs for quarks; an analogous table can be formed for TMD FFs [214, 215]. Each entry in the table corresponds to a specific polarization status of the quark and of the parent nucleon. The asterisks denote combinations that are forbidden by invariance under parity transformations. Building a 3D map for each entry can expose details of spin-spin, spin-momentum (spin-orbit) partonic correlations, as well as correlations between the partonic motion and nucleon spin. An even richer table can be made at subleading twist to explore quark-gluon dynamical correlations. However, no factorization theorem is available yet at this level although conjectures towards it have been recently published [216].

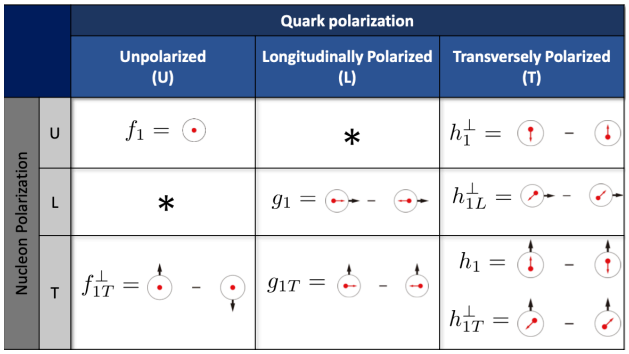

FIG. 21. Table of all leading-twist TMD PDFs of a quark in a spin-1/2 hadron depending on quark polarization (columns: U - unpolarized, L - longitudinally polarized, T - transversely polarized) and hadron polarization (rows U, L, T, with same meaning). Horizontal (vertical or slanted) arrows indicate longitudinal (transverse) polarization. Red arrows for quark, black arrows for hadron. Asterisks denote combinations forbidden by invariance under parity transformations.

Factorization in the TMD framework holds also for other processes like e^+e^- annihilation and production of Drell-Yan lepton pairs (for a review, see Ref. [212]), making it possible to separately test the universality of TMD PDFs and TMD FFs. Factorization is explicitly broken for inclusive hadron production in hadronic collisions [217]. An alternative approach has been recently suggested to detect hadrons inside jets, because in this hybrid framework the cross section factorizes in terms of the same universal TMD FF and a collinear PDF [218].

Evolution of TMDs is more complicated than in the collinear framework. In the CSS scheme [212, 219], the evolution operator contains a perturbative part and a

non-perturbative part. The perturbative component of the operator resums all logarithms of q_T/Q connected to soft gluon radiation, where $q_T = P_{hT}/z$. This component can be calculated nowadays at a level of sophistication comparable to the most refined phenomenological analyses at LHC [220, 221]. But f or very small parton k_T, the perturbative description breaks down. The non-perturbative component must take over, and a prescription for a smooth transition between the two regimes is needed. Both the non-perturbative part of the evolutor and the transition prescription can be described in an arbitrary way and depend on parameters to be fitted to data (the same holds also for other schemes [213, 222, 223]). Moreover, matching the TMD framework at $q_T \ll Q$ to fixed-order calculations in collinear framework at $q_T \lesssim Q$ is still an open problem [224–227]. Therefore, it is important to have experimental data sensitive to transverse momenta that span a large portion of phase space in Q^2 and also x.

	Framework	HERMES	COMPASS	DY	Z production	N of points
Pavia 2013 arXiv:1309.3507	parton model	✔	✘	✘	✘	1538
Torino 2014 arXiv:1312.6261	parton model	✔ (separately)	✔ (separately)	✘	✘	576 (H) 6284 (C)
DEMS 2014 arXiv:1407.3311	NNLL	✘	✘	✔	✔	223
EIKV 2014 arXiv:1401.5078	NLL	1 (x,Q^2) bin	1 (x,Q^2) bin	✔	✔	500 (?)
SIYY 2014 arXiv:1406.3073	NLL′	✘	✔	✔	✔	200 (?)
Pavia 2017 arXiv:1703.10157	NLL	✔	✔	✔	✔	8059
SV 2017 arXiv:1706.01473	NNLL′	✘	✘	✔	✔ (LHC)	309
BSV 2019 arXiv:1902.08474	NNLL′	✘	✘	✔	✔ (LHC)	457
Pavia 2019 arXiv:1912.07550	up to N^{3}LL	✘	✘	✔	✔ (LHC)	319
SV 2019 arXiv:1912.06532	ζ prescription up to N^{3}LO	✔	✔	✔	✔ (LHC)	1039

FIG. 22. The most recent extractions of unpolarized TMD PDF $f_1(x, k_T^2)$ from data on SIDIS unintegrated multiplicities provided by the HERMES (H) and COMPASS (C) collaborations, and/or cross sections for the production of Drell-Yan lepton pairs (DY) or Z-boson. In the second left column, the corresponding accuracy in the description of the perturbative component of TMD evolution is indicated: resummation of soft gluon radiation up to next-to-leading log precision (NLL), next-to-next-leading log (NNLL), next-to-next-to-next-leading log (N^{3}LL), and slight variations of them indicated by NLL' and NNLL', respectively [220]. The last entry in the bottom box refers to the specific ζ prescription by the corresponding authors that amounts to a next-to-next-to-next-leading order (N^{3}LO) perturbative accuracy. The most recent four extractions use also LHC data on Z-boson production.

The best known leading-twist TMD PDF is the unpolarized $f_1(x, k_T^2)$. In Fig. 22, we list the most recent extractions of f_1 from data on SIDIS unintegrated multiplicities and/or cross sections for the production of Drell-Yan lepton pairs or Z-boson. The "Pavia 2013" is the first (and unique, so far) analysis with an explicit flavor dependence in the fitting parameters of the functional form [228]. The impact of this non-perturbative effect on the extraction of the W-boson mass m_W at LHC has been explored using the template-fit technique, reaching the conclusion that the uncertainty Δm_W induced by flavor sensitivity in quark k_T distributions might be comparable with the error correlated to PDF uncertainties [229]. The "Pavia 2017" is the first extraction from a global fit of 8059 points from SIDIS, Drell-Yan, and Z-boson data [9], reaching a $\chi^2/\text{d.o.f.} = 1.55 \pm 0.05$ with only 11 parameters. The main drawbacks of this analysis were the still marked anti-correlation between TMD PDF and TMD FF k_T distributions (calling for an independent extraction of TMD FFs from e^+e^- data, which is still missing), and difficulties in reproducing the normalization of low-Q^2 SIDIS data (a similar finding is reported in other later works [230, 231]). Very recently, a series of new analyses have been published where the details of perturbative resummation match the same accuracy of standard phenomenology at the LHC. In "BSV 2019" [232] and "Pavia 2019" [220] the data set encompasses measurements from only Drell-Yan and Z-boson production including very precise ATLAS data points, implementing kinematical cuts on the final leptons and without *ad-hoc* adjusting the normalization [220]. The "SV 2019" includes also SIDIS data [221] although the total number of fitted points is still far from the "Pavia 2017" record. In all these cases, a large impact of LHC data was found on the behavior of the resulting $f_1(x, k_T^2)$ at small x. The general outcome of results listed in Fig. 22 can be summarized in the tomography depicted in Fig. 23, which shows the x-dependence of the k_T-distribution of quarks inside Nucleons at $Q^2 = 1$ GeV^2. Through TMD evolution, we know also how this tomography evolves to higher scales and from "Pavia 2013" we have some limited information on its flavor dependence [228]. Nothing is known about the gluon TMD PDF. Several studies explored useful channels at RHIC or LHC with $p-p$ collisions leading to $J/\psi + X$, or $J/\psi + \gamma + X$, or $\eta_c + X$ [233–236]. At the EIC, it would be possible to consider also SIDIS processes like $e-p$ collisions leading to $J/\psi+X$, h_1+h_2+X, jet + jet + X, J/ψ + jet + X [234, 237–239].

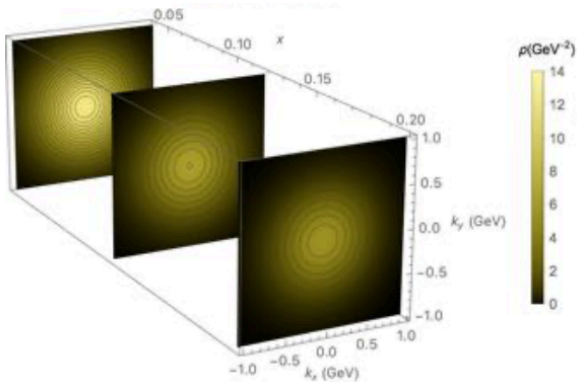

FIG. 23. Tomography of unpolarized $f_1(x, k_T^2)$ of quarks in the proton at $Q^2 = 1$ GeV^2 [9].

In Fig. 21, another key entry in the table is the so-called Sivers function $f_{1T}^{\perp}$ appearing in the bottom left

corner. It describes how the k_T distribution of an unpolarized quark is distorted in a transversely polarized Nucleon [240]. Evidently, the $f_{1T}^{\perp}$ describes a spin-orbit effect at the partonic level. The Sivers function is representative of the class of naïve T-odd TMDs, namely of those TMDs that are not constrained by T-reversal invariance [215]. Their universality is broken but in a calculable way. For example, the Sivers function extracted in a Drell-Yan process with a transversely polarized proton should turn out opposite to the one that is extracted in SIDIS. The $f_{1T}^{\perp}|_{\rm DY} = -f_{1T}^{\perp}|_{\rm SIDIS}$ prediction is based on very general assumptions, and it represents a fundamental test of QCD in the non-perturbative regime [241]. Therefore, it is subject of intense experimental investigation. Preliminary results hint to statistically favor the prediction [242–244] although more precise data are needed to draw a sharp conclusion. Many parameterizations of the Sivers function are available on the market (for example, see Refs. [245–251]). In Fig. 24, the first k_T-moment multiplied by x, *i.e.* $xf_{1T}^{\perp(1)}(x)$, is shown as a function of x for the up and down quarks. Results from recent parameterizations ("PV11" [247], "EIKV" [252], "TC" [253], "PV19" [254]) agree within statistical uncertainty. Figure 25 supplements the tomography of Fig. 23: the upper panels correspond to the unpolarized k_T distribution of that figure at $x = 0.1$; the lower panels visualize how those k_T distributions get distorted by the Sivers effect in an opposite way for up and down quarks. Both groups of panels show quark probability densities that are entirely based on real experimental data for Nucleons with or without transverse polarization.

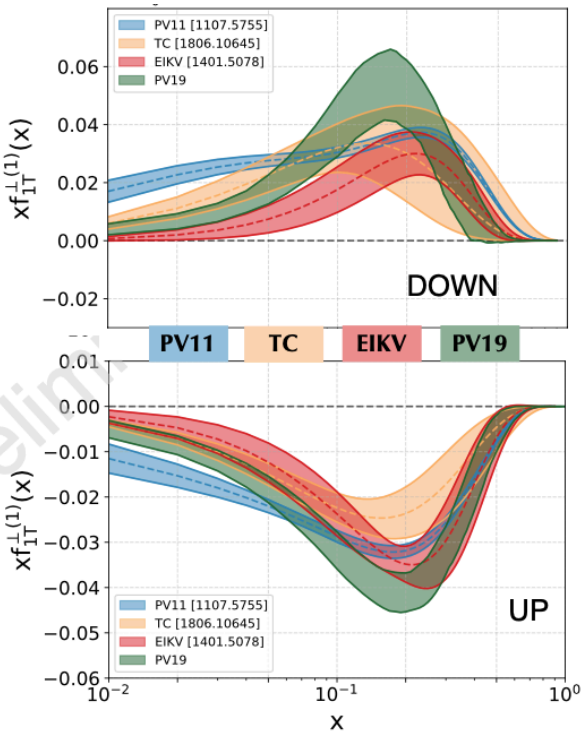

FIG. 24. The $xf_{1T}^{\perp(1)}(x)$ (first k_T-moment of the Sivers function multiplied by x) as a function of x. Upper panel for down quark, lower for up quark. Parameterizations: "PV11" at $Q^2 = 1$ GeV^2 from Ref. [247]; "EIKV" at $Q^2 = 2.4$ GeV^2 from Ref. [252]; "TC" at $Q^2 = 1.2$ GeV^2 from Ref. [253]; "PV19" at $Q^2 = 1$ GeV^2 from Ref. [254].

The precision of the current knowledge will be significantly improved with the planned measurements at Jefferson Lab after the recent 12 GeV energy upgrade (JLab12) and with planned future EIC. The SoLID SIDIS experiments [255–257] with JLab12 will provide the most precise measurements [130] of Sivers asymmetries in the valence quark region ($x > 0.05$). Figure 26 shows the projected uncertainty bands of extracted Sivers function for up and down quarks with SoLID data comparing with the ones with current world data. Also shown at the bottom panel of the figure are the improvements (ratios of world data uncertainty over SoLID uncertainty). Figure 27 shows the 2D projection (x and $k_\perp$) of the extracted Sivers function from SoLID measurements compared with that extracted from the current world data.

The right-most column of the table in Fig. 21 contains the chiral-odd TMD PDFs, which are related to processes not conserving quark helicity. Each of them can appear in the cross section if it is associated to a chiral-odd partner [258]. The best known chiral-odd TMD PDFs is the transversity h_1. It describes the correlation between the transverse polarizations of the nucleon and of its constituent quarks. Transversity survives in collinear framework: it is the third PDF needed to fully account for the partonic spin structure of the Nucleon at leading twist. The TMD PDF $h_1(x, k_T^2)$ can be extracted from SIDIS data for the so-called Collins effect [259–261] (the chiral-odd partner being the Collins function $H_1^{\perp}$, simultaneously extracted from e^+e^- asymmetry data). As previously mentioned, the limitation of the TMD framework prevents this analysis to be extended to a global fit including data on the Collins effect in hadron-hadron collisions. This limitation can be overcome by considering the Collins effect for a hadron detected inside a jet [262], where the TMD FF $H_1^{\perp}$ is paired to the collinear PDF $h_1(x)$ [263]. Alternatively, in a fully collinear framework the PDF $h_1(x)$ can be extracted from data on the inclusive production of di-hadrons inside the same current jet and with small invariant mass [264–268] (the chiral-odd partner being now the di-hadron function $H_1^{\sphericalangle}$, that can be extracted from asymmetry data on di-hadron pair production in e^+e^- [269–272]). Because of the collinear framework, $h_1(x)$ could be extracted not only from SIDIS data [273–275] but also from a global fit including data on proton-proton collisions [276]. In Fig. 28, the results for $xh_1(x)$ and for valence up (upper panel) and down (lower panel) quarks extracted from Refs. [259, 260, 276] are compared at the same scale $Q^2 = 2.4$ GeV^2, showing a reasonable agreement.

The planned measurements at JLab12 will greatly improve our knowledge of transversity. The SoLID SIDIS experiments [255–257] with JLab12 will provide the most precise measurements of Collins asymmetries [277] in the

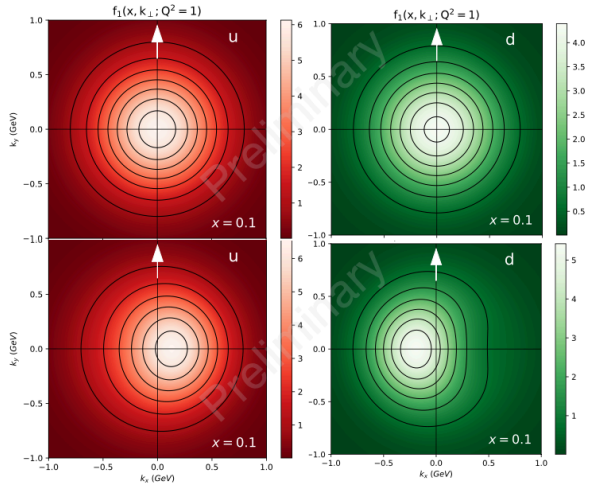

FIG. 25. Upper panel: tomography of unpolarized $f_1(x = 0.1, k_T^2)$ at $Q^2 = 1$ GeV^2 as in Fig. 23. Lower panel: tomography of Sivers effect in same kinematic conditions from "PV19" parameterization [254]. Left panel for up quark, right panel for down quark.

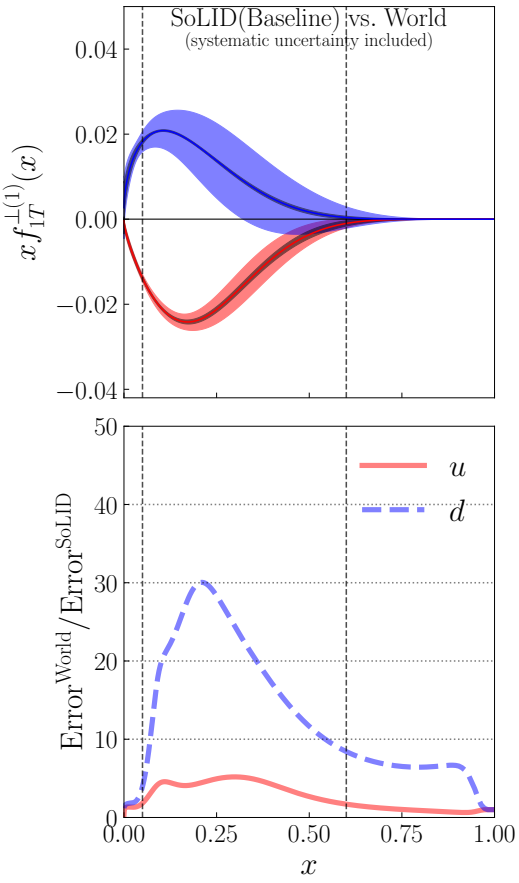

FIG. 26. Upper panel: projections of uncertainty band of the Sivers function for up (red bands) and down (blue bands) quarks extracted from SoLID measurements (darker bands) comparing with those extracted from current world data (lighter bands) at $Q^2 = 2.4$ GeV^2. Lower panel: ratios of uncertainty for current world data over that for SoLID for up (red curve) and down (blue curve) quarks.

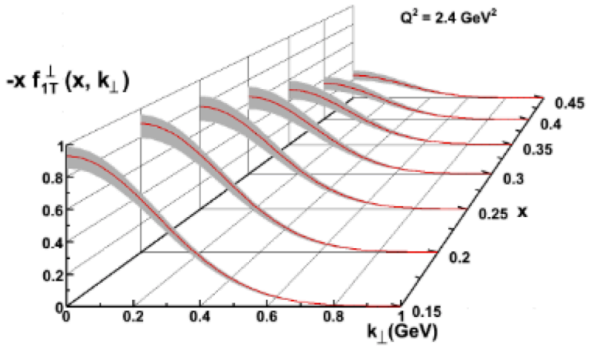

FIG. 27. Sivers function of x and $k_\perp$ for up quark at $Q^2 = 2.4$ GeV^2. Red band: uncertainty band for projection extracted from SoLID measurements. Gray band: uncertainty band extracted from current world data.

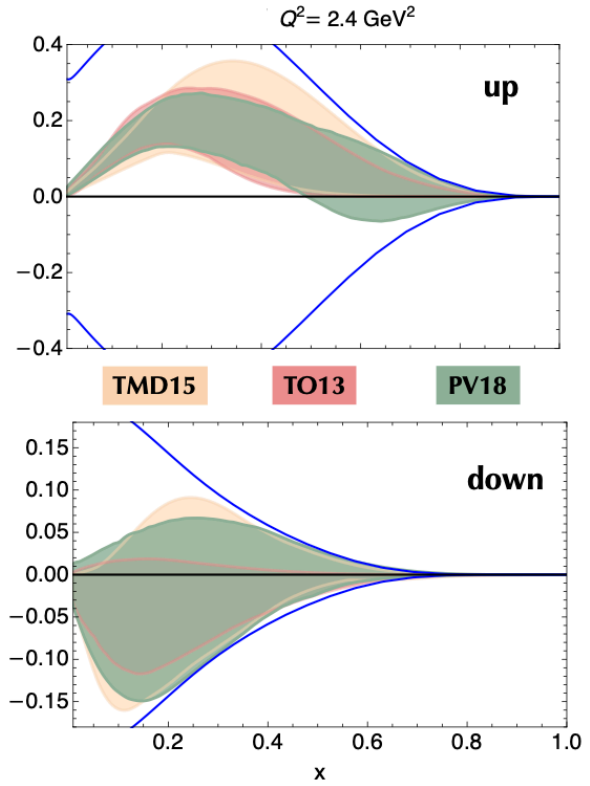

FIG. 28. The $xh_1(x)$ at $Q^2 = 2.4$ GeV^2 for valence up quark (upper panel) and down quark (lower panel). Yellow band "TMD15" from Ref. [260]; red band "TO13" from Ref. [259]; green band "PV18" from Ref. [276]. Blue solid lines for the Soffer bound at the same scale.

valence quark region ($x > 0.05$). Figure 29 shows the projected uncertainty bands of extracted transversity for up and down quarks with SoLID data comparing with the ones with current world data. Also shown in the bottom panel of the figure are the improvements (ratios of world data uncertainty over SoLID uncertainty). In Fig. 30, the global fit of Ref. [276] and the Collins extraction of Ref. [261] are compared at $Q^2 = 4$ GeV^2 with a lattice calculation of the corresponding quasi-

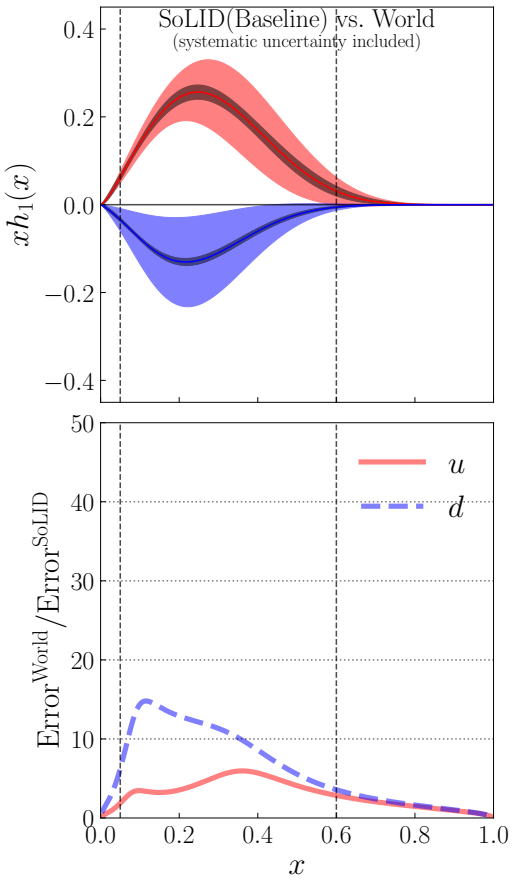

FIG. 29. Same as in Fig. 26 but for the transversity distribution.

PDF [140]. The first Mellin moment of $h_1(x)$ is named tensor charge g_T and has recently received increasing attention in searches of new physics Beyond Standard Model (BSM). For example, the tensor charge affects the contribution of quark electric dipole moments to the neutron electric dipole moment in searches of BSM sources of CP-violation [278, 279]. In Fig. 31, the results for g_T^u and g_T^d from various phenomenological extractions of transversity are shown with black points and compared with recent lattice computations (shown with blue points). The red point shows the impact of JLab12 SoLID projection on the (SIDIS $+e^+e^-$) analysis of the Collins effect [277]. This would translate in an improvement of a factor 2 on the current limit of the up electric dipole moment [280].

Each TMD PDF in Fig. 21 enters the SIDIS cross section with a specific dependence on azimuthal angles defined by the kinematics of the process. Hence, it can be extracted through measurements of azimuthal (spin) asymmetries. All relevant asymmetries corresponding to the entries in Fig. 21 have been explored [281–288] and will be precisely measured [255–257, 289], providing crucial information on spin-orbit correlations and the orbital angular momentum of the confined quarks inside the Nucleon.

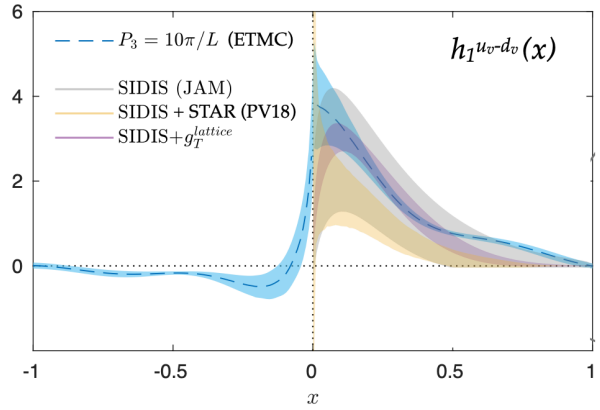

FIG. 30. The isovector component of $h_1(x)$ at $Q^2 = 4$ GeV^2. Blue band "ETMC" from lattice calculation of Ref. [140]. Gray band "JAM" from extraction based on SIDIS data of Ref. [261], purple band when including constraint of reproducing lattice isovector tensor charge $g_T^{lattice}$. Yellow band "PV18" from global fit of Ref. [276].

In summary, studies of 3D maps of the partonic structure of Nucleons in momentum space are moving from an exploratory phase to the era of precision. Links to high-energy phenomenology are being established and inputs from non-perturbative effects encoded in TMDs could affect those analyses. Upcoming data from starting projects like JLab12 (in particular, the expected high precision data from SoLID) and future projects (LHCspin, ALICE, EIC) will significantly enlarge the available phase space, and will contribute in deepening our knowledge of parton dynamics, ultimately clarifying the mechanisms leading to confinement.

F. Mapping the Energy-Momentum Tensor of Ground State Nucleons from DVCS Data

The experimental study of the proton energy-momentum tensor is a novel tool to obtain information about the mechanical or gravitational properties of particles. Russian theorists I. Yu. Kobzarev and L.B. Okun [295], and American theorist Heinz Pagels [296] were the first ones to explore, independently, the possibility of studying the mechanical properties of subatomic particles. Pagels developed the framework of gravitational form factors in analogy to the electromagnetic interaction. However, he concluded that *contrary to the case of electromagnetism, there is very little hope of learning anything about the detailed mechanical structure of a particle, because of the extreme weakness of the gravitational interaction.* The field remained dormant and was revived only with the discovery of the GPDs [297–299] and the relationship of their second Mellin moments to $J(t)$, $M2(t)$, and $d1(t)$, which are the gravitational form factors (GFF) of the proton matrix element of the energy-momentum tensor. They relate to the distribution of angular momentum, the mass and energy, and the radial

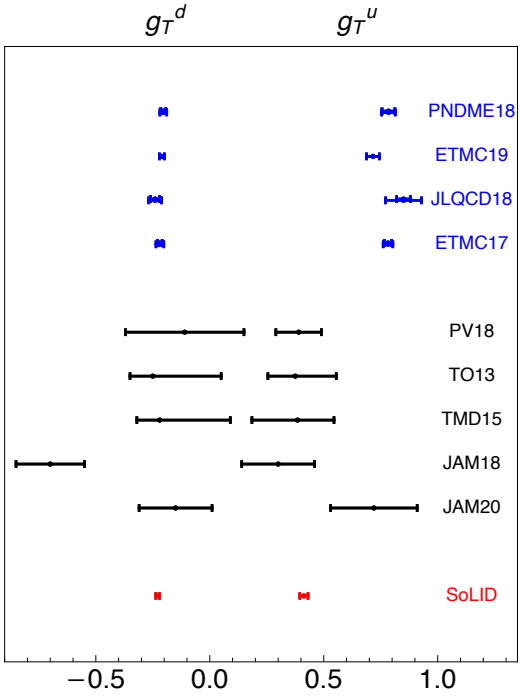

FIG. 31. The tensor charge g_T for down (left) and up quark (right). Blue points from lattice calculations ("PNDME18" [290], "ETMC19" [291], "JLQCD18" [292], "ETMC17" [293]). Black points from phenomenological extractions of transversity ("PV18" [276], "TO13" [259], "TMD15" [260], "JAM18" [261], "JAM20" [294]). Red point from SoLID projection on "TMD15" results [277].

distribution of shear forces and pressure inside the proton [300]. The first experimental application came in 2017 with the extraction of the GFF $d1(t)$, shown in Fig. 32, employing the two sets of DVCS data published by the CLAS Collaboration [177, 178], and the subsequent estimate of the pressure distribution inside the proton [11], which yielded a peak pressure near the proton center of 10^{35} Pa, exceeding the gravitational pressure observed in neutron stars LIGO by an order of magnitude.

The first extraction of the pressure distribution inside the proton has already generated over 70 citations, and inspired many theoretical papers that, among others, relate the pressure distribution to limits on deviations from general relativity at short distance [301], applications to computing the equation of state in neutron stars [302], Lattice calculations of gluon contributions to the pressure distribution [303], studies of a two-scale structure of the proton related to LHC results [304–307], computations of the proton mechanical radius [308, 309], a detailed review paper [310], extensions of the concept of mechanical properties [311] and others.

In the near future, given a sufficient amount of DVCS data, including polarized beam asymmetries and cross section data, covering a large range in photon virtuality Q^2, and in four-momentum transfer t to the proton, the

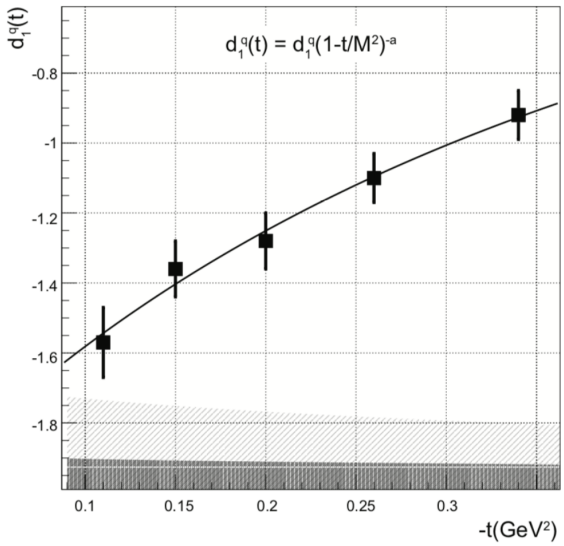

FIG. 32. Example of a fit to $d_1(t)$. The error bars are from the fit to the cross sections at fixed value of $-t$ and correspond to 1 standard Gaussian deviation. The single-shaded area at the bottom corresponds to the uncertainties from the extension of the fit into regions without data and is reflected in the green shaded area in Fig. 33. The double-shaded area corresponds with the projected uncertainties from future experiment as shown in Fig. 33 with the red shaded area.

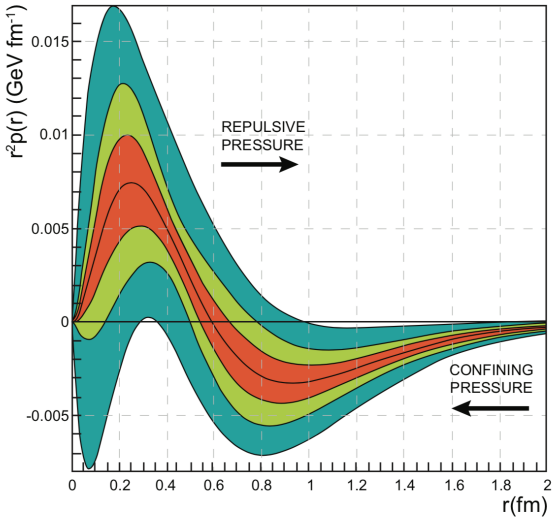

FIG. 33. The radial pressure distribution in the proton. The figure shows the pressure distribution $r^2p(r)$ resulting from the interactions of the quarks in the proton versus the radial distance from the center in fm. The black central line corresponds to the pressure extracted from the D-term parameters fitted to the published data at 6 GeV [177, 178]. The corresponding estimated uncertainties are displayed as the shaded area shown in light green. They correspond to 1 standard deviation. See the text for more details.

large systematic uncertainties of these first data (green band) can be significantly reduced. The DVCS program at the JLab 12 GeV upgrade is now generating the data that can result in significant advances of the field.

A significant extension of the JLab experimental program at 12 GeV that employs both electron and positron beams will directly access the real part of the Compton amplitude. This will allow for a much improved isolation of the Compton FF $\mathcal{H}(\xi,t)$ with much smaller systematic uncertainties. Estimates (see the proceedings of Positron workshop [312, 313]) have shown that the beam charge asymmetries are large and can directly access the real part of the Compton amplitude, which would be a major advance in the program to establish the 3D quark imaging of nucleons, and to determine one of the gravitational form factors, $d_1(t)$, in a larger t range.

G. Insights into Strong QCD from Combined Studies of Baryon Ground and Excited States

Contemporary strong interaction theory is beginning to reveal many consequences of EHM, as illustrated by Figs. 7 to 9. Numerous calculations connect these features with observable properties of hadron ground states and the associated comparisons with experiment show that the ideas are viable. However, the ground state is just one isolated member of a set of Hamiltonian eigenvectors with infinitely many elements: many Hamiltonians can possess practically identical ground states and yet produce excited-state spectra that are vastly different. Moreover, masses alone, being infrared-dominated quantities, contain relatively little information. Distinct Hamiltonians can satisfactorily reproduce known hadron spectra; but these same Hamiltonians deliver predictions that disagree enormously when employed to compute structural properties. Such properties – like the Q^2-dependence of elastic and transition form factors – possess the greatest discriminating power. Hence, modern theory must be deployed to compute these observables. With CSMs, their reliable prediction requires the use of realistic wave functions and currents, the calculation of which is challenging; and using LQCD, algorithmic and technical challenges must be surmounted in order to deliver simulations of realistic systems.

These remarks mean that results on the structure of nucleon resonances cannot be divorced from those obtained for ground-state nucleons and mesons. In order to validate any description of features of the latter, one must elucidate the properties of all systems that can be produced by the theoretical framework and insist that the approach provide a unifying explanation. This is true for all sectors: mesons, baryons, hybrids and exotics. Consequently, any claim that progress has been made toward understanding QCD should be tested by the requirement that its basis provides a simultaneous explanation of, *inter alia*: how emergent mass is expressed in distinct bound states; and if there are differences between systems, then how can they be understood?

Concerning baryons, an important aspect of EHM is expressed in the fact that any interaction capable of creating pseudo–Nambu-Goldstone modes as bound-states of a light dressed-quark and -antiquark, and reproducing the measured value of their leptonic decay constants, will necessarily, *inter alia*, also generate strong color-antitriplet correlations between any two dressed-quarks contained within a nucleon [314].

The properties of such diquark correlations are known. As color-carrying correlations, diquarks are confined [315, 316]. Additionally, a diquark with spin-parity J^P may be viewed as a partner to the analogous J^{-P} meson [317]. Hence, the strongest diquark correlations in the nucleon are: scalar isospin-zero, $[ud]_{0^+}$; and pseudovector, isospin-one, $\{uu\}_{1^+}$, $\{ud\}_{1^+}$, $\{dd\}_{1^+}$. Moreover, while no pole-mass exists, the following mass-scales, which express the strength and range of the correlation, may be associated with these diquarks [20, 145, 317–324] (in GeV):

$$m_{[ud]_{0^+}} \approx 0.7 - 0.8\,,\; m_{\{uu\}_{1^+}} \approx 0.9 - 1.1\,. \qquad (2)$$

With isospin symmetry, $m_{\{dd\}_{1^+}} = m_{\{ud\}_{1^+}} = m_{\{uu\}_{1^+}}$.

It should be stressed that contemporary applications of CSMs indicate that the ground-state nucleon necessarily contains both scalar-isoscalar and pseudovector-isovector correlations: neither can be ignored and their presence has many observable consequences [145, 147, 324–328]. On the other hand, further amplifying the importance of excited states, odd-parity baryons are predicted to contain pseudoscalar and vector diquarks and these correlations might also play a role in even-parity excited states of the nucleon [320–322]. Importantly, there is also strong evidence for the presence of diquark correlations in baryons from LQCD [329–332].

Realistic diquark correlations are soft and interacting. All carry charge, scatter electrons, and possess an electromagnetic size that is similar to that of the analogous mesonic system, *e.g.* [319, 333, 334]:

$$r_{[ud]_{0^+}} \gtrsim r_\pi, \quad r_{\{uu\}_{1^+}} \gtrsim r_\rho, \qquad (3)$$

with $r_{\{uu\}_{1^+}} > r_{[ud]_{0^+}}$. As in the meson sector, these scales are set by that associated with EHM.

Here it should be emphasized that these fully dynamical diquark correlations are vastly different from the static, point-like "diquarks" introduced originally [335] in an attempt to solve the so-called missing resonance problem [336], *viz.* the fact that quark models predict many more baryon states than were observed in the previous millennium [337]. Moreover, their existence enforces certain distinct interaction patterns for the singly and doubly represented valence-quarks within the proton and its excited states, as exhibited elsewhere [16, 146, 147, 325].

The existence of such tight correlations between two dressed quarks is the key to transforming the three valence-quark scattering problem into a simpler Faddeev

equation [338–340]; and this is achieved without loss of dynamical information [341]. The three-gluon vertex, a signature feature of QCD's non-Abelian character, is not explicitly part of the bound-state kernel in this picture. Instead, one capitalizes on the feature that phase-space factors materially enhance two-body interactions over $n \geq 3$-body interactions and exploits the dominant role played by diquark correlations in the two-body subsystems. Then, while an explicit three-body term might affect fine details of baryon structure, the dominant effect of non-Abelian multi-gluon vertices is expressed in the formation of diquark correlations. Consequently, as depicted in Fig. 34, the active kernel describes binding within the baryon through diquark breakup and reformation, which is mediated by exchange of a dressed-quark. Such a baryon is a compound system whose properties and interactions are largely determined by its quark+diquark structure.

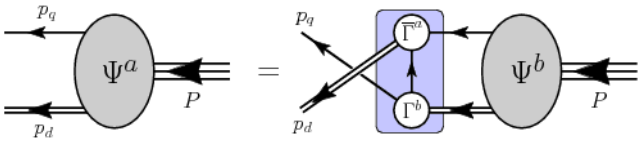

FIG. 34. Poincaré covariant Faddeev equation: a linear integral equation for the matrix-valued function Ψ, being the Faddeev amplitude for a baryon of total momentum $P = p_q + p_d$, which expresses the relative momentum correlation between the dressed-quarks and -diquarks within the baryon. The shaded rectangle demarcates the kernel of the Faddeev equation: *single line*, dressed-quark propagator; Γ, diquark correlation amplitude; and *double line*, diquark propagator.

Importantly, the number of states in the spectrum of baryons obtained from the Faddeev equation [320, 321, 323, 324] is similar to that found in the three-constituent quark model. This prediction is consistent with direct solutions of the Poincaré-covariant three-body bound-state equation [320, 342] and LQCD results [343]; and, notably, modern data and recent analyses have already reduced the number of missing resonances [14, 344–348].

Furthermore, it is beginning to appear that diquark correlations also play a role in baryons involving one or more heavy quarks. In these systems, owing to the dynamical character of the diquarks, it is typically the lightest allowed diquark correlation that defines the most important component of a baryon's Faddeev amplitude [324]. This outcome challenges the validity of phenomenological models that treat singly heavy baryons ($qq'Q, q, q' \in \{u, d, s\}, Q \in \{c, b\}$) as two-body light-diquark+heavy-quark ($qq' + Q$) bound states; similarly, those that treat doubly heavy baryons (qQQ' as two-body light-quark+heavy-diquark bound-states, $q + QQ'$.

The increasing evidence in support of a role for two-body correlations in baryons has spurred analyses that seek to exploit diquarks in tetra- and pentaquark systems [349, 350] and others that search for different correlations in hybrid systems [351]. The latter are sensitive to hitherto unexplored aspects of gluon-quark dynamics [352].

Having explained the origin and sketched the features of diquark correlations, it is natural now to return to the central topic of this subsection with a simple observation: QCD is not solved unless the Roper resonance is understood. In this connection, the last twenty years have seen the acquisition and analysis of a vast amount of high-precision proton-target exclusive electroproduction data with single- and double-pion final states on a large kinematic domain of energy and momentum-transfer; development of a sophisticated dynamical reaction theory capable of simultaneously describing all partial waves extracted from available, reliable data; and formulation and wide-ranging application of CSMs. Following these efforts, it is now widely accepted that the Roper is, at heart, the first radial excitation of the nucleon, consisting of a well-defined dressed-quark core that is augmented by a meson cloud, which both reduces the Roper's core mass by approximately 20% and contributes materially to the electroproduction transition form factors on $Q^2 \lesssim 2m_N^2$ (m_N is the nucleon mass) [2].

The $\Delta(1232)$ also has a radial excitation and one should answer the question: "Is this the $\Delta(1600)$?" This is because the spectrum of Δ-baryons exhibits the same level-inversion seen in the nucleon spectrum, *viz.* the lightest negative-parity state is heavier than the two lightest positive-parity states. The Roper experience has demonstrated that it will only become possible to decide the character of the $\Delta(1600)$ after one has predictions for the associated electroproduction form factors and experiments to test them. Fortunately, data exist [353, 354] and can be analyzed with this aim understood; and theoretical predictions are now available [145].

Recall that Poincaré covariance demands that the proton possess intrinsic deformation. However, quantum mechanics teaches that such deformation is not observable for $J = 1/2$ systems. On the other hand, deformation can be observed in proton $= p \to \Delta(1232)$, $\Delta(1600)$ transitions.

Regarding $\gamma^* p \to \Delta(1232)$, on $Q^2 \gtrsim 0.5 m_N^2$, *i.e.* outside the meson cloud domain for this process, the magnetic dipole and Coulomb quadrupole form factors reported in Ref. [145] agree well with available data. Consistent with the data, too, the electric quadrupole form factor is very small in magnitude; hence, it is particularly sensitive to the diquark content and quark+diquark angular-momentum structure of the baryons involved, and also to meson-baryon final-state-interactions (MB FSIs) on a larger domain than the other form factors. These remarks are supported by the following observations: the role played by higher partial waves in the wave functions increases with momentum transfer (something also observed in meson form factors), here generating destructive interference; agreement with data on G_M^* is impossible without the higher partial waves; and the effect of such components is very large in G_E^*, with the complete result for G_E^* exhibiting a zero at $Q^2 \approx 4m_N^2$, which is absent in the S-wave-only result(s).

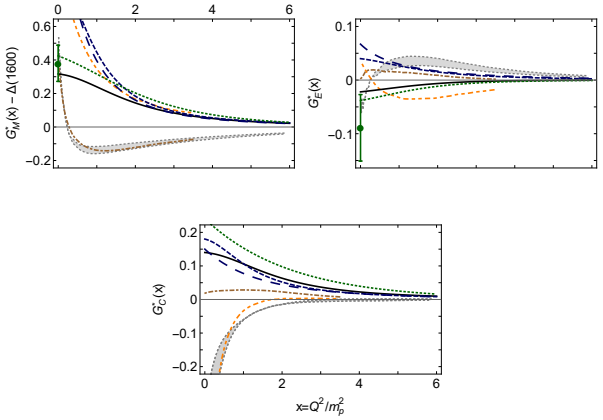

FIG. 35. UL: Magnetic dipole $\gamma^* p \to \Delta(1600)$ form factor; UR: electric quadrupole; and Bottom: Coulomb quadrupole. Data from Ref. [1]; and the conventions of Ref. [355] are employed. All panels: solid [black] curve, complete result; long-dashed [blue] curve, result obtained when $\Delta(1600)$ is reduced to S-wave state; dashed [blue] curve, both the proton and $\Delta(1600)$ are reduced to S-wave states; dotted [green] curve, obtained by enhancing proton's axial-vector diquark content; shaded [gray] band, light-front relativistic Hamiltonian dynamics (LFRHD) [356]; dot-dashed [brown] curve, light-front relativistic quark model (LF-RQM) with unmixed wave functions [357]; and dot-dot-dashed [orange] curve, LF-RQM with configuration mixing [358].

Drawn from Ref. [145], predictions for the $\gamma^* p \to \Delta(1600)$ transition form factors are displayed in Fig. 35. Here, empirical results are only available at the real-photon point: $G_M^*(Q^2 = 0)$, $G_E^*(Q^2 = 0)$. Evidently, the quark model results – [shaded gray band] [356], dot-dashed (brown) curve [357], and dot-dot-dashed [orange] curve [358]) – are very sensitive to the wave functions employed for the initial and final states. Furthermore, inclusion of relativistic effects has a sizeable impact on transitions to positive-parity excited states [356].

The quark+diquark Faddeev equation prediction is the solid [black] curve in each panel of Fig. 35. In this instance, every transition form factor is of unique sign on the domain displayed. Notably, the mismatches with the empirical results for $G_M^*(0)$, $G_E^*(0)$ are commensurate in relative sizes with those in the $\Delta(1232)$ case, suggesting that MB FSIs are of similar importance in both channels.

Axial-vector diquark contributions interfere constructively with MB FSIs [359]; hence, regarding form factors, one can mimic some meson cloud effects by modifying the axial-vector diquark content of the participating hadrons. Accordingly, to illustrate the potential impact of MB FSIs, the transition form factors were also computed using an enhanced axial-vector diquark content in the proton. This was achieved by setting $m_{1^+} = m_{0^+} = 0.85$ GeV, values with which the proton's mass is practically unchanged. The procedure produced the dotted [green] curves in Fig. 35; better aligning the $x \simeq 0$ results with experiment and suggesting thereby that meson-cloud effects will improve the Faddeev equation predictions.

The short-dashed [blue] curve in Fig. 35 is the result obtained when only rest-frame S-wave components are retained in the wave functions of the proton and $\Delta(1600)$; and the long-dashed [blue] curve is that computed with a complete proton wave function and a S-wave-projected $\Delta(1600)$. Once again, the higher partial-waves have a visible impact on all form factors, with G_E^* being most affected: the higher waves produce a change in sign. This reemphasizes one of the conclusions from the quark model studies, *viz.* data on the $\gamma^* p \to \Delta(1600)$ transition form factors will be sensitive to the structure of the $\Delta(1600)$.

These observations emphasize that it is crucial to study the complete spectrum of states and expose the internal structure of characterizing members of each level if one wishes to arrive at answers to numerous fundamental questions in hadron physics. For instance, is relativity important to hadron structure; and if so, when is it expressed, how, and what can be learned from seemingly good predictions made with nonrelativistic models? Furthermore, are there two-body subclusters (correlations) in baryons and other hadrons; if so, what sort of correlations, in which channels, how are they manifested in observables, and what do they reveal about EHM? In answering such questions, tools will be developed that are necessary to chart the distributions of energy, momentum and mass within QCD bound states, and learn how they are influenced by the hadronic and nuclear environments.

H. Exploring the Emergence of Nuclear Structure from Strong QCD

Systematic studies of monopole, quadrupole, and rotational collective modes in atomic nuclei suggest that approximate symmetries play an important, if not dominant role in determining their low-energy structure. Indeed, to leading order - at least for light nuclei - it has been shown that calculated eigenstates using realistic NN interactions correlate strongly with eigenvectors of the symplectic [Sp(3,R)] group [12, 360, 361].

From a microscopic perspective the latter should not come as a surprise as the 21 generators of Sp(3,R) consist of the particle-symmetric independent quadratic forms in the momenta and spatial coordinates of the constituent particles. These in turn can be re-grouped into four physically important subset modalities: six generators of monopole and quadrupole moments, six generators of monopole and quadrupole deformation, three generators of rotation, and another set of six generators associated with quadrupole flow. For purposes of this contribution, which is to probe the linkage between low-energy nuclear physics (as seemingly governed by the strong interaction between nucleons and mesons), and high-energy nuclear physics (as governed by the strong interaction between quarks and gluons), it is important to realize that Sp(3,R) can also be characterized as a multi-shell gen-

eralization of the single-shell Elliott SU(3) model. The Elliott SU(3) symmetry enters as a subgroup of Sp(3,R) in a chain that ends with SO(3), the symmetry group of the orbital angular momentum. Specifically, if one removes from Sp(3,R) the generators of U(3) - all of which act only within single major shells of the oscillator (for SU(3) plus 1 for U(1) that counts the total number of oscillator quanta within a shell), the remaining 12 generators are 6 raising operators each of which adds two quanta to a configuration [a L=0 (monopole, or 's') mode, and another five L=2 (quadrupole, or 'd') modes, with the other 6 lowering operators that are simply conjugates of the raising operators].

The latter features, when understood within the context of a many-particle shell-model theory that takes into account Pauli statistics between like particles, provides a linkage to the more common Slater determinant characterization of shell-model basis states, as well as our ability to understand the microscopic *np-nh* structures [12, 361] that are also everywhere apparent as clustering degrees of freedom in atomic nuclei. The good news is that within the past few years a so-called symmetry-adapted no-core shell-model (SA-NCSM) code [362] has been developed that takes all of these features into account, including the ability to start from realistic interactions that are considered to be part of what is now commonly referred to as *ab initio* shell-model theories.

As the above implies, the Sp(3,R) model can also be used to expose the microscopic underpinnings of clustering in nuclei; especially, but not only, when the total number of nucleons is a simple multiple of the α-particle, which is the case for the α-particle (^{4}He) itself, ^{8}Be, ^{12}C, ^{16}O, ^{24}Mg, and so on. In particular, in contrast with the simplest of α-cluster models, the reach-back to *ab initio* features in nuclei afforded by the Sp(3,R) model suggests that the Hoyle state in ^{12}C is considerably more subtle than simply geometrical configurations of three α particles suggest. Indeed, SA-NCSM calculations have demonstrated the relevance of Sp(3,R) for light p-shell nuclei through the sd-shell and even into the intermediate mass region of the pf shell. Beyond this, additional considerations are needed due to a breaking of this simple picture as evidenced in a growing of neutron excesses over the proton count. But even for strongly deformed nuclei of the rare earth and actinide regions [12], the prominence of deformation and clustering is everywhere apparent, especially in fission fragments. In short, nuclear deformation and shape coexistence dominate the entire nuclear landscape. However, while advanced tools of the SA-NCSM type await further developments for heavy nuclei, for the current focus of examining the bridging between nuclear structure and strong QCD, a focus on light nuclei is best; and for this, the existing SA-NCSM should suffice.

Before pushing ahead with addressing low/high energy aspects of the nuclei/nucleon interface, it seems useful to also recall that the simplest Bohr-Mottelson liquid-drop picture of a nucleus – which predated the work of Elliott – was used to successfully describe in the simplest of terms the dominance of rotational and vibrational modes in light as well as heavy nuclei. Under the assumption of deformation (quadrupole) dominance described in terms of two shape variables, β and γ, many observed features of nuclei – light and heavy – could be reasonably reproduced. Interestingly, the corresponding quantities in the Sp(3,R) picture are the (λ, μ) representation labels of the lowest-weight SU(3) configuration in a Sp(3,R) representation that uniquely defines its entire structure. In fact, up to an overall scaling, the rotational invariants of SU(3) can be put in one-to-one correspondence with β and γ of the Bohr-Mottelson theory. In short, β is a radial measure of the prolate-oblate character of a nucleus and γ is an angular measure of its triaxiality. This relationship is depicted schematically in Fig. 36 (bottom) where the

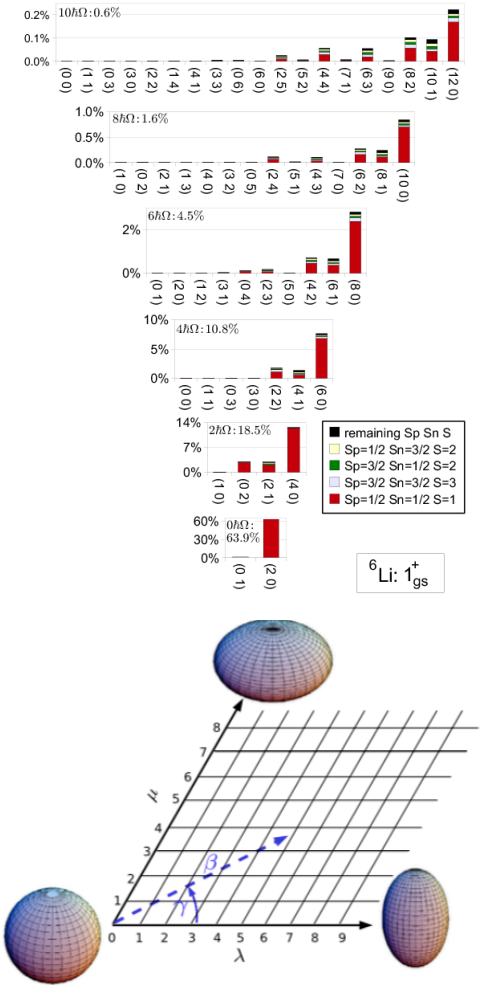

FIG. 36. (Top) The symplectic configurations in the wave function of the ground state of ^{6}Li computed within the SA-NCSM [362]. Less than 1% of the included configurations account for greater than 90% of the physics encoded in the wave function. (Bottom) The correspondence between the Elliott SU(3) group quantum numbers (λ, μ) and the parameters β and γ that describe the shape of atomic nuclei.

continuous β and γ values are shown by a vector, while the discrete (λ, μ) quantum numbers of the Elliott SU(3) group are depicted by a mesh overlaying the same space. Each node corresponds to a certain shape (spherical, prolate, oblate, or triaxial) as determined by the β and γ parameters of each node. In summary, the basis states of a specific Sp(3,R) symmetry should be considered to be a coherent combination of the well-defined shapes.

The above background on symmetry informed advances in *ab initio* approaches for studying the structure of atomic nuclei [12], coupled with progress in gaining a description of the ground state structure of nucleons from a strong QCD perspective within continuum QCD approaches [48, 145, 146, 314, 323] discussed below, opens up a promising new avenue to explore at a deeper level how deformation of atomic nuclei emerges from strong QCD. These studies address two important questions: (*a*) whether the ground state of a nucleon in its intrinsic frame is round or deformed, and (*b*) how the interactions between nucleons within nuclei are driven by strong QCD and the role it plays in the generation of dynamic deformation found in atomic nuclei? Clearly the scales are different – MeV for nuclei and GeV for the strong interaction between the dressed quarks and gluons in the strong QCD regime; yet, the deuteron is bound and deformed while di-neutrons and di-protons are unbound, and the α-particle (^{4}He) is the most tightly bound of all light nuclei, and also deformed!

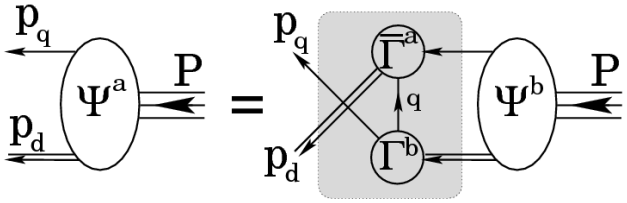

FIG. 37. Nucleon = quark+diquark Faddeev equation. This is a linear integral equation for the Poincaré-covariant matrix-valued function Ψ, the Faddeev amplitude for a state with total momentum $P = p_q + p_d$. It describes the relative momentum correlation between the dressed-quarks and -diquarks. Legend. Shaded rectangle – kernel of the Faddeev equation; *single line* – dressed-quark propagator; Γ – diquark correlation amplitude; and *double line* – diquark propagator. Ground-state nucleons (n - neutron, p - proton) contain both isoscalar-scalar diquarks, $[ud] \in (n, p)$, and isovector-pseudovector diquarks $\{dd\} \in n$, $\{ud\} \in (n, p)$, $\{uu\} \in p$.

I. Nucleon Shape from Continuum QCD

Substantial progress has been achieved in the exploration of ground state nucleon structure within continuum QCD approaches with a traceable connection to the QCD Lagrangian [48, 145, 146, 314, 323]. Within continuum QCD approaches, full information on the ground state nucleon structure is encoded in the Faddeev amplitude. This amplitude comes from the solution of the integral equation depicted in Fig. 37. The ground state nucleon Faddeev amplitude is given by the residue at the position of the pole of minimal mass in the partial wave $J^P = 1/2^+$. The kernel in Fig. 37 implies two sources for the dressed constituent quark binding within the nucleon: (*a*) tight, dynamical color-antitriplet quark-quark correlations in the scalar-isoscalar and pseudovector-isotriplet channels and (*b*) exchange associated with diquark breakup and reformation, which is required in order to ensure that each valence-quark participates in all diquark correlations to the complete extent allowed by its quantum numbers.

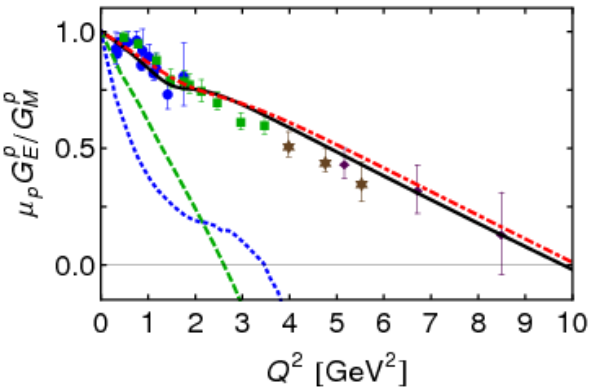

FIG. 38. Continuum QCD prediction for the ratio $\mu_P G_E^P / G_M^P$ [314]: solid (black) curve – full result; dot-dashed (red) – momentum-dependence of the scalar-diquark contribution, including both $L = 0, 1$ nucleon rest-frame quark+diquark orbital angular momentum components. The contribution from configurations of quark+diquark orbital angular momentum L=0 resulting in a spherical nucleon shape is shown by the dashed (green) curve, while the dashed (blue) curve shows the contribution from the pseudovector diquark, which can generate a deformation in the intrinsic frame of the nucleon. All partial contributions have been renormalized to produce unity at $Q^2 = 0$. Data: circles (blue) [363]; squares (green) [364]; asterisks (brown) [365]; and diamonds (purple) [366].

In Fig. 38 we compare the experimental data on the ratio of electric to magnetic proton form factors, $\mu_P G_E^P / G_M^P$, with results computed using the Faddeev equation solution outlined above [314]. Here we also show (green dashed curve) the contribution from the configuration corresponding to the orbital angular momentum between the quark and scalar diquark in the proton rest frame L=0 (S-wave). This contribution gives rise to the spherically symmetric shape of the nucleon in its intrinsic frame. However, the pseudovector diquark correlations (shown by blue dashed line) also contributes to the ground state nucleon structure. Owing to the presence of the selected direction in the intrinsic nucleon frame defined by the pseudovector, it becomes possible to generate a deformed shape of the nucleon in its intrinsic frame.

In Fig. 39 the relative contributions of the configurations of different quark+diquark orbital angular mo-

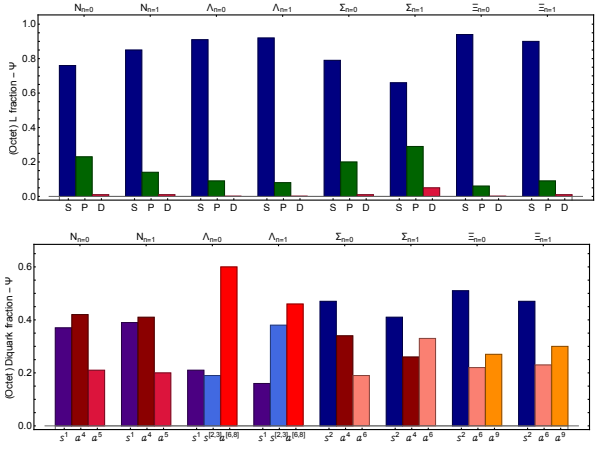

FIG. 39. Octet baryon ground states ($n = 0$) and their first positive-parity excitations ($n = 1$). Upper panel – Baryon rest-frame quark-diquark orbital angular momentum fractions: $L = 0$ (S), $L = 1$ (P) and $L = 2$ (D). Lower panel – Relative strengths of various diquark components within the indicated baryon's Faddeev amplitude: scalar diquark (s) and pseudovector diquarks (a, a). The superscripts here indicate quark flavor content. This is listed for the neutron and proton in Fig. 37. (Details provided in Ref. [323].)

menta in the nucleon rest frame, as well as the contributions from scalar and pseudovector diquark correlations computed using the methods of continuum QCD [323] are shown. Based on these expectations for the ground state nucleon structure, we conclude that the contributions from pseudovector diquark correlations, together with the admixture of the configurations with non-zero quark-diquark orbital angular momenta, may generate a nucleon deformation in its intrinsic frame.

Confirming the continuum QCD expectations in comparison with the experimental data on ground and excited state nucleons, as well as atomic nuclear structure opens up a new avenue in the joint research efforts between nuclear and hadron physics.

1. *Validating Theory Predictions on the Nucleon Shape*

The Faddeev equation depicted in Fig. 37 includes: (a) the dressed quark propagator with the momentum-dependent dressed quark mass, (b) the diquark correlation amplitude Γ, and (c) the diquark propagator. The CLAS results on the nucleon resonance electroexcitation amplitudes ($\gamma_v pN^*$ photo-/electrocouplings) offer an excellent opportunity to validate the continuum QCD evaluations for the momentum dependence of the dressed quark mass, the so-called dressed quark mass function. The s tructure of all excited nucleon states is encoded in their respective Faddeev amplitudes ψ_{N^*}, which are the solution of the similar Faddeev equations for the partial waves and with the diquark correlations allowed and determined by the resonance quantum numbers.

The consistent results on the dressed quark mass function available from independent continuum QCD studies of nucleon elastic form factors and electroexcitation amplitudes for resonances of distinctively different structure, $\Delta(1232)3/2^+$ and $N(1440)1/2^+$, strongly support the credible evaluation of the dressed quark mass function and the dressed quark propagator within continuum QCD [171]. Comparison between the continuum QCD expectations on the $\gamma_v pN^*$ photo-/electrocouplings for other excited nucleon states [145] with the experimental results from CLAS [6] will further validate the continuum QCD evaluation of the dressed quark propagator starting from the QCD Lagrangian.

The spin-parities for the diquark correlations contributing to N^* structure are unambiguously determined by the resonance spin-parity. Therefore, studies of the $\gamma_{r,v} pN^*$ photo-/electrocouplings for all prominent nucleon resonances will allow us to explore all relevant types of diquark correlations within nucleon structure. In this way, the experimental results on the $\gamma_{r,v} pN^*$ photo-/electrocouplings will provide for the adequate description of the diquark correlation amplitudes Γ and the diquark propagators obtained within the continuum QCD approaches. The description of diquark correlations in the nucleon structure can also be checked by making predictions for the meson$' \to$meson time-like transition form factors. These form factors should be computed by employing the Bethe-Salpeter amplitudes associated with the meson partners of a given diquark correlation, ranging over all diquarks relevant for the structure of all prominent N^* states. The meson-transition time-like form factors predicted in this way can be confronted with the future experimental results, thus bridging the efforts between studies of meson and baryon structure with the outcome of particular interest for the exploration of nucleon shape in connection with the nucleon deformation impact on the structure of atomic nuclei.

2. *From Nucleon Structure to the Structure of Atomic Nuclei*

In order to gain insight on the shape of the nucleon in its intrinsic frame, the ground state nucleon Faddeev amplitude should be transformed into the light-front wave function [327] to allow a probabilistic interpretation for the matter distribution within the nucleon. A special approach should be developed to allow us to express the ground state nucleon light-front wave function in terms of the superposition of the Elliott SU(3) eigenvectors projected into the light front. Each of these vectors (λ, μ) corresponds to the contribution of a certain and well-known shape. Therefore, the decomposition of the ground state nucleon light-front wave function over the set of (λ, μ) SU(3) eigenvectors will provide the information on the co-existence of different shapes that generate the resulting nucleon shape in its intrinsic frame.

An alternative pathway in the search for the intrinsic

nucleon deformation is the computation of the pretzelosity h_{1T} TMD structure function. Its non-zero values will offer evidence for the intrinsic nucleon deformation. The presence of the nucleon deformation is implied by the tensor structure of the projection operator for the pretzelosity [367]. Comparison of the experimental results on h_{1T} from the SIDIS data with the expectations from continuum QCD, with all elements of the Faddeev equation kernel checked against the results on the nucleon elastic and transition form factors, will bridge the efforts between the N^* and DIS physics in the exploration of hadron structure, in particular, shedding light on the nucleon's shape.

In order to reveal the impact of the nucleon shape on the structure of atomic nuclei, the nucleons should be treated in the many-body nuclear physics computations as space-extended objects of the certain shape, in contract with most previous studies of the nuclear structure where the nucleons were considered as point-like objects. As a starting point, the structure of the simplest nuclei ^{2}H, ^{3}H, ^{3}He, and ^{4}He should be described accounting for the space-extension of the nucleons, paving the way for description of complex nuclei as bound systems of spatially extended nucleons [13]. Besides the shape of the nucleon, nuclear structure is also determined by nucleon interactions within atomic nuclei. Therefore, the emergence of nucleon interactions from strong QCD should also be elucidated. As a first step, the NN interaction amplitudes should be related to the dressed quark and the dressed gluon interactions within nucleons and pions. This work is in progress within the continuum QCD approaches [172].

Eventually, the emergence of nuclear structure from the interactions between the dressed quarks and gluons confined within the nucleons and mesons will be explored. The success in this challenging adventure will certainly open up a new chapter in the experimental studies of nuclear structure in nuclear-nuclear, photon-nucleus, and electron-nucleus collisions.

V. PHENOMENOLOGY FOR THE EXTRACTION OF QCD INTERPRETABLE HADRON PARAMETERS

A. Advances in Multi-Channel Amplitude Analyses

Partial-wave analysis provides the link between large-scale experimental programs and theory approaches that focus on the intermediate-energy region, where quark confinement manifests itself in a rich spectrum of resonances and where the key to our understanding of the strong interaction will be found. Improved and extended analysis techniques are necessary to further our understanding of baryon structure and, in particular, help resolve the missing-resonance problem, formulated as a priority in the 2015 Long-Range Plan of the National Science Advisory Council (NSAC).

The intermediate-energy region holds the key to our understanding of confinement and its manifestation in a rich phenomenology of resonances. Partial-wave analysis (PWA) of experimental data reveals the spectrum of these resonances. It, thus, provides the bridge to compare experiments with theories such as Quark Models [149, 368–375], Dynamical Dyson-Schwinger approaches [48, 376–379], Chiral Unitary calculations [380–392], and Lattice QCD simulations [343, 393–403]. Note that, in the latter two approaches, one can directly compare theory to partial waves assuming that finite-volume, discretization, and quark mass effects are under control in lattice QCD calculations (see, e.g Refs. [404–406]).

Our knowledge of the baryon spectrum, as determined from analyses of experimental data, has advanced rapidly [1] over the past decade. The progress has been most significant for non-strange baryons, due largely to the wealth of new and more precise measurements made at electron accelerators worldwide. The majority of these new measurements have been performed at Jefferson Lab (using the CLAS and Hall A detectors), with the MAMI accelerator in Mainz (the Crystal Ball/TAPS detector being particularly well suited for the measurement of neutral final states), and with the Crystal Barrel detector at ELSA in Bonn.

While most of the early progress [407–410] in baryon spectroscopy was based on the analysis of meson-nucleon scattering data, particularly pion-nucleon scattering ($\pi N \to \pi N$, $\pi N \to \pi\pi N$), photon-nucleon interactions offer the possibility of detecting unstable intermediate states with small branchings to the πN channel. Many groups have performed either single-channel or multi-channel analyses of these photo-induced reactions. In the more recent single-channel analyses, fits have typically used isobar models [411, 412] with unitarity constraints at the lower energies, K-matrix-based formalisms, having built-in cuts associated with opening inelastic channels [413], and dispersion-relation constraints [412, 414]. Multi-channel fits have analyzed data (or, in some cases, amplitudes) from hadronic scattering data together with the photon-induced channels. These approaches have utilized unitarity more directly. The most active programs are being carried out by the Bonn-Gatchina [415], Jülich-Bonn (JuBo) [167], ANL-Osaka [346], Kent State [410], JPAC [416], and Giessen [417] groups. At low energies the chiral MAID analysis provides a comprehensive description of photo and electroproduction data [418].

1. From Photo to Electroproduction

Our knowledge of the baryon spectrum has rapidly evolved over the last decade, due largely to the refinement of dynamical and phenomenological coupled-channel approaches for the analysis of pseudoscalar-meson photoproduction reactions. The electroproduction process is closely related but, so far, no unified coupled-channel

analysis of photo and electroproduction experiments exists that simultaneously studies the πN, ηN and ΛK final states, where the Q^2 variation of resonance couplings is expected to provide a link between perturbative QCD and the region where quark confinement sets in.

Going from photo- to electroproduction of pseudoscalar meson, the number of helicity amplitudes increases from four to six, requiring more measurements for the analogous 'complete experiment' [419, 420], with a multipole decomposition adding longitudinal components to the transverse elements anchored by photoproduction analyses at $Q^2 = 0$. Variation of resonance couplings with Q^2 is expected to provide a link between perturbative QCD and a region where quark confinement requires the use of lattice QCD, ChPT, or more phenomenological approaches. Exactly where this transition occurs is not precisely known. The well-known prediction [421] of an E2/M1 ratio, for the $\Delta(1232)$ state, approaching unity shows no sign of occurring, remaining essentially flat at a small negative value. In contrast, other clear resonances, such as the $N(1520)$, do show rapid behavior in the low-Q^2 region, followed by a smooth transition to higher values of Q^2.

The reliable determination of helicity amplitudes for $Q^2 > 0$ is also relevant for neutrino physics. Neutrino oscillation experiments are currently evolving from the discovery to the precision era. At this stage, systematic errors will become comparable to the statistical ones. A deeper understanding and realistic modeling of neutrino interactions with the detector target is therefore required. At the future DUNE experiment, most of the interaction events will be inelastic, demanding an accurate description of weak meson (typically pion) production. The multipole decomposition of the electroproduction amplitude provides a powerful framework incorporating all the valuable experimental information available to constrain the corresponding weak processes. Furthermore, methods to extract information about the axial nucleon inelastic current from measurements in detector materials containing hydrogen are being developed. The possibility of performing new measurements of neutrino cross sections on elementary targets is also being considered. In such a scenario, our formalism is particularly well suited to extract useful information about the axial properties of the inelastic nucleon current at various kinematics. See also Ref. [422] for progress in this direction.

Recent advances in the baryon spectrum, based upon real-photon data analyzed via dynamical and phenomenological coupled-channel models, have not yet been fully reproduced in the realm of electroproduction. Electroproduction experiments, e.g., by the CLAS collaboration at JLab, are producing a wealth of data that, in many cases, still await a detailed analysis, in pion electroproduction [157, 423–425] (JLab), [426] (A1 collaboration at MAMI), η electroproduction [196] (JLab), [427] (A1 collaboration at MAMI), and kaon electroproduction [428] (A2 collaboration), [429] (JLab). Analyses at JLab continue; for example in the near future data on $\pi^0 p$ differential cross sections at $0.3 < Q^2 < 1.0$ GeV^2 and $1.1 < W < 1.8$ GeV will be released [430].

Reaction	Observable	Q^2 [GeV]	W [GeV]	Ref.
$ep \to e'p'\eta$	σ_U, σ_{LT}, σ_{TT}	$1.6 - 4.6$	$2.0 - 3.0$	[196]
	σ_U, σ_{LT}, σ_{TT}	$0.13 - 3.3$	$1.5 - 2.3$	[158]
	$d\sigma/d\Omega$	$0.25 - 1.5$	$1.5 - 1.86$	[431]
$ep \to e'K^+\Lambda$	P_N^0	$0.8 - 3.2$	$1.6 - 2.7$	[432]
	σ_U, σ_{LT}, σ_{TT}, $\sigma_{LT'}$	$1.4 - 3.9$	$1.6 - 2.6$	[433]
	P'_x, P'_z	$0.7 - 5.4$	$1.6 - 2.6$	[434]
	σ_T, σ_L, σ_{LT}, σ_{TT}	$0.5 - 2.8$	$1.6 - 2.4$	[435]
	P'_x, P'_z	$0.3 - 1.5$	$1.6 - 2.15$	[436]

TABLE I. Overview of ηp and $K^+\Lambda$ electroproduction data measured at CLAS for different photon virtualities Q^2 and total energy W. Based on material provided by courtesy of D.S. Carman (JLab) and I. Strakovsky (GW).

In Table I, CLAS data on η and kaon electroproduction are summarized. The much longer list for pion electroproduction is omitted here for brevity. Many pion electroproduction data are already included in the SAID database [437]. It should also be stressed that pion and kaon electroproduction experiments with the new CLAS12 detector at the 12 GeV upgrade of Jefferson Lab [438–440] will provide many data that require a timely analysis.

The ANL-Osaka group is currently extending its dynamical coupled-channel analysis of pion electroproduction [441] to higher Q^2-values [168]. Plots of the $\Delta(1232)$ amplitudes at the resonance pole position (yielding a complex amplitude) also seem to qualitatively reproduce results found for the MAID and SAID analyses [442]. However, results have generally been restricted to the low-energy $\Delta(1232)$ and $N(1440)$ states.

The most widely used single-pion electroproduction analyses, covering the resonance region, have been performed by the Mainz (MAID) [411] and Jefferson Lab [154, 156] groups. An extensive single-pion electroproduction database, and a K-matrix based SAID fit, is also available [443]. Eta electroproduction has been analyzed in the Eta MAID framework [444], and kaon electroproduction by the Ghent group [445]. These fits have generally utilized a Regge [446] or Regge-plus-resonance approach [447] at high to medium energies. (We mention here parenthetically that the Ghent Regge approach can be improved by correctly implementing the local gauge-invariance constraints [448].) Effective Lagrangian and isobar models have also been used [449, 450], with some of these available via the MAID website, for both kaon and eta electroproduction [444].

These are all single-channel analyses with approaches similar to the associated real-photon fits, but generally, with the exception of the MAID and SAID analyses, not including the real-photon data as a constraint at $Q^2 = 0$. Both the MAID and Jefferson Lab groups have made fits using a Breit-Wigner plus background models with reso-

nance couplings extended to include a Q^2 dependence. In the Jefferson Lab analyses [156], a further fit was again based on satisfying fixed-t dispersion relation. It should be mentioned that two-pion electroproduction fits have also been performed, and compared to the single-pion results, at Jefferson Lab [4, 21, 451, 452]. See Ref. [4] for a review.

We emphasize that the electromagnetic resonance properties are encoded in the helicity couplings. In the past, they have often been defined as Breit-Wigner couplings, *i.e.*, a Breit-Wigner plus background term was fitted to the energy-dependent multipoles or helicity amplitudes that are a superposition of multipoles. The couplings are real by construction, but not unambiguously defined. Instead, a reaction-independent definition of helicity couplings is only possible by utilizing residues of the resonance poles, since it is these singularities in the complex energy plane and their properties that lead to resonance shapes for real physical scattering energies. See Ref. [442] for recent work of our group towards this goal. Indeed, such a definition is reasonable because many hadronic models can only compare to the transition form factors at the pole, as in the unitarized versions of Chiral Perturbation Theory [453–456] or perturbative calculations using the complex mass scheme [457, 458]. Transition form factors at the complex pole position are complex themselves. which adds a new and independent piece of information compared to the reaction-dependent definition in terms of Breit-Wigner parameters [442, 457].

2. Recent Progress with the Juelich-Bonn and SAID Analysis Frameworks

The Juelich-Bonn analysis is currently upgraded to simultaneously analyze pion, eta, and kaon photo- and electroproduction reactions. A few recent developments in the joint analysis effort of the SAID and Juelich-Bonn group are highlighted in the following.

Data from the CLAS collaboration at Jefferson Lab have been incorporated into the SAID website. These have included neutron-target (deuteron) measurements of pion photoproduction cross sections and the beam-target polarization observable (E). Data were fitted via multipole analyses that were included in the associated publications of these datasets [459, 460]. Similarly, the beam asymmetry Σ in η photoproduction was analyzed using the JuBo approach and published with the CLAS collaboration [461]; an intriguing structure in the data, close to the position of a supposed pentaquark, could be conventionally explained in terms of interference effects. The JuBo approach reached a major milestone by analyzing the world database of $K^+\Lambda$ photoproduction [462]. This reaction is particularly interesting due to the richness of polarization data available from experiments at Jefferson Lab, ELSA, and MAMI. Two resonances claimed by other groups could be confirmed and properties of known states could be determined with greater precision.

The SAID, JuBo, and other groups compared their analysis frameworks and the impact of new high-precision data in a common effort [463]. This synergistic study revealed that the new data brought the analyses significantly closer together although differences still remain.

In anticipation of future electroproduction data from JLab, the SAID group has analyzed baryon transition form factors at the resonance pole [442] in collaboration with Lothar Tiator and Alfred Švarc. For the $\Delta(1232)$, existing SAID and MAID transition form factors showed qualitative agreement, apart from $R_{SM}(Q^2)$ at intermediate values of Q^2.

In collaboration with Tiator (Mainz) and Wunderlich (Bonn), we have also re-examined the connections between complete experiments and truncated multipole analyses for both pion photoproduction and pion electroproduction. New relationships were discovered [419, 464]. Studies of the phase-ambiguity problem, associated with amplitude analyses, were conducted in collaboration with the Mainz, Bonn, and Zagreb groups [465, 466]. These studies have more clearly defined the amplitude information that can be extracted from data with minimal input from reaction models.

B. Extension of Amplitude Analyses, Development of Reaction Models for the Extraction of Hadron Parameters from Data

The recent JLab 12 GeV upgrade, the proposed EIC, and the continued precision experimental efforts at accelerator facilities around the world all aim to explore the dynamics of strong QCD and hadron structure. These experiments necessitate close collaboration between experimentalists, phenomenologists, theorists to untangle the underlying physics from measurement. The mission of the Joint Physics Analysis Center (JPAC) at Indiana University and Jefferson Lab is to facilitate this collaboration by developing tools for precision data and amplitude analysis as well as training a new generation of practitioners of hadron/QCD phenomenology.

Amplitude analysis, *i.e.* the construction of models satisfying general quantum mechanical scattering principles (S-matrix theory) to describe physical measurement is a vital step in connecting experiment to the theory of strong interactions. Here we summarize recent JPAC efforts in the this regard with a special focus on amplitude analysis in photo- and electro-production processes.

Many ongoing experiments, *e.g.* the CLAS12 and GlueX experiments both at JLab, rely on diffractive production of mesons recoiling against (excited) nucleons to probe the properties of hadrons. These processes are primarily studied within the framework of Regge phenomenology that provides a rich set of theoretical tools for amplitude analysis. The increased statistics of next-generation experiments necessitate a deeper understanding of the validity of the tools used to extract physical

quantities. In particular, Regge theory predicts the high-energy diffractive production to be factorizable, *i.e.* describe by independent fragmentation of the beam and target. Dynamics of the production arise from the presence of resonances in the exchange channels, so called "reggeon" exchanges. Photon induced, and in particular charge exchanged processes allow the possibility of non-Pomeron reggeons to be exchanges and thus require identifying the dominant contributions in terms of the singularity structure of the amplitude, *i.e.* contribution from leading and daughter Regge poles or Regge cuts. The validity of this Regge factorization hypothesis was recently assessed by a global fit to charge and strange exchange quasi-two body reactions in Ref [467]. In particular kinematic domains where Regge pole models faithfully reproduce observation are identified for reactions dominated by different exchanges (see Fig. 40).

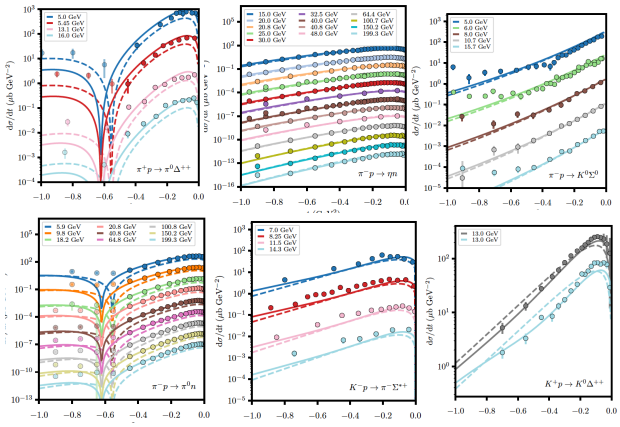

FIG. 40. Sample of results from a global fit of world's data on quasi-elastic charge exchange reactions using Regge poles only.

This framework was then applied to π^0 and η photoproduction off a nucleon in Ref. [416, 468]. Here, analyticity in the form of finite-energy sum rules are used to relate the different energy regimes (*i.e.* the high-energy diffractive regime and the low-energy resonance regime). This provides a rigid constraint on model amplitudes and connects the baryon spectrum dominating the low-energy regime with the mesonic exchanges of Regge dominated peripheral scattering (see Fig. 41).

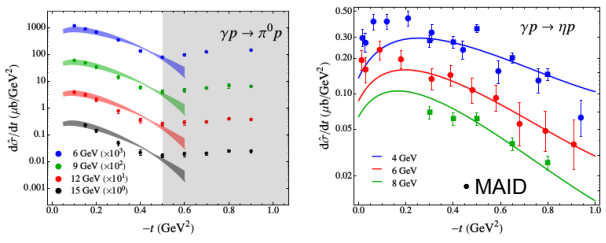

FIG. 41. Finite Energy Sum Rule predictions from pion (left) and eta (right) low-energy partial wave analyses

Similar Regge models are considered in η/η' photoproduction at JLab energies in Ref. [468]. The contributions of hidden-strange exchanges are estimated to give predictions for the ratio of beam asymmetries between the η and η'. An observed deviation from prediction may indicate significant sub-leading contributions (see Fig. 42).

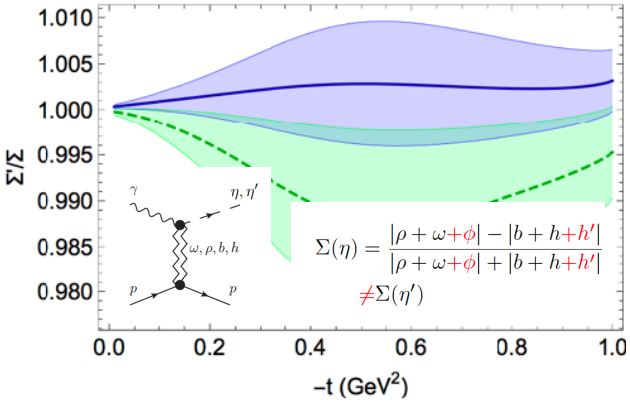

FIG. 42. Regge pole prediction for the ratio of η' to η beam asymmetries.

Subsequent measurement from GlueX indicate agreement with prediction [31]. Generalizations for the beam asymmetries and moments of angular distribution for $\eta\pi^0$ photoproduction have also been recently made [469].

JPAC is also extensively involved in the application of amplitude analysis to search for exotic hadrons. The possibility of structures beyond the usual $q\bar{q}$ or qqq have long been predicted to exist. In particular, hybrid mesons, *i.e.* mesons with an excited gluonic degree of freedom, are expected to be accessible in a variety of reactions and uncovering their properties (*e.g.* masses, widths, decays) provides a window into the role of glue at low-energies. The lowest lying hybrid states are anticipated to exist with exotic quantum numbers $J^{PC} = 1^{-+}$ near 2 GeV. These exotic states, called π_1 states have lead to controversies with experiments reporting the possible existence of two different states, $\pi_1(1400)$ and $\pi_1(1600)$, coupling separately to $\eta\pi$ and $\eta'\pi$ final states. JPAC provided a robust extraction of resonant pole parameters from available COMPASS experiment data that indicates the existence of only one exotic pole that couples to both $\eta^{(\prime)}\pi$ channels [470] (see Fig. 43).

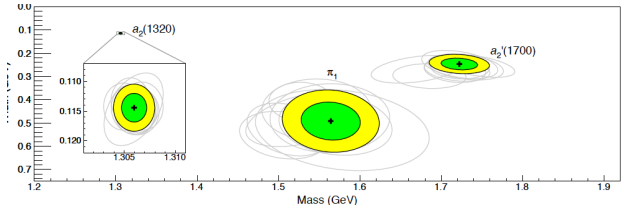

FIG. 43. Pole position of (from left to right) the a_2, π_1, a_2' resonances form analytical fits to the COMPASS partial waves analysis.

The new data coming from dedicated photoproduction

experiments at JLab will prove valuable in testing additional hypotheses.

In addition to hybrid states, the observation of signals with pentaquark-like quantum numbers by the LHCb collaboration [471] spurred immediate interest in searching for these state with photoproduction. JPAC provided first estimates for the branching fraction of these states that serve as a benchmark for the experimental reach of the CLAS12 detector [472]. In an updated analysis incorporating data from the GlueX experiment, the branching fraction estimates and sensitivity of polarization observables accessible at Hall A of JLab are given [473].

VI. MULTI-PRONG HADRON STRUCTURE THEORY FOR EXPLORATION OF STRONG QCD EMERGENCE

A. Description of Hadron Spectrum and Structure Within LQCD

The study of the structure of the nucleon and the pion has long been the subject of an intense lattice-QCD effort. Those studies have focused on the different nucleon charges, the electromagnetic and axial-vector form factors; and on the Bjorken-x moments of parton distribution functions, and of the GPDs and TMDs that encode three-dimensional properties. However, the formulation of lattice QCD in Euclidean space precluded the direct calculation of x-dependent PDFs, GPDs, and TMDs since these are matrix elements of operators separated along the light-cone. The last few years have witnessed a series of advances that have circumvented this restriction [17–19, 99, 474–477], beginning with the Large Momentum Effective Theory (LaMET) [99, 474], through the introduction of pseudo-PDFs [17], to the calculation of the matrix elements of gauge-invariant current-current correlators [477]. Each involves the computation of matrix elements of operators separated in space, with differences in the renormalization prescription and kernel relating the lattice matrix elements to the target light-cone distributions. Since the introduction of these new ideas, there has been an increasing body of calculations of the x-dependent parton distributions both of the nucleon and of the pion, exemplified in Fig. 44.

Our ability to explore the resonance spectrum of QCD has likewise been transformed through the application of the so-called Lüscher method [480] and its extensions, whereby infinite-volume scattering amplitudes can be related to energy-shifts on a Euclidean lattice of finite spatial volume. The current state-of-the-art is to explore multi-channel and inelastic scattering, for which the formulation has recently developed [481, 482]. Together these calculations are providing new insights into the resonance spectrum of QCD, most recently for the σ, f_0 and f_2 mesons, illustrated in the top plot of Fig. 45. With the formalism to explore the resonance spectrum of QCD established, the next challenge is to calculate

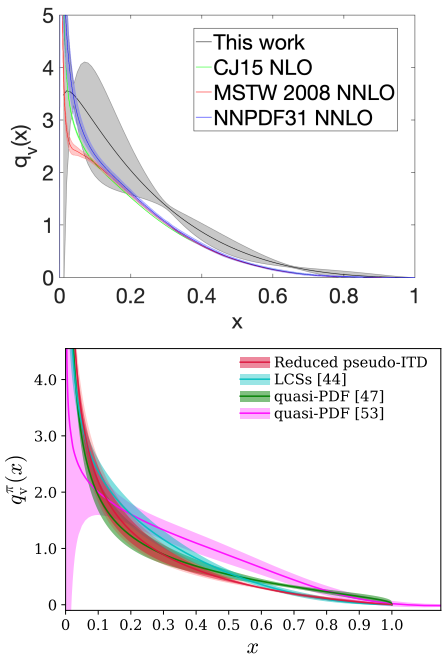

FIG. 44. The top panel shows the unpolarized, isovector PDF of the nucleon using the pseudo-PDF approach [478], obtained on a lattice with $m_\pi \simeq 415$ MeV and spacing $a = 0.127$ fm. The bottom panel shows the valence-quark distribution of the pion using the pseudo-PDF approach [105], compared with calculations using the quasi-PDF [101, 479] and current-current correlator approaches [104].

their structure and transitions through interactions with external currents, where the formalism has also been developed [483], and applied to the calculation of the $\gamma^*\pi \to \pi\pi$ transition, shown as the bottom plot of Fig. 45.

The advent of the exa-scale era in leadership-class computing provides an opportunity for lattice QCD to truly capitalize on both these advances, and to perform *ab initio* calculations that can both extend experimental and QCD-inspired studies, and compute key quantities that are either inaccessible to experiment, or at least highly model dependent. The success at understanding the resonance spectrum for mesons will be extended to provide a first-principles understanding of the computationally more demanding baryons, where few calculations have been performed [486]. Precision studies of the pion will be performed without the need to extrapolate to the pion pole, and form factors of resonances such as the Δ, inaccessible to experiment, will be computed can be computed from first principles. Finally, the contribution of gluons to the structure of hadrons will be explored, in anticipation of the future Electron-Ion Collider. Indeed, the potential of lattice QCD to advance of our understanding of hadrons over the next five has been explored in detail in Refs. [487] and [488].

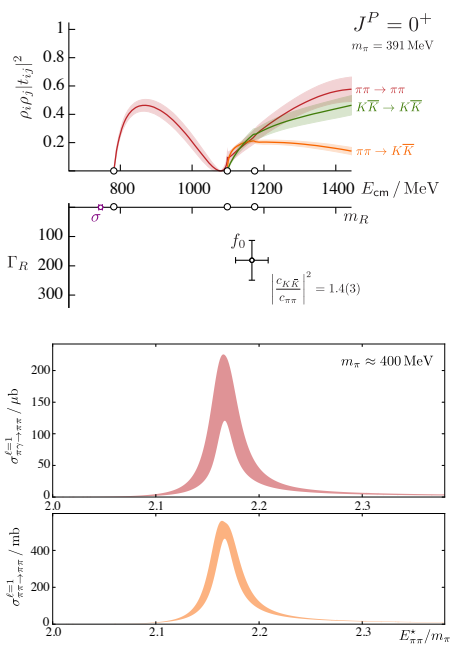

FIG. 45. The top panel shows the coupled $\pi\pi$ $K\bar{K}$ amplitudes in the scalar sector, where the open circles denote the $\pi\pi$, $K\bar{K}$, and $\eta\eta$ thresholds [484]. The bottom panel shows the $\pi^+\gamma \to \pi^+\pi^0$ cross section, together with the elastic $\pi\pi$ scattering cross sections showing the ρ resonance [485].

B. Continuum Strong QCD: Achievements and Prospects

The Faddeev equation was introduced almost sixty years ago [489]. It treats the quantum mechanical problem of three-bodies interacting via pairwise potentials by reducing it to a sum of three terms, each of which describes a solvable scattering problem in distinct two-body subsystems. An analogous approach to the three-valence-quark (baryon) bound-state problem in QCD was explained thirty years ago [338–340]. In this case, owing to EHM and the importance of symmetries [47], a Poincaré-covariant quantum field theory generalization of the Faddeev equation is required. Like the meson Bethe-Salpeter equation, it is natural to consider analyses using such a Faddeev equation within the class of CSMs.

The first direct treatment of the nucleon Faddeev equation is described in Ref. [341]. Following that approach, Refs. [342, 490] calculated the spectrum of ground-state $J = 1/2^+$, $3/2^+$ $(qq'q'')$-baryons, where $q, q', q'' \in \{u, d, s, c, b\}$, their first positive-parity excitations and parity partners. Introducing two parameters, to compensate for deficiencies of the leading-order truncation when used for excited hadrons [491], a description of the known spectrum of 39 such states was obtained, with a mean-absolute-relative-difference between calculation and experiment of 3.6 (2.7)%. This is exemplified in Fig. 46. The framework was subsequently used to predict the masses of 90 states not yet seen empirically.

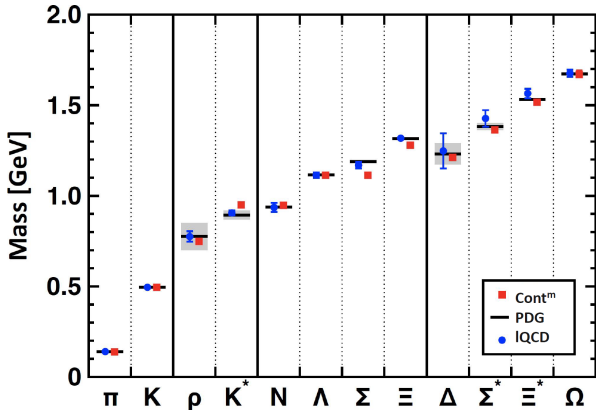

FIG. 46. Masses of pseudoscalar and vector mesons, and ground-state positive-parity octet and decuplet baryons calculated using continuum (squares, red) [342] and lattice [393] methods in QCD compared with experiment (PDG – black bars, with decay-widths of unstable states shaded in gray) [1]. The continuum study did not include isospin symmetry breaking effects, which are evidently small, as highlighted by the empirically determined Σ-Λ mass difference ($\sim 7\%$).

The success of this treatment of the spectrum supports a view that the states are constituted of dynamically dressed quarks bound by exchanges of gluons, which are themselves dressed. Being dressed, the gluons also have a momentum-dependent mass-function as a consequence of EHM; and this function is large at infrared momenta, $m_0 = 0.43(1)$ GeV [53]. Given their role in the Faddeev equation, there is a sense in which the dressed-quarks, whose properties can be and are calculated in QCD [492–494], serve as Nature's embodiment of the constituent-quarks used effectively in bringing order to hadron physics [495, 496]. A key advantage of modern CSMs is their manifestly Poincaré covariant formulation, essential to any treatment of systems involving light quarks, it ensures that wave functions and currents can be used to calculate form factors to arbitrarily large Q^2.

At the other extreme, the symmetry-preserving character of CSMs means that low-Q^2 observables can also be computed and the associated truncation error quantified. An example is provided by the proton's tensor charges $\delta_T q$ [497]:

$$\delta_T q = \int_{-1}^{1} dx\, h_{1T}^q(x) = \int_0^1 dx\, \left[h_{1T}^q(x) - h_{1T}^{\bar{q}}(x)\right] , \quad (4)$$

expressed here in terms of the quark transversity distributions, $h_{1T}^q(x)$. $\delta_T q$ measures the light-front number-density of valence-q quarks with transverse polarization parallel to that of the proton minus that of such quarks with antiparallel polarization; namely, it measures any bias in quark transverse polarization induced by a polarization of the parent proton. These charges are analogs of the nucleon flavor-separated axial-charges, which measure the difference between the light-front number-density of quarks with helicity parallel to that

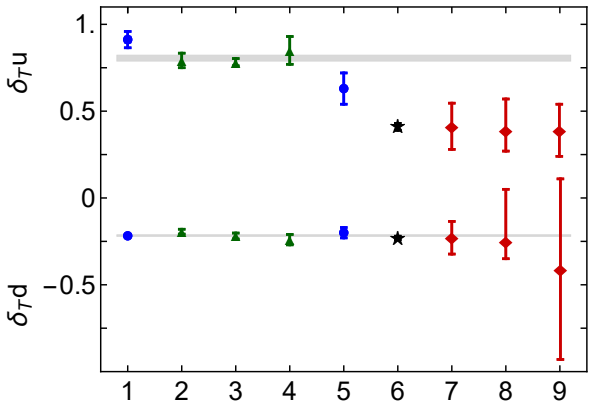

FIG. 47. Comparison of the CSF prediction for the proton's tensor charges, position 1 [497], with those obtained using: LQCD (2 – [498], 3 – [293], 4 – [292]); and a contact-interaction Faddeev equation (5 – [499]). The renormalization scale is $\zeta^2 = 4$ GeV^2 in all these cases; and the gray bands depict the averages in Eq. (5). Position 6 – projected errors achievable at JLab12 with the Solenoidal Large Intensity Device (SoLID) [280], using Eq. (4) and anticipated transversity distribution data. The central values are chosen to match those estimated elsewhere [277] (7, $\zeta^2 = 2.4$ GeV^2) following an analysis of extant transversity distribution data. Earlier estimates from transversity distribution data are also depicted (8 – [259], $\zeta^2 = 2.4$ GeV^2, and 9 – [275], $\zeta^2 = 1$ GeV^2.)

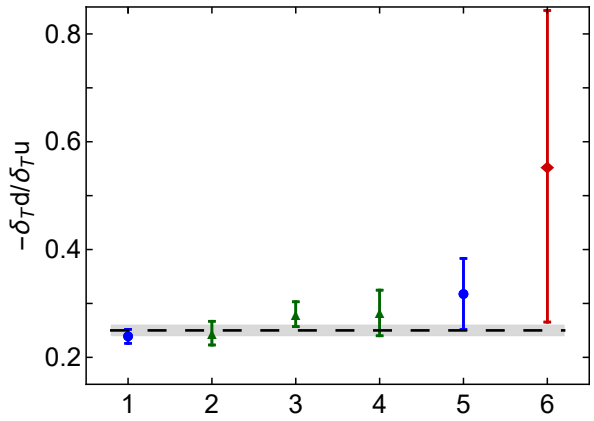

FIG. 48. Ratio $(-\delta_T d/\delta_T u)$. Position 1: CSM result [497]; LQCD: 2 – [498], 3 – [293] and 4 – [292]; contact-interaction Faddeev equation: 5 – [499]. The gray band depicts the weighted average in Eq. (6); and the dashed horizontal line is the quark model result $(-\delta_T d/\delta_T u) = 1/4$ [500]. Position 6 – estimate obtained using Eq. (4) and extant transversity distribution data [277].

of the proton and the density of quarks with helicity antiparallel. In nonrelativistic systems, the helicity and transversity distributions are identical because boosts and rotations commute with the Hamiltonian. Hence, tensor charges are a basic property of the nucleon and may be judged to measure, *inter alia*, the importance of Poincaré-covariance in treatments of the nucleon bound state.

Figure 47 compares the most recent CSF predictions for the proton's tensor charges with those obtained using LQCD [292, 293, 498] and an earlier contact-interaction Faddeev equation study [499]. A weighted combination of the CSF result and recent LQCD values [292, 293, 498] yields the following estimates (gray bands in Fig. 47):

$$\overline{\delta_T} u = 0.805(17)\,,\ \overline{\delta_T} d = -0.216(4)\,. \tag{5}$$

It is evident from the figure that CSF predictions are consistent with recent LQCD values; and produce results for $\delta_T u$ that differ markedly from those obtained via Eq. (4) using extant transversity distribution data.

The mismatch between theory and phenomenology is also apparent in the scale independent ratio $(-\delta_T d/\delta_T u)$, Fig. 48. In this case, the weighted average of theoretical predictions is

$$-\frac{\overline{\delta_T d}}{\delta_T u} = 0.25(1)\,, \tag{6}$$

illustrated by the gray band in the figure. Using a simple non-relativistic quark model spin-flavor wave function, this ratio is 0.25. It is practically the same in the MIT bag model [500]; but, in both cases, the individual tensor charges are measurably larger in magnitude than the modern theory predictions.

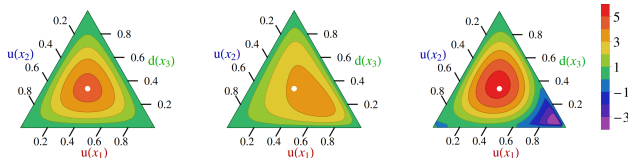

FIG. 49. (Left) Barycentric plots: asymptotic profile, baryon PDA, $\varphi_N^{\rm asy}([x]) = 120 x_1 x_2 x_3$; (Middle) computed proton PDA evolved to $\zeta = 2$ GeV, which peaks at $([x]) = (0.55, 0.23, 0.22)$; and (Right) Roper resonance PDA. The white circle in each panel marks the center of mass for $\varphi_N^{\rm asy}([x])$, whose peak lies at $([x]) = (1/3, 1/3, 1/3)$.

The agreement between CSM and LQCD predictions for the proton's tensor charges increases tension between theory and phenomenology, *viz.* while there is agreement on $\delta_T d$, direct computations of the tensor-charge matrix element produce a value of $\delta_T u$ that is approximately twice as large as that obtained via analyses of extant transversity distribution data. Evidently, it is very important to complete a sound analysis of new data on the proton's transversity distribution.

While a complete treatment of the Poincaré-covariant Faddeev equation is now possible using modern hardware, it remains a complex task. Hence, as remarked in Sec. IV G, for the development of insights in a wide array of baryon problems, it remains common to treat the equation in a quark+diquark approximation, where the diquark correlations are non-point-like and dynamical [314].

One of the predictions of this approach is the $x \to 1$ behavior of the ratio of neutron and proton structure functions, F_2^n/F_2^p [325]. This ratio is a clean probe of the proton's valence-quark structure, exposing crucial features of its wave function. However, for roughly 30 years, theoretical predictions have produced answers over a very wide range, anything between 1/4 and 2/3. Conflicting with common sense, the former may be interpreted as indicating that there are NO valence d-quarks in the proton. In an important step toward a solution of puzzle, a new analysis of the world's data on this ratio [328], accounting for the role of short-range correlations, produces a result in agreement with the quark+diquark CSM picture, *viz.* $\lim_{x\to 1} F_2^n(x)/F_2^p(x) \approx 0.45$. This value is consistent with axial-vector diquarks being a significant part of the nucleon wave function.

The surest path to a picture of the proton with a clean probability interpretation is via projection of the bound-state's Faddeev amplitude onto the light-front. Following this route, the proton's leading-twist dressed-quark PDA was calculated [327]. The result is depicted in Fig. 49.

Table II lists the four lowest-order moments of the proton PDA. They reveal valuable insights, *e.g.* when the proton is drawn as solely a quark+scalar-diquark correlation, $\langle x_2\rangle_u = \langle x_3\rangle_d$, because these are the two participants of the scalar quark+quark correlation; and the system is very skewed, with the PDA's peak being shifted markedly in favor of $\langle x_1\rangle_u > \langle x_2\rangle_u$. This outcome conflicts with LQCD results [501, 502]. On the other hand, realistic Faddeev equation calculations indicate that pseudovector diquark correlations are an essential part of the proton's wave function. When these uu and ud correlations are included, momentum is shared more evenly, shifting from the bystander $u(x_1)$ quark into $u(x_2)$, $d(x_3)$. Adding these correlations with the known weighting, the PDA's peak moves back toward the center, locating at $([x]) = (0.55, 0.23, 0.22)$; and the computed values of the first moments align with those obtained using LQCD. This confluence delivers a more complete understanding of the LQCD simulations, which are thereby seen to validate a picture of the proton as a bound-state with both strong scalar *and* pseudovector diquark correlations, in which the scalar diquarks are responsible for $\approx 65\%$ of the Faddeev amplitude's canonical normalization.

Like ground-state S-wave mesons [503–508], the leading-twist PDA of the ground-state nucleon is both broader than $\varphi_N^{\rm asy}([x])$ (defined by Table II, Row 1) and decreases monotonically away from its maximum in all directions, *i.e.* the PDAs of these ground-state S-wave systems possess endpoint enhancements, but neither humps nor bumps.

As with meson elastic form factors, the veracity of this result for the proton PDA can be tested in future experiments. For instance, it can be used to provide a realistic assessments of the scale at which exclusive experiments involving proton targets may properly be compared with predictions based on pQCD hard scattering formulae [52].

TABLE II. Computed values of the first four moments of the proton and Roper-resonance PDAs. The error on f_N, a dynamically determined quantity that measures the proton's "wave function at the origin", reflects a nucleon scalar diquark content of $65 \pm 5\%$; and values in rows marked with "$\not\supset$ av" were obtained assuming the baryon is constituted solely from a scalar diquark. (All results listed at a renormalization scale $\zeta = 2\,$GeV.)

	$10^3 f_N/\mathrm{GeV}^2$	$\langle x_1\rangle_u$	$\langle x_2\rangle_u$	$\langle x_3\rangle_d$
asymptotic PDA		0.333	0.333	0.333
LQCD [501]	2.84(33)	0.372(7)	0.314(3)	0.314(7)
LQCD [502]	3.60(6)	0.358(6)	0.319(4)	0.323(6)
CSM proton [327]	3.78(14)	0.379(4)	0.302(1)	0.319(3)
CSM proton $\not\supset$ av	2.97	0.412	0.295	0.293
CSM Roper [327]	5.17(32)	0.245(13)	0.363(6)	0.392(6)
CSM Roper $\not\supset$ av	2.63	0.010	0.490	0.500

Analogous to the meson case, the value of this mass-scale is an empirical manifestation of EHM, here within the three-valence-quark proton bound-state.

Additionally, *e.g.* DVMP is sensitive to the wave functions of both the target hadron and final-state meson. Consequently, the predictions being made for these objects using CSMs can be useful for both planning experiments and understanding their outcomes; and progress toward these goals might be achieved by exploiting the predictions via the PARTONs software [111].

As noted above, the quark+diquark Faddeev equation has also been used to elucidate properties of the Roper-resonance [20, 146, 322]. Working with this input, Ref. [327] delivered the associated leading-twist PDA, depicted in the rightmost panel of Fig. 49 and whose first four moments are listed in Table II. The prediction reveals some curious features, *e.g.*: the excitation's PDA is not positive definite and there is a prominent locus of zeros in the lower-right corner of the barycentric plot, both of which echo aspects of the wave function for the first radial excitation of a quantum mechanical system and have also been seen in the leading-twist PDAs of radially excited mesons [509, 510]; and here the impact of pseudovector correlations is opposite to that in the ground-state, *viz.* they shift momentum into $u(x_1)$ from $u(x_2)$, $d(x_3)$.

The character of EHM and the diquark correlations it induces within baryons are also visible in baryon elastic and transition form factors. Particular examples of contemporary significance are neutron and proton elastic form factors, which provide vital information about the structure and composition of the most basic elements of nuclear physics. They are a measurable and physical manifestation of the nature of the nucleons' constituents and the dynamics that binds them together; and new, accurate form factor data are driving paradigmatic shifts in our understanding of these things.

This is particularly clear in analyses of experimental data acquired in the past twenty years, which have im-

posed a new ideal. Namely, despite its simple valence-quark content, the internal structure of the nucleon is very complex, with marked differences between the distributions of total charge and magnetization [364–366, 511, 512] and also between the distributions carried by the different quark flavors [16, 147, 513].

Data available before the year 1999 led to a view that

$$\mu_p \frac{G_E^p(Q^2)}{G_M^p(Q^2)}\Big|_{\rm Rosenbluth} \approx 1, \tag{7}$$

$G_M^p(Q^2=0)/\mu_p = 1$, where $G_{E,M}^p$ are the proton's electric and magnetic form factors; and hence a conclusion that the distributions of charge and magnetization within the proton are approximately identical [514]. Significantly, this outcome is consistent with the simple pictures of the proton's internal structure popular at the time, in which, *e.g.* correlations between quarks and attendant orbital angular momentum play little role.

The situation changed dramatically when the combination of high-energy, -current and -polarization at JLab enabled a new type of experiment to be performed, *viz.* polarization-transfer reactions [511], which are directly proportional to $G_E(Q^2)/G_M(Q^2)$ [515, 516]. A series of these experiments [364–366, 511, 512] has determined that

$$\mu_p \frac{G_E^p(Q^2)}{G_M^p(Q^2)}\Big|_{\rm JLab\,PT} \approx 1 - {\rm constant} \times Q^2, \tag{8}$$

where the constant is such that the ratio might become negative for $Q^2 = 9.8 m_N^2 = 8.7\,{\rm GeV}^2$. This behavior contrasts starkly with Eq. (7); and since the proton's magnetic form factor is reliably known on a space-like domain that extends to $Q^2 \approx 30$ GeV^2 [517, 518], the Q^2-dependence of G_E^p/G_M^p exposes novel features of the proton's charge distribution, as expressed in $G_E^p(Q^2)$.

Numerous analyses have sought to explain the behavior of $G_E^p(Q^2)/G_M^p(Q^2)$; and insights deriving from CSMs are described in Refs. [16, 378].

More recently, a new, indirect approach to the problem has been explored [519]. Consider that the electric form factor of a positively charged vector meson decreases with increasing $x = Q^2/m_{\mathcal{V}}^2$, where $m_{\mathcal{V}}$ is the vector meson's mass. However, setting it apart from that of a pseudoscalar meson, which is positive-definite, the large-x prediction from Refs. [520, 521] suggests that $G_E^{\mathcal{V}}(x)$ may possess a zero at $x \sim 6$. This was the outcome in Ref. [334], which used a symmetry preserving regularization of a contact interaction and was thus able to compute form factors to arbitrarily large x.

In exhibiting a zero crossing, the vector mesons electric form factor, $G_E^{\mathcal{V}}$, can serve as a surrogate for the proton's electric form factor because the reason for the potential appearance of a zero is similar in both cases. For the proton, a zero can be produced by destructive interference between the Dirac and Pauli form factors, and will appear if the transition between the strong and perturbative domains of QCD is pushed to a sufficiently large value of Q^2 [16, 378]. In the vector meson case, there are three elastic form factors: $F_1^{\mathcal{V}}$ is Dirac-like; $F_2^{\mathcal{V}}$, Pauli; and $F_3^{\mathcal{V}}$ is quadrupole-like. Here, $F_{1,3}^{\mathcal{V}}$ are positive and $F_2^{\mathcal{V}}$ is negative; and if the magnetic form factor, $F_2^{\mathcal{V}}$, is removed, then the vector meson's electric form factor is positive-definite at space-like momenta.

The merit of using vector meson studies to locate and explain a zero in the electric form factor of a $J \neq 0$ hadron is the relative simplicity of the two-body continuum bound-state problem as compared to the analogous three-body problem. Ref. [519] calculated the electric charge form factors of $u\bar{d}$ vector mesons, varying the current-quark masses of the valence quarks: realistic, s-quark, c-quark. A zero is found in each case; and importantly, as the current-mass of the system's valence-quarks is increased, the $x = Q^2/m_{\mathcal{V}}^2$-location of the zero, x_z, moves toward $x = 0$:

$\mathcal{V}$	ρ	ρ_s	ρ_c
x_z	10.6(3)	$10.1^{(9)}_{(7)}$	$4.5^{(2.5)}_{(1.0)}$

(9)

The shift is initially slow; but the pace increases as one leaves the domain upon which emergent mass is dominant and enters into that for which explicit (Higgs-connected) mass generation overwhelms effects deriving from strong-QCD dynamics. Reverting to Q^2, the location of the zero in $G_E^{\mathcal{V}}$ moves to larger values with increasing current-quark mass.

Focusing on the ρ-meson case, because the ρ is made from the same valence-quarks as the proton, if one replaces $m_{\mathcal{V}}^2$ by m_N^2,

$$x = 10.6(3) \to Q^2 = 9.4(3)\,{\rm GeV}^2. \tag{10}$$

Using a quark+diquark Faddeev equation to describe the proton, Ref. [16] predicted that G_E^p possesses a zero at $Q^2 = 9.5$ GeV^2. No symmetry protects G_E^p. It can be negative and very likely exhibits a zero in the neighborhood of this point because dressed-quarks have large anomalous magnetic moments that run slowly to zero [522–524]. Once again, the existence of a zero is a consequence of EHM, driven by strong-QCD dynamics.

The existence of a zero in vector meson form factors has another important corollary; namely, single-pole vector meson dominance (VMD), *viz.* $G_E^{\mathcal{V}}(x) \approx 1/(1+x)$, can only be a useful tool for approximating (off-shell) vector meson properties within a limited x-domain. The vector-meson electric form factor presents the best case for a VMD model because it necessarily agrees with the computed result in some neighborhood of $x = -1$ and, by charge conservation, also in the vicinity of $x = 0$. The analysis in Ref. [519] reveals that the discrepancy is less-than 20% within the following regions:

$$\begin{aligned}
\rho &: \ -1 < x < 0.81\,, \\
\rho_s &: \ -1 < x < 0.60\,, \\
\rho_c &: \ -1 < x < -0.96 \ \ \& \ \ -0.15 < x < 0.24\,,
\end{aligned} \tag{11}$$

where the subscript indicates the size of the current-mass for the valence-quarks defining the bound state. Evidently, a single-pole VMD approximation is a fair assumption on a reasonable domain for light-quark systems. However, it is poor for states in which the Higgs-mechanism of mass generation is dominant, *i.e.* $c\bar{c}$ and more massive systems. In fact, without the $x = 0$ constraint imposed by current conservation, a VMD approximation for the $c\bar{c}$ system becomes quantitatively unreliable once bound-state virtuality exceeds 4%. Hence, as highlighted by the analysis in Ref. [525], it is likely that VMD estimates of heavy-quarkonia photo- and electroproduction cross sections are both quantitatively and qualitatively unsound. This question is currently the focus of detailed analysis because, *e.g.* it bears upon flagship experiments aimed at exposing EHM [33, 526].

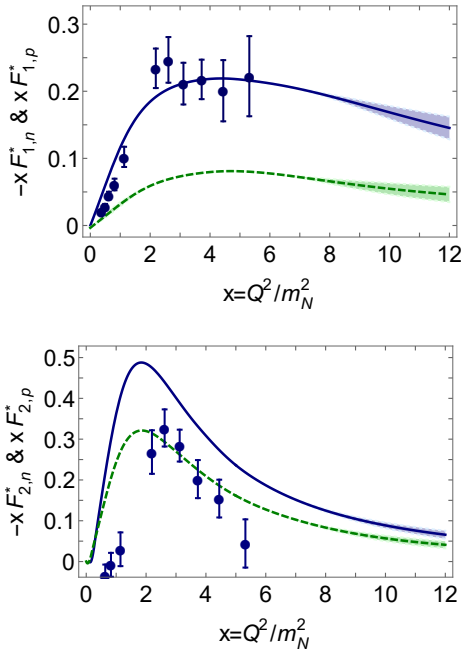

FIG. 50. x-weighted Dirac (top) and Pauli (bottom) transition form factors for the reactions $\gamma^* p \to R^+$ (solid blue curves) and $\gamma^* n \to R^0$ (dashed green curves) reported in Ref. [146]. In all cases, the results on $x \in [6, 12]$ are projections, obtained via extrapolation of analytic approximations to results on $x \in [0, 6]$: at each x, the width of the band associated with a given curve indicates the confidence-level for the extrapolated value. (See Ref. [146] for details.) Data in both panels are for the charged-channel transitions, $F^*_{1,p}$ and $F^*_{2,p}$: circles (blue) [156]. No data currently exist for the neutral channel, but could be obtained using a deuteron to provide the neutron target. In this case, there are indications that the quality of the cross section data should be comparable to that for charged-Roper production off the free proton [527].

Key to completing the analysis in Ref. [519] is the recent development of new numerical techniques for extending the domain of Q^2 upon which CSMs can provide reliable form factor predictions. The approach, which adds a powerful statistical aspect to the Shlessinger point method (SPM) [528–531], was first tested in Ref. [146]. In anticipation of new data from the CLAS12 detector at JLab that will reach to unprecedented photon virtuality, Ref. [146] employed a standard quark+diquark approximation to the three valence-quark bound-state problem to compute $\gamma^* p \to R^+$ and $\gamma^* n \to R^0$ transition form factors on $Q^2/m_N^2 \in [0, 12]$, greatly extending the reach of existing theory predictions [2]. The results are illustrated by the curves in Fig. 50. The precision of the projections in Fig. 50 can be exemplified by quoting the form factor values at the upper bound of the extrapolation domain, $x_{12} = 12$:

$$F^*_{1,p} = 0.0121(14), \qquad -F^*_{1,n} = 0.0039(10), \quad (12a)$$

$$x_{12}F^*_{1,p} = 0.145(17), \qquad -x_{12}F^*_{1,n} = 0.046(11), \quad (12b)$$

$$F^*_{2,p} = 0.0055(8), \qquad -F^*_{2,n} = 0.0034(7), \quad (13a)$$

$$x_{12}F^*_{2,p} = 0.066(10), \qquad -x_{12}F^*_{2,n} = 0.041(9). \quad (13b)$$

The x-weighted form factors were drawn in Fig. 50 so as to accentuate, but not over-magnify, the larger-x behavior of the form factors. On the domain depicted, there is no indication of the scaling behavior expected of the transition form factors: $F_1^* \sim 1/x^2$, $F_2^* \sim 1/x^3$. Since each dressed-quark in the baryons must roughly share the impulse momentum, Q, one should expect that such behavior will only become evident on $x \gtrsim 20$ [532].

Similar techniques are currently being employed to update the predictions in Ref. [16], reanalyzing the brute-force results described therein and delivering predictions for proton and neutron elastic form factors on $x \lesssim 15$.

C. Further Developments of Quark Models for the Description of the Hadron Spectrum, Structure, and GPDs

Why do we use mean-field approaches to describe a baryon? In 1979, E. Witten proposed an ingenious approach to describe a baryon based on large N_c QCD in which a baryon can be viewed as N_c valence quarks bound by the meson mean fields, since the mass of the baryon is proportional to N_c whereas the meson-loop contributions are suppressed by $1/N_c$ [533, 534]. He showed explicitly that in two-dimensional QCD the baryon arises as a bound state of N_c valence quarks by the meson mean fields. It resembles a well-known Hartree approximation. The presence of the N_c valence quarks polarize the Dirac sea or the QCD vacuum, which in turn affects self-consistently the N_c valence quarks. The chiral quark-soliton model (χQSM) was constructed such that this self-consistent Hartree picture is realized [535–537]. As a result, the baryon emerges as a soliton that consists of the N_c valence quarks. We can summarize the features of the χQSM.

- A meson mean-field theory
- A model based on relativistic quantum field theory

- A model that incorporates chiral symmetry and its spontaneous breakdown
- A very constraint model with all parameters fixed in the mesonic sector
- It is related to strong or non-perturbative QCD via the instanton vacuum

The χQSM starts from the effective chiral action (EχA), which contains the dynamical quarks and the pseudo-Goldstone boson fields:

$$S_{\rm eff} = -N_c {\rm Tr} \log \left[i\partial\!\!\!/ + i\sqrt{M(i\partial)} U^{\gamma_5} \sqrt{M(i\partial)} + i\hat{m} \right], \tag{14}$$

where M denotes the dynamical quark mass and U^{γ_5} the pseudo-Goldstone boson field. $\hat{m}$ represents the mass matrix of the current quarks in flavor space $\hat{m} = {\rm diag}(m_{\rm u}, m_{\rm d}, m_{\rm s})$. In fact, chiral symmetry and its spontaneous breakdown determines the explicit form of the EχA given in Eq. (14). A specific quark-gluon dynamics is encoded in the dynamical quark mass. However, local models such as the NJL model and the chiral quark model do not provide any information on the internal quark-gluon dynamics. On the other hand, if one considers the QCD instanton vacuum, which was investigated by D. Diakonov and V. Petrov [538], the dynamical quark mass arises as a momentum-dependent one. Moreover, the instanton vacuum determines not only the explicit form of the momentum-dependent quark mass but also its value at the zero virtuality by the saddle-point approximation that is justified in the large N_c limit. In the χQSM constructed from the instanton vacuum, the renormalization point inheres naturally [539]. This is indeed very important, when one compares the results from the χQSM. Since the EχA (14) contains all orders of the effective chiral Lagrangian, the model is distinguished from the Skyrme model, which was constructed by the truncated effective chiral Lagrangian. Moreover, if one turns off the self-consistent interaction between the mean fields and valence quarks, the model produces the results of the well-known nonrelativistic quark model (NRQM). Thus, the model interpolates between the Skyrme model (large soliton size) and the NRQM (zero soliton size) [536].

Since the momentum-dependence of the quark mass causes additional complexity, the quark mass is often taken to be constant, which brings about a regularization to tame divergences arising from quark loops. The χQSM has been successfully applied to the description of properties of the lowest-lying light baryons over decades [536]. Recently, the model has been utilized to explain singly heavy baryons [540, 541]. Taking the limit of the infinitely heavy mass of the heavy quark ($m_Q \to \infty$), one can view a singly heavy baryon as $N_c - 1$ light valence quarks bound by the pion mean field. In this limit, the spin of the heavy quark is conserved, which makes the spin of the light degrees of freedom [542–545]. By exactly the same self-consistent procedure, a singly heavy baryon comes about again as a chiral soliton but a bosonic and colored one [540, 546–548]. Combining it with the heavy quark that is considered to be a mere static color source, we can construct a singly heavy baryon. Thus, the χQM has a virtue of explaining the light and singly heavy baryons on an equal footing.

What have we studied for the structures of the baryons Within the framework of the χQSM, various observables of the baryons have been examined: we list some of them as follows:

- Mass spectra of the SU(3) baryons [549, 550]
- Electromagnetic form factors of the baryon octet and decuplet [551–554]
- Transition magnetic moments of the SU(3) baryons [555]
- Axial-vector form factors of the baryon octet and decuplet [556, 557]
- Parity violation and Strange vector form factors of the nucleon [558–560]
- Tensor charges and tensor form factors of the nucleon [561–565]
- Gravitational form factors of the nucleon [566]
- Semileptonic hyperon decays [567–569]
- Unpolarized quark distributions (twist-2) of the nucleon [539, 570]
- Transversity distributions of the nucleon [571]
- Antiquark distributions and unpolarized flavor asymmetry [572]
- Quasi-parton distributions of the nucleon [573]
- Electromagnetic form factors of singly heavy baryons [574, 575]
- Excited Ω_cs as exotic baryons [576, 577]
- Generalized parton distributions [578]

Possible extensions of the χQSM The present version of the χQSM is mainly applicable to the lowest-lying baryons. In order to explain the mass spectra and properties of both the excited light and heavy baryons, we have to extend the mean-field approximation. To do that, we need to take into account at least four important physics:

- Inclusion of the vector, axial-vector, and tensor mean fields [579]
- Confining background fields
- $1/N_c$ meson-loop fluctuations
- Momentum-dependent dynamical quark mass [580]

So far, the χQSM contains only the pion mean field, which is represented by the single pion profile function. Once we introduce the vector, axial-vector, and tensor structures, we have to determine the twelve different profile functions [579], which is technically not at all an easy task. Nevertheless, they should be included, since some of excited baryons can decay into vector mesons and lower baryon states. In general, a valence quark or quarks in a excited baryon should be excited to the next level. It implies that certain confining effects should be taken into account to keep the valence quarks stay in the excited baryon. Unfortunately, the confining background field cannot be derived or determined self-consistently. Moreover, it should be saturated at a certain scale such that the confining string is broken or a meson is created. Unfortunately, there is no consistent and rigorous theory on the quark confinement. We can only resort to phenomenological methods to incorporate it.

When a valence quark is excited in the baryon, it is natural that there must be a quark-antiquark correlation, which corresponds to the $1/N_c$ meson-loop fluctuations. Considering these $1/N_c$ meson loops means that we have to go beyond the mean-field approximation. It bears resemblance to the RPA approximation in nuclear physics but it requires more involved investigation. So far, we have turned off the momentum dependence of the dynamical quark mass. However, the momentum-dependent quark mass embraces quark-gluon dynamics arising from the instanton vacuum. In particular, when it comes to the quark distribution amplitudes and generalized parton distributions, it is essential to take into account the momentum-dependent quark mass.

Future investigation on the baryon properties Once the χQSM is successfully extended, one can perform the investigations on the structures of excited light and heavy baryons. We can present some examples as follows:

- Mass spectra of excited light and heavy baryons
- Strong decays of the excited baryons
- Various form factors of the excited baryons
- Decays of heavy baryons to light baryons
- Light-cone distribution amplitudes of the baryons and form factors at higher Q^2 regions and in the time-like region

In particular, the transitions from the heavy baryons to the light baryons require additional theoretical efforts. Since the heavy and light baryons have different meson mean fields, one has to scrutinize the transitions between different meson mean fields.

Conclusion The chiral quark-soliton model is a robust and viable model for the description of the structure of baryons. It has the great virtue that explains the light and heavy baryons on an equal footing. Moreover, since it is a model based on relativistic quantum field theory, it can describe not only the static properties and form factors of the baryons but also the internal quark structure of the baryons such as the quark distributions, generalized parton distributions, light-cone distribution amplitudes, and so on. Since the renormalization point of the model is well defined from the instanton vacuum, results from the model can be directly compared with both the experimental data and those from lattice QCD data.

D. Light-Front Holography and Supersymmetric Conformal Algebra: A Novel Approach to Hadron Spectroscopy, Structure, and Dynamics

Recent insights into the non-perturbative structure of QCD based on the gauge/gravity correspondence and light-front (LF) quantization, *light-front holography* for short [581], have lead to effective semiclassical bound state equations for mesons and baryons where the confinement potential is determined by an underlying superconformal algebraic structure [582–584]. The formalism provides a remarkably first approximation to QCD, including its hidden supersymmetric hadronic features. The resulting light-front wave equation allows the familiar tools and insights of Schrödinger's nonrelativistic quantum mechanics and the Hamiltonian formalism to be applied to relativistic hadronic physics [585–587]. It should be noted that supersymmetry in this approach is supersymmetric quantum mechanics [588] and refers to bound state wave functions and not to elementary quantum fields.

Our work in this area can be traced back to the original article of Polchinski and Strassler [589], where the exclusive hard-scattering counting rules [590, 591] were derived from the warped geometry of Maldacena's five-dimensional anti-de Sitter AdS_5 space: The hadron in elastic scattering at high momentum transfer shrinks to a small size near the AdS boundary at $z = 0$ where the dual space is conformal (z is the fifth coordinate of AdS space). Hadron form factors (FFs) look very different in AdS space [592] or in physical spacetime [593, 594]: One can show, however, that a precise mapping can be carried out at Dirac's fixed light-front time [595] for an arbitrary number of partons [596]. As a result, the impact parameter generalized parton distributions [597, 598] are expressed in terms of the square of AdS eigenmodes, provided that the invariant transverse impact variable ζ for the n-parton bound state is identified with the holographic variable z. For a two-parton system, $\zeta^2 = x(1-x)\mathbf{b}_\perp^2$, the AdS modes are mapped directly to the square of effective light-front wave functions (LFWFs) that incorporate the non-perturbative pole structure of FFs [596]. Similar results follow from the mapping of the matrix elements of the energy-momentum tensor [599].

A semi-classical approximation to light-front QCD follows from the LF Hamiltonian equation $P_\mu P^\mu|\psi\rangle = M^2|\psi\rangle$ with $P = (P^-, P^+, \mathbf{P}_\perp)$. In the limit $m_q \to 0$ the LF Hamiltonian for a $q\bar{q}$ bound state can be system-

atically reduced to a wave equation in the variable ζ [581]

$$\left(-\frac{d^2}{d\zeta^2} - \frac{1-4L^2}{4\zeta^2} + U(\zeta)\right)\phi(\zeta) = M^2\phi(\zeta), \qquad (15)$$

where the effective potential U includes all interactions, including those from higher Fock states. The orbital angular momentum $L = 0$ corresponds to the lowest possible solution. The LF equation has similar structure of wave equations in AdS, and can be embedded in AdS space provided that $\zeta = z$ [581]. The precise mapping allows us to write the LF confinement potential U in terms of the dilaton profile that modifies AdS [600].

The separation of kinematic and dynamic components can be extended to arbitrary integer-spin J by starting from a dilaton-modified AdS action for a rank-J symmetric tensor field $\Phi_{N_1\ldots N_J}$. Variation of the AdS action leads to a general wave equation plus kinematical constraints to eliminate lower spin from the symmetric tensor [601]. LF mapping allows to determine the mass function in the AdS action in terms of physical kinematic quantities consistent with the AdS stability bound [602]. Similar derivation for arbitrary half-integral spin follows for Rarita-Schwinger spinors in AdS [601]. In this case, however, the dilaton term does not lead to an interaction [603] and an effective Yukawa-type interaction has to be introduced instead [604]. Embedding light-front physics in a higher dimension gravity theory leads to important insights into the non-perturbative structure of bound state equations in QCD for arbitrary spin, but does not answer how the effective confinement dynamics is determined and how it can be related to the symmetries of QCD itself?

Conformal algebra underlies in LF holography the scale invariance of the QCD Lagrangian [582]. It leads to the introduction of a scale $\lambda = \kappa^2$ and harmonic confinement, $U \sim \lambda\zeta^2$, maintaining the action conformal invariant [582, 605]. The oscillator potential corresponds to a quadratic dilaton profile and thus to linear Regge trajectories [606]. Extension to superconformal algebra leads to a specific connection between mesons and baryons [584] underlying the $SU(3)_C$ representation properties, since a diquark cluster can be in the same color representation as an antiquark, namely $\bar{3} \in 3\times3$. We follow [607] and define the fermionic generator $R_\lambda = Q + \lambda S$ with anticommutation relations $\{R_\lambda, R_\lambda\} = \{R^\dagger_\lambda, R^\dagger_\lambda\} = 0$. It generates a new Hamiltonian $G_\lambda = \{R_\lambda, R^\dagger_\lambda\}$ that closes under the graded algebra $[R_\lambda, G_\lambda] = [R^\dagger_\lambda, G_\lambda] = 0$. The generators Q and S are related to the generator of time translation $H = \{Q, Q^\dagger\}$ [588] and special conformal transformations $K = \{S, S^\dagger\}$: together with the generator of dilations D they satisfy the conformal algebra. The new Hamiltonian G_λ is an element of the superconformal (graded) algebra and uniquely determines the bound-state equations for both mesons and baryons [583, 584]

$$\left(-\frac{d^2}{d\zeta^2} + \frac{4L_M^2-1}{4\zeta^2} + V_M(\zeta)\right)\phi_M = M^2\,\phi_M, \quad (16)$$

$$\left(-\frac{d^2}{d\zeta^2} + \frac{4L_B^2-1}{4\zeta^2} + V_B(\zeta)\right)\phi_B = M^2\,\phi_B, \quad (17)$$

including essential constant terms in the effective confinement potential $V_{M,B}(\zeta) = \lambda^2_{M,B}\,\zeta^2 + 2\lambda_{M,B}(L_{M,B} \mp 1)$, with $\lambda_M = \lambda_B \equiv \lambda$ (equality of Regge slopes) and $L_M = L_B + 1$ [608]. This is shown in Fig. 51. The mass spectrum from Eqs.(16-17) is $M^2_M = 4\lambda(n + L_M)$ and $M^2_B = 4\kappa^2(n+L_B+1)$ with the same slope in L and n, the radial quantum number. Since $[R^\dagger_\lambda, G_\lambda] = 0$, it follows that the state $|M, L\rangle$ and $R^\dagger_\lambda|M, L\rangle = |B, L-1\rangle$ have identical eigenvalues M^2, thus $R^\dagger_\lambda$ is interpreted as the transformation operator of a single constituent antiquark (quark) into a diquark cluster with quarks (antiquarks) in the conjugate color representation. The pion, however, has a special role as the unique state of zero mass that is annihilated by $R^\dagger_\lambda$, $R^\dagger_\lambda|M, L = 0\rangle = 0$: The pion has not a baryon partner and thus breaks the supersymmetry.

Embedding in AdS is also useful to extend the superconformal Hamiltonian to include the spin-spin interaction: From the spin dependence of mesons [601] one concludes that $G_\lambda = \{R_\lambda, R^\dagger_\lambda\} + 2\lambda s$, with $s = 0, 1$ the total internal spin of the meson or the spin of the diquark cluster of the baryon partner [610]. The lowest mass state of the vector meson family, the ρ (or the ω) is also annihilated by the operator $R^\dagger$, and has no baryon partner: The effect of the spin term is an overall shift of the quadratic mass scale without a modification of the LFWF as depicted in Fig. 51. The analysis was consistently applied to the radial and orbital excitation spectra of the π, ρ, K, K^* and ϕ meson families, as well as to the $N, \Delta, \Lambda, \Sigma, \Sigma^*, \Xi$ and Ξ^* in the baryon sector, giving the value $\kappa = \sqrt{\lambda} = 0.523 \pm 0.024$ GeV from the light hadron spectrum [610]. Contribution of quark masses [611] are included via the Feynman-Hellman theorem, $\Delta M^2 = \langle\sum_q m_q^2/x_q\rangle$, with the effective values $m_u = m_d = 46$ MeV and $m_s = 357$ MeV [586]. The complete multiplet is obtained by applying the fermion operator $R^\dagger_\lambda$ to the negative-chirality component baryon wave function [583, 586] $\phi_B = \{\psi_+(L_B), \psi_-(L_B+1)\}$ leading to a tetraquark bosonic partner, $R^\dagger_\lambda\,\psi_- = \phi_T$, a bound state of diquark and anti-diquark clusters with angular momentum $L_T = L_B$ [610]: The full supermultiplet (see Fig. 52) contain mesons, baryons, and tetraquarks [612]. A systematic analysis of the isoscalar bosonic sector was also performed using the framework described here; the $\eta' - \eta$ mass difference is correctly reproduced [614].

We have shown in Ref. [615] that the basic underlying hadronic supersymmetry still holds and gives remarkable connections across the entire spectrum of light and heavy-light hadrons even if quark masses break the conformal invariance. In particular, the $L = 0$ lowest mass meson defining the $K, K^*, \eta', \phi, D, D^*, D_s, D^*_s, B, B^*, B_s$

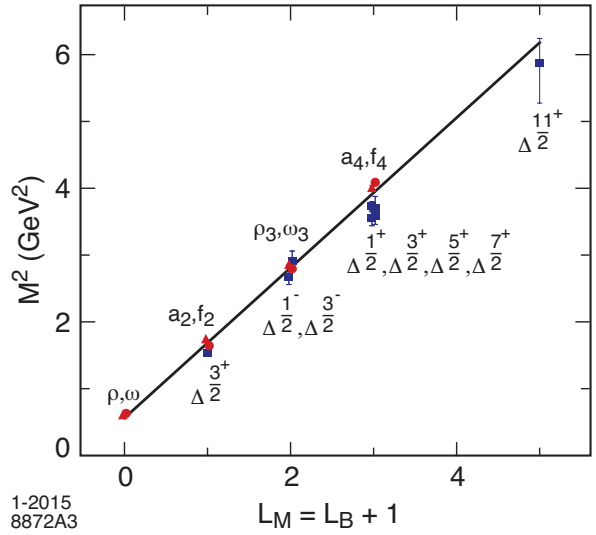

FIG. 51. Supersymmetric vector meson and Δ partners from Ref. [584]. The experimental values of M^2 for confirmed states [1] are plotted vs $L_M = L_B + 1$. The solid line corresponds to $\sqrt{\lambda} = 0.53$ GeV. The ρ and ω mesons have no baryonic partner, since it would imply a negative value of L_B.

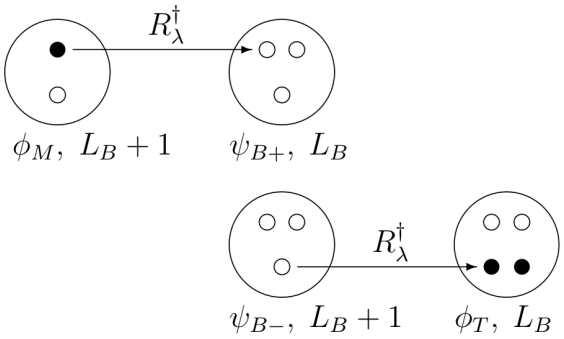

FIG. 52. Supersymmetric 4-plet representation of same-mass and parity hadronic states $\{\phi_M, \psi_{B+}, \psi_{B-}, \phi_T\}$ [610]. Mesons are interpreted as $q\bar{q}$ bound states, baryons as quark-antidiquark bound states and tetraquarks as diquark-antidiquark bound states. The fermion ladder operator $R^\dagger_\lambda$ connects antiquark (quark) and diquark (anti-diquark) cluster of the same color. The baryons have two chirality components with orbital angular momentum L and $L+1$.

and B_s^* families examined in Ref. [615] has in effect no baryon partner, conforming to the SUSY mechanism found for the light hadrons. The analysis was extended in [616] by showing that the embedding of the light-front wave equations in AdS space nevertheless determines the form of the confining potential in the LF Hamiltonian to be harmonic, provided that: a) the longitudinal and transverse dynamics can be factored out to a first approximation and b) the heavy quark mass dependence determines the increasing value of the Regge slope according to Heavy Quark Effective Theory (HQET) [543]. This model has been confronted with data in the detailed analysis performed in [617] including tetraquarks with one charm or one bottom quark as illustrated in Tables III and IV. The double-heavy hadronic spectrum, including mesons, baryons and tetraquarks and their connections was examined in Ref. [618] confirming the validity of the supersymmetric approach applied to this sector. The lowest mass meson of each family, the η_c, J/ψ, η_B, and Y have no hadronic partner and the increase in the Regge slope qualitatively agrees with the HQET prediction. Embedding LF dynamics in AdS allow us to study the infrared (IR) behavior of the strong coupling. In fact, it is possible to establish a connection between the short-distance behavior of the QCD coupling α_s with JLab long-distance measurements of α_s from the Bjorken sum rule [619–622]. In light-front holography the IR strong coupling is $\alpha_s^{IR}(Q^2) = \alpha_s^{IR}(0)e^{-Q^2/4\lambda}$. One can obtain Λ_{QCD} from matching the perturbative (5-loop) and non-perturbative couplings at the transition scale Q_0 as shown in Fig. 53. For $\sqrt{\lambda} = 0.523 \pm 0.024$ GeV we find $\Lambda_{\bar{M}S} = 0.339 \pm 0.019$ GeV compared with the world average $\Lambda_{\bar{M}S} = 0.332 \pm 0.017$ GeV and $Q_0^2 \simeq 1$ GeV^2. Therefore, one can establish a connection between the proton mass $M_p^2 = 4\lambda$ and the perturbative QCD scale Λ_{QCD} in any renormalization scheme.

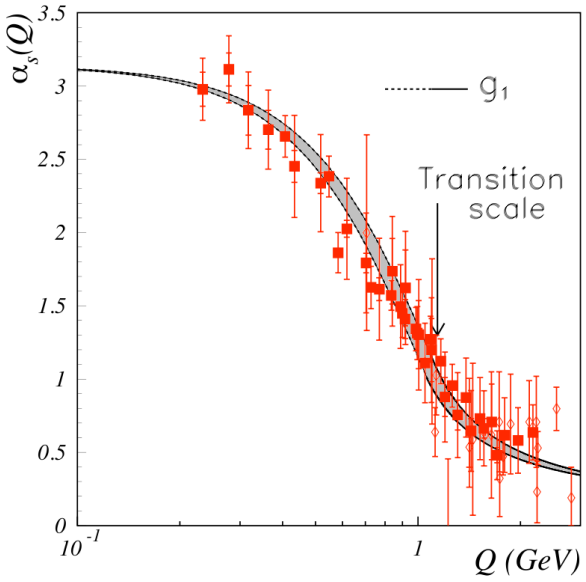

FIG. 53. Matching the non-perturbative and perturbative couplings regimes at 5-loop β-function in the $\bar{M}S$ renormalization scheme and comparison with α_s measurements from the Bjorken sum rule. For $\sqrt{\lambda} = 0.523 \pm 0.024$ GeV we obtain $\Lambda_{\bar{M}S} = 0.339 \pm 0.019$ GeV compared with the world average $\Lambda_{\bar{M}S} = 0.332 \pm 0.017$ GeV [622].

An extensive study of FFs [623] and parton distributions [624, 625] has been carried out recently using an extended model based on the gauge-gravity correspondence, light-front holography, and the generalized Veneziano model [626–628]. The non-perturbative strange and charm sea content of the nucleon has been studied by also incorporating constraints from lattice QCD [629, 630]. Meson [631] and nucleon transition

form factors, such as the proton to Roper $N(1440)1/2^+$ transition, can also be described within the light-front holographic framework [632, 633] and extended to other nucleon transitions [169], such as the transition to the $\Delta(1232)3/2^+$, $N(1520)3/2^-$, $N(1535)1/2^-$, $\Delta(1600)3/2^+$, and $\Delta(1620)1/2^-$ states measured at CLAS [21].

Hadron FFs in the light-front holographic approach are a sum from the Fock expansion of states $F(t) = \sum_\tau c_\tau F_\tau(t)$, where the c_τ are spin-flavor coefficients and $F_\tau(t)$ has the Euler's Beta form structure [626–628]

$$F_\tau(t) = \frac{1}{N_\tau} B\big(\tau - 1, 1 - \alpha(t)\big), \tag{18}$$

where $\alpha(t)$ is the Regge trajectory of the vector meson that couples to the quark current in the hadron. For twist $\tau = N$, the number of constituents in a Fock component, the FF is an $N-1$ product of poles

$$F_\tau(Q^2) = \frac{1}{\big(1+\frac{Q^2}{M^2_{n=0}}\big)\big(1+\frac{Q^2}{M^2_{n=1}}\big)\cdots\big(1+\frac{Q^2}{M^2_{n=\tau-2}}\big)}, \tag{19}$$

located at $-Q^2 = M_n^2 = (n+1-\alpha(0))/\alpha'$, which generates the radial excitation spectrum of the exchanged particles in the t-channel [586, 587]. The trajectory $\alpha(t)$ can be computed within the superconformal framework and its intercept $\alpha(0)$ incorporates the quark masses [629].

Using the integral representation of the Beta function, the form factor is expressed in a reparameterization invariant form

$$F(t)_\tau = \frac{1}{N_\tau}\int_0^1 dx w'(x) w(x)^{-\alpha(t)}\,[1-w(x)]^{\tau-2}, \tag{20}$$

with $w(0) = 0, \quad w(1) = 1, \quad w'(x) \geq 0$. The flavor FF is given in terms of the valence GPD at zero skewness $F^q_\tau(t) = \int_0^1 dx\, q_\tau(x) \exp[t f(x)]$ with the profile function $f(x)$ and PDF $q(x)$ determined by $w(x)$

$$f(x) = \frac{1}{4\lambda}\log\Big(\frac{1}{w(x)}\Big), \tag{21}$$

$$q_\tau(x) = \frac{1}{N_\tau}[1-w(x)]^{\tau-2} w(x)^{-\frac{1}{2}} w'(x). \tag{22}$$

Boundary conditions at $x \to 0$ follow from the expected Regge behavior, $w(x) \sim x$, and at $x \to 1$ from the inclusive-exclusive counting rules [593] $q_\tau(x) \sim (1-x)^{2\tau-3}$ that imply $w'(1) = 0$. These physical conditions, together with the constraints written above, basically determine the form of $w(x)$. If the universal function $w(x)$ is fixed by the nucleon PDFs then the pion PDF is a prediction [624]. The unpolarized PDFs for the nucleon are compared with global fits in Fig. 54.

To study the polarized GPDs and PDFs we perform a separation of chiralities in the AdS action: It allows the computation of the matrix elements of the axial current - including the correct normalization, once the coefficients c_τ are fixed for the vector current [625]. The

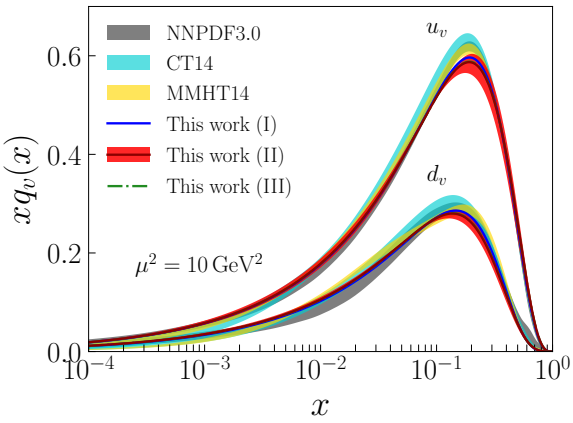

FIG. 54. Comparison of $xq(x)$ in the proton from LF holographic QCD [624] with global fits [634–636] for models I, II and III in [625]. The results are evolved from the initial scale $\mu_0 = 1.06 \pm 0.15$ GeV [622].

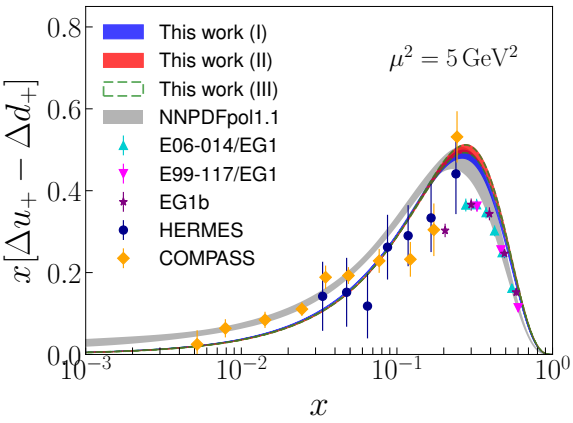

FIG. 55. Polarized distributions of the isovector combination $x[\Delta u_+(x) - \Delta d_+(x)]$ in comparison with NNPDF global fit [637] and experimental data [638–644]. Three sets of parameters are determined from the Dirac form factor and unpolarized valence distributions.

formalism incorporates the helicity retention between the leading quark at large x and the parent hadron: $\lim_{x\to 1} \frac{\Delta q(x)}{q(x)} = 1$, a perturbative QCD result [86]. It also predicts no-spin correlation with the parent hadron at low x: $\lim_{x\to 0} \frac{\Delta q(x)}{q(x)} = 0$. We compare our predictions with available data for spin-dependent PDFs in Fig. 55 and for the ratio $\Delta q(x)/q(x)$ in Fig 56. The first lattice QCD computation of the the charm quark contribution to the electromagnetic form factors of the nucleon with three gauge ensembles (one at the physical pion mass) was performed in Ref. [630]. It gives the necessary constraints to compute the non-perturbative intrinsic charm-anticharm asymmetry $c(x) - \bar{c}(x)$ using the light-front holography approach. The results are shown in Fig. 57 ($q_+ \equiv q + \bar{q}$).

We have shown how the classical equations of mo-

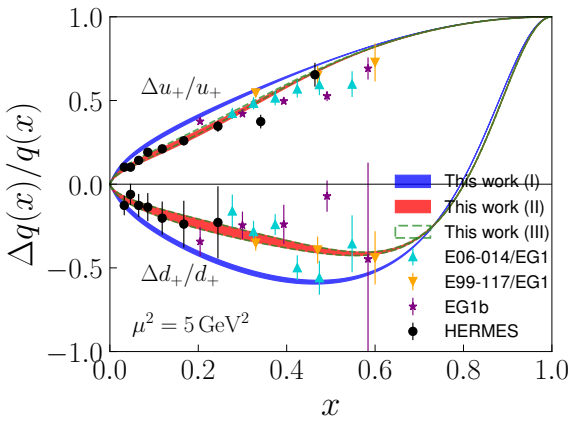

FIG. 56. Helicity asymmetries of $u + \bar{u}$ and $d + \bar{d}$. Symbols as in Fig. 55.

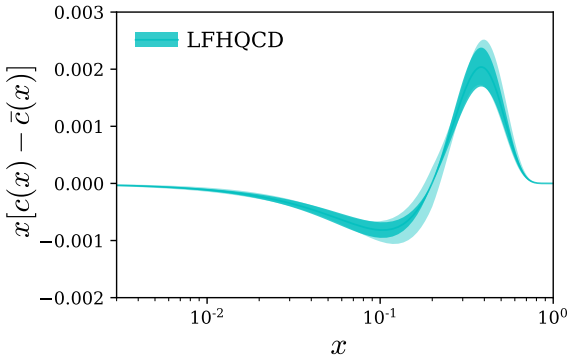

FIG. 57. The distribution function $x[c(x) - \bar{c}(x)]$ computed in the light-front holographic framework using lattice QCD input of the charm electromagnetic form factors [630].

tion for hadrons of arbitrary spin derived from the 5-dimensional gravity theory have the same form of the semiclassical bound-state equations for massless constituents in LF quantization. The implementation of superconformal algebra determines uniquely the form of the confining interaction. This new approach to hadron physics incorporates basic non-perturbative properties that are not apparent from the chiral QCD Lagrangian, such as the emergence of a mass scale and the connection between mesons and baryons. In particular, the prediction of a massless pion in the chiral limit is a consequence of the superconformal algebraic structure and not of the Goldstone mechanism. The structural framework of LF holography also provides nontrivial connections between the structure of form factors and polarized and unpolarized quark distributions with non-perturbative results such as Regge theory and the Veneziano model.

Specific key results, such as the prediction of the ratio $\Delta q(x)/q(x)$ at large x will be tested very soon in upcoming experiments at JLab [645, 646]. The strange-antistrange asymmetry could be explored in semi-inclusive ϕ electroproduction with CLAS 12. Our study of the nucleon to Roper transition form factor will be extended up to $Q^2 = 12$ GeV^2 for comparison with new CLAS data. The prediction of hadron states within superconformal multiplets of meson-baryon-tetraquarks (for example the multiplets shown in Tables III and IV) can motivate the search for new tetraquark states. Many other important applications to hadron physics based on the holographic framework have been studied in addition to the new developments described here; unfortunately it is not possible to review them in this short overview and we apologize to the authors in advance.

VII. CONTRIBUTIONS TO THE USA EIC PHYSICS PROGRAM

With the recent decision by the Department of Energy (DOE), the prospects for the construction the Electron-Ion Collider have been increased significantly. The nucleon 3-D imaging program with exclusive and semi-inclusive processes is of high priority. The expected availability both of highly polarized electrons as well as of polarized protons, either longitudinally (along the beam) or transversely polarized (either in the ep scattering plane or perpendicular to it), will give access not only to the CFF $\mathcal{H}(\xi, t)$ but will directly access the CFF $\mathcal{E}(\xi, t)$, which is related to the gravitational spin form factor $J(t)$, and can therefore help solve the proton's still unresolved spin puzzle of the proton. When comparing the 12 GeV kinematics with the EIC kinematics we have to take into account the much lower luminosity for the EIC in case of unpolarized ep scattering.

However, in the case of polarized proton targets the effective luminosity, *i.e.* taking into account the dilution factor for polarized NH_3, approximately equal to 0.17, the situation is less dramatic. Moreover, for transverse polarization, *e.g.* using a polarized HD target, the expected acceptable effective proton luminosity is $L \approx 0.3 \times 10^{34}$ cm^{-2}s^{-1}, more comparable with the EIC luminosity on polarized protons. The process $\gamma p \to p e^+ e^-$, which is the time-reversed process to DVCS, also accesses the GPDs and Compton Form Factors, but provides direct access to the real part of the Compton amplitude, *i.e.* it complement DVCS, which, in polarized beam experiments directly accesses the imaginary part of the Compton amplitude.

Owing to the high center-of-mass energy, the EIC offers the possibility to study the equivalent 3D and gravitational properties of the glue. Here processes such as $e + p \to e + p + J/\psi$ and $e + p \to e + p + \phi$ may be explored, and in greater detail. Last by not least, the EIC, in particular in its lower energy implementation, can be an excellent tool for spectroscopy especially in the light-flavor and strangeness area, as well as in the X, Y, Z exotic states. In the latter, the nature of the already found states can be explored, for example 4-quarks states versus meson-meson molecules, and dynamical processes near threshold. The slope of the t-dependence in the production cross section can be an effective tool in dis-

TABLE III. Quantum number assignment of different meson families with quarks: $q = u,\ d,\ s$ and one charm quark c and their supersymmetric baryon and tetraquark partners from Ref. [617]. Each family is separated by a horizontal line. For baryons multiplets with same L_B and S_D only the state with the highest possible value for J is included. Diquarks clusters are represented by [ ] have total spin $S_D = 0$, and ( ) represents $S_D = 1$. The quantum numbers $J^P = 1^+$ and $J^P = 2^-$ are assigned to the states $D(2550)$ and $D_J(2600)$, but their quantum numbers have not yet been determined. States with a question mark (?) are the predicted ones. The lowest meson bound state of each family has no baryon or tetraquark partner and breaks the supersymmetry.

Meson			Baryon			Tetraquark		
q-cont	$J^{P(C)}$	Name	q-cont	J^P	Name	q-cont	$J^{P(C)}$	Name
$\bar{q}c$	0^-	$D(1870)$	—	—	—	—	—	—
$\bar{q}c$	1^+	$D_1(2420)$	$[ud]c$	$(1/2)^+$	$\Lambda_c(2290)$	$[ud][\bar{c}\bar{q}]$	0^+	$\bar{D}_0^*(2400)$
$\bar{q}c$	2^-	$D_J(2600)$	$[ud]c$	$(3/2)^-$	$\Lambda_c(2625)$	$[ud][\bar{c}\bar{q}]$	1^-	—
$\bar{c}q$	0^-	$\bar{D}(1870)$	—	—	—	—	—	—
$\bar{c}q$	1^+	$\bar{D}_1(2420)$	$[cq]q$	$(1/2)^+$	$\Sigma_c(2455)$	$[cq][\bar{u}\bar{d}]$	0^+	$D_0^*(2400)$
$\bar{q}c$	1^-	$D^*(2010)$	—	—	—	—	—	—
$\bar{q}c$	2^+	$D_2^*(2460)$	$(qq)c$	$(3/2)^+$	$\Sigma_c^*(2520)$	$(qq)[\bar{c}\bar{q}]$	1^+	$D(2550)$
$\bar{q}c$	3^-	$D_3^*(2750)$	$(qq)c$	$(3/2)^-$	$\Sigma_c(2800)$	$(qq)[\bar{c}\bar{q}]$	—	—
$\bar{s}c$	0^-	$D_s(1968)$	—	—	—	—	—	—
$\bar{s}c$	1^+	$D_{s1}(2460)$	$[sq]c$	$(1/2)^+$	$\Xi_c(2470)$	$[sq][\bar{c}\bar{q}]$	0^+	$\bar{D}_{s0}^*(2317)$
$\bar{s}c$	2^-	$D_{s2}(\sim 2830)$?	$[sq]c$	$(3/2)^-$	$\Xi_c(2815)$	$[sq][\bar{c}\bar{q}]$	1^-	—
$\bar{s}c$	1^-	$D_s^*(2110)$	—	—	—	—	—	—
$\bar{s}c$	2^+	$D_{s2}^*(2573)$	$(sq)c$	$(3/2)^+$	$\Xi_c^*(2645)$	$(sq)[\bar{c}\bar{q}]$	1^+	$D_{s1}(2536)$
$\bar{s}c$	3^-	$D_{s3}^*(2860)$	$(sq)c$	$(1/2)^-$	$\Xi_c(2930)$	$(sq)[\bar{c}\bar{q}]$	—	—
$\bar{c}s$	1^+	$\bar{D}_{s1}(\sim 2700)$?	$[cs]s$	$(1/2)^+$	$\Omega_c(2695)$	$[cs][\bar{s}\bar{q}]$	0^+	??
$\bar{s}c$	2^+	$D_{s2}^*(\sim 2750)$?	$(ss)c$	$(3/2)^+$	$\Omega_c(2770)$	$(ss)[\bar{c}\bar{s}]$	1^+	??

TABLE IV. Same as Table III but for mesons containing one bottom quark b from Ref. [617]. The quantum numbers $J^P = 1^+,\ J^P = 0^+$ and $J^P = 2^-$ are assigned to the states $B_J(5732)$, $B_J^*(5840)$ and $B_J(5970)$, but their quantum numbers have not yet been determined. States with a question mark (?) are the predicted ones. The lowest meson of each family has no baryon or tetraquark partner and breaks the supersymmetry.

Meson			Baryon			Tetraquark		
q-cont	$J^{P(C)}$	Name	q-cont	J^P	Name	q-cont	$J^{P(C)}$	Name
$\bar{q}b$	0^-	$\bar{B}(5280)$	—	—	—	—	—	—
$\bar{q}b$	1^+	$\bar{B}_1(5720)$	$[ud]b$	$(1/2)^+$	$\Lambda_b(5620)$	$[ud][\bar{b}\bar{q}]$	0^+	$B_J(5732)$
$\bar{q}b$	2^-	$\bar{B}_J(5970)$	$[ud]b$	$(3/2)^-$	$\Lambda_b(5920)$	$[ud][\bar{b}\bar{q}]$	1^-	—
$\bar{b}q$	0^-	$B(5280)$	—	—	—	—	—	—
$\bar{b}q$	1^+	$B_1(5720)$	$[bq]q$	$(1/2)^+$	$\Sigma_b(5815)$	$[bq][\bar{u}\bar{d}]$	0^+	$\bar{B}_J(5732)$
$\bar{q}b$	1^-	$B^*(5325)$	—	—	—	—	—	—
$\bar{q}b$	2^+	$B_2^*(5747)$	$(qq)b$	$(3/2)^+$	$\Sigma_b^*(5835)$	$(qq)[\bar{b}\bar{q}]$	1^+	$B_J(5840)$
$\bar{s}b$	0^-	$B_s(5365)$	—	—	—	—	—	—
$\bar{s}b$	1^+	$B_{s1}(5830)$	$[qs]b$	$(1/2)^+$	$\Xi_b(5790)$	$[qs][\bar{b}\bar{q}]$	0^+	$\bar{B}_{s0}^*(\sim 5800)$?
$\bar{s}b$	1^-	$B_s^*(5415)$	—	—	—	—	—	—
$\bar{s}b$	2^+	$B_{s2}^*(5840)$	$(sq)b$	$(3/2)^+$	$\Xi_b^*(5950)$	$(sq)[\bar{b}\bar{q}]$	1^+	$B_{s1}(\sim 5900)$?
$\bar{b}s$	1^+	$B_{s1}(\sim 6000)$?	$[bs]s$	$(1/2)^+$	$\Omega_b(6045)$	$[bs][\bar{s}\bar{q}]$	0^+	??

criminating among such possibilities.

A critical parameter of such an EIC machine is its operating luminosity as all of these exclusive processes are quite rare, and require high luminosity and long beam times to collect sufficient statistics in a multi-dimensional binning. Especially the ξ and t dependence of DVCS cross sections and of the beam and target spin asymmetries are required for the analysis and the Fourier transform of the gravitational form factors in order to extract mechanical properties of the proton and light nuclei.

VIII. RECOMMENDATIONS ON FUTURE JOINT ACTIVITIES BETWEEN EXPERIMENT, PHENOMENOLOGY, AND THEORY

The achievements described in this document, which summarizes the exploration of the spectra and structure of hadrons using experiments with electromagnetic probes and attendant advances in theory for the description of hadron properties, suggests good prospects for gaining insight into the strong QCD dynamics that underlie the generation of the ground and excited state hadrons. In this section we introduce possible future research activities covering a wide field of hadron physics efforts that can all benefit from synergistic engagement between experimentalists, phenomenologists, and theorists.

A. Hadron Spectroscopy

Observations of new missing resonances extend our knowledge about the spectrum of excited nucleon states. They support the relevance of SU(6) spin-flavor approximate symmetry in the generation of the excited nucleon spectrum. This symmetry, however, predicts many resonances in addition to those already discovered within the mass range from 1.7 GeV to 2.5 GeV. Experiments on the studies of exclusive meson photoproduction collecting data on differential cross sections, and single-, double-, and triple-polarization asymmetries, supported by results from experiments with hadron beams, will provide the nearly complete set of data needed to solve the fundamental several-decade-old problem of how the spectrum of nucleons arises from QCD. The amplitude or reaction model analyses of the experimental photoproduction data for the individual exclusive channels as well as within global coupled-channel approaches are critical in order to achieve this objective. Joint research activity between experimentalists in the area of exclusive meson photo-/hadroproduction and the experts in phenomenological data analyses will provide the final results on the spectrum of the excited nucleons as they are seen from the data.

This activity should be extended by the combined studies of exclusive meson photo- and electroproduction data aimed at searches for new resonances. New resonances established in photoproduction can be seen in the electroproduction data too. A successful description of both photo- and electroproduction data within a substantial range of Q^2, with Q^2-independent resonance masses, and total and partial hadronic decay widths, will validate the resonance existence in a nearly model-independent way. The efficiency of this strategy was demonstrated recently by observation of a new $N'(1720)3/2^+$ nucleon resonance from combined studies of CLAS $\pi^+\pi^- p$ photo- and electroproduction data [15]. These studies will benefit from new CLAS12 experimental data. Crucially, the amplitude analyses and reaction models, used successfully in the discovery of new baryon states from photoproduction data, must be extended to electroproduction as part of these efforts.

Searches for new states of baryon matter with glue as an active structural component, the so-called hybrid baryons, are in progress with the CLAS12 detector. Contemporary theory suggests that hybrid baryons may be seen as missing resonances in the W range from 2.0 GeV to 2.5 GeV in the KY and $\pi^+\pi^- p$ exclusive photo-/electroproduction channels. In order to identify the hybrid nature of these resonances, it is necessary to study the Q^2 evolution of the resonance electrocouplings with Q^2-independent hadronic parameters. In regular baryons, the three valence quarks are in a color-singlet configuration, while in hybrid-baryons they are in a color octet configuration. This difference can result in peculiar features of the Q^2-evolution of hybrid baryon electroexcitation amplitudes in comparison with those for three-quark systems. Modeling of the evolution of the hybrid-baryon electroexcitation amplitudes is critically needed for identification of the hybrid baryon states.

Establishing the spectrum of nucleon resonances is important for elucidating the emergence of strong QCD phenomena from the QCD Lagrangian. Coupled-channel analyses of exclusive meson photo- and hadroproduction data have demonstrated that the N^* spectrum is determined by combined contributions from both a dressed-quark core and meson-baryon cloud. Currently, LQCD has offered the potential to describe the N^* spectrum starting from the QCD Lagrangian and accounting for all active components in the resonance structure with an impact on the generation of the N^* spectrum. Therefore, extension of the results on the N^* spectrum are of particular interest for LQCD to advance toward a description of this spectrum using quark masses that approach physical values and accounting for all relevant multi-particle configurations. Approaching the physical masses of the N^* states requires accounting for the resonance hadronic decays. This can be done in joint efforts between LQCD and amplitude analysis theory.

Establishing the resonance spectrum is a key element in understanding the inner workings of QCD, which is the key objective of the various efforts described in this document. Specifically, understanding the nature of color confinement rests in quantitative determination of the role of gluons in the spectrum. Besides baryons, as described above, precision studies of the meson spectrum have and will continue, benefiting from new precision data collected in collider and fixed-target experiments. For example, the GlueX and CLAS12 programs have dedicated experiments to search for light-quark meson resonances in order to identify states that do not fit the conventional quark model. The $J^{PC} = 1^{-+}$ exotic hybrid meson is expected to have mass in the $1.5 - 2$ GeV range with a width that is comparable to that of other resonances with a similar mass [28]. The analysis of the COMPASS data on the $\eta - \pi$ and $\eta' - \pi$ spectrum [647] indicates the existence of a pole in the P-wave partial wave

amplitude consistent with existence of just such a resonance [648]. In addition, phenomenological models [649], lattice QCD [27], and continuum studies [351] imply the existence of other non-$q\bar{q}$ states in the same mass range, possibly containing significant gluonic contributions and filling a quadruplet with $J^{PC} = (0^{-+}, 1^{-+}, 1^{--}, 2^{-+})$ quantum numbers.

The spectrum of mesons with heavy flavors appears to be much richer than predicted by the naive quark model. Some of the XYZ states observed, for example, in e^+e^- annihilation or B-meson decays are candidates for tetraquarks, di-meson molecules, or alternatively could be a kinematic effect associated with exchange forces [650]. To reduce this range of possibilities and identify the key mechanisms for producing these novel phenomena, much higher statistics are needed along with access to similar states in the bottomonium spectrum. This could be achieved at the EIC provided the luminosity is high enough.

The resonance spectrum is determined from partial wave amplitude analysis and requires analytical continuation off the real axis to the complex energy plane. This is an unconstrained problem that is approached by either using a microscopic model, *e.g.* the quark model or a hadronic EFT, or by exploring general analytical properties. The latter result from fundamental properties of the theory, such as unitarity or crossing relations. In principle, they can relate the physical behavior of the system, such as the existence of resonances, to amplitude singularities. Yet, another approach, which has been successfully used for other ill-defined inverse problems, is to use artificial neural networks in a supervised learning approach.

Light-front holography, based on superconformal symmetry, offers predictions for the masses and spin-parities of still unobserved tetraquark states from the known meson and baryon spectra. Searches for these exotic states will bridge efforts in the exploration of meson and baryon spectra.

B. Elucidating N^* Structure in Experiments with Electromagnetic Probes

Analyses of CLAS results on the $N \to N^*$ electroexcitation amplitudes within continuum QCD approaches, quark models, and the coupled-channel approaches have revealed the structure of excited nucleon states as a complex interplay between the inner core of three dressed quarks and an external meson-baryon cloud [2, 21]. The full range of length-scales through which the transition between the combined contribution from the meson-baryon cloud and quark core at intermediate $Q^2 \approx 2.0$ GeV^2 to quark core dominance at high $Q^2 > 5.0$ GeV^2, will be studied using CLAS12 data on exclusive $N\pi$, $N\eta$, KY, and $\pi^+\pi^-p$ electroproduction for 2.0 GeV^2 $< Q^2 <$ 6.0 GeV^2. Precision data on the electroexcitation amplitudes of all prominent resonances at these photon virtualities will allow for exploration of the emergence of a deconfined cloud of mesons and baryons from the core of the three confined dressed quarks.

In order to achieve this objective, strong theory support is critical. Continuum QCD approaches have already demonstrated promising prospects for a description of the emergence of the $N\pi$ component of the meson-baryon cloud from the quark core. The meson-baryon cloud was incorporated or described effectively in quark models [166, 169, 357, 358]. Accounting for the complexity of the subsequent meson-baryon final state interactions requires the full machinery developed in coupled-channel approaches for the global multi-channel analyses of hadro-, photo-, and electroproduction data [346]. A description of the Q^2-evolution of resonance electroexcitation amplitudes at $Q^2 < 3.0$ GeV^2 represents an important milestone for the LQCD efforts.

Synergistic efforts between experimental studies of resonance electroexcitation amplitudes and theory support in describing emergence of the meson-baryon cloud are required to understand the complex interplay between the inner quark core and the external meson-baryon cloud in the structure of distinct excited nucleon states. This is especially true because such interactions are likely to depend sensitively on the quantum numbers of the states involved.

C. Exposing the Emergence of Hadron Mass

The Higgs mechanism accounts for only a small part of the proton's mass. The main part comes from the strongly interacting gluon field. In particular, the so called "trace anomaly", whose strength is driven by gluon self-interactions, is the most important part; yet, it is the least understood [651–653]. Owing to the computational difficulty, lattice QCD has no direct predictions thus far. It would be very valuable for the the lattice QCD community to deliver sound predictions in the near future. Experimentally, a potentially promising method is to measure heavy quarkonium production near threshold, which models have related to the trace anomaly [654, 655]. Precision measurements of J/ψ threshold production are planned with SoLID [255, 656] and CLAS12 at JLab [657]. Threshold Υ production measurements have been discussed for the EIC [658]. These measurements may assist in revealing the trace anomaly's contribution to the proton mass.

Consistent results on the momentum dependence of the dressed quark mass from independent studies of nucleon elastic form factors and the electroexcitation amplitudes of the $\Delta(1232)3/2^+$ and $N(1440)1/2^+$ resonances have demonstrated the capability of gaining insight into the dynamics underlying the dominant part of hadron mass generation [16, 20, 21]. In the near-term, experimental results on the resonance electroexcitation amplitudes will become available from CLAS exclusive meson electroproduction data for all prominent nucleon resonances in the

mass range up to 2.0 GeV and at photon virtualities Q^2 up to 5.0 GeV^2 [5, 6]. Future analyses of these experimental results within the continuum QCD approach will enable us to map out the dressed quark mass function from independent studies of the electroexcitation amplitudes of many different excited nucleon states. Mapping the momentum dependence of the dressed quark mass from the electroexcitation amplitudes of different resonances will either validate the universality of this function or demonstrate an environmental sensitivity of this key feature of strong QCD and the structure of hadrons.

The experimental results on N^* electroexcitation amplitudes available and expected from the CLAS exclusive electroproduction data at $Q^2 < 5.0$ GeV^2 allow us to explore the dressed quark mass function at quark momenta < 0.7 GeV that correspond to distance scales with the fully dressed quarks bound within the quark core in the regime of quark-gluon confinement. The CLAS12 results on the electrocouplings of all prominent nucleon resonances in the mass range up to 3.0 GeV will become available at $Q^2 < 12$ GeV^2 [438]. The first results on the resonance electroexcitation amplitudes within this Q^2 range will allow us to map out the momentum dependence of the dressed quark mass over the length scales whereupon the transition from quark-gluon confinement to pQCD regime is expected. The continuum QCD analyses of the CLAS12 results on nucleon resonance electroexcitation amplitudes at 5.0 GeV$^2 < Q^2 < 12$ GeV^2 will address a key open problem in the Standard Model on the emergence of the dominant part of hadron mass from QCD. Consistent results on the dressed quark mass function from the independent studies of electroexcitation amplitudes of many resonances with different structure will provide credible insight into the dynamics of hadron mass generation in a nearly model-independent way. Progress toward this challenging objective requires coordinated efforts between experimental research on resonance structure and QCD-connected theory analyses capable of describing nucleon resonance electroexcitation amplitudes.

The dressed quark mass function that unifies experimental results on nucleon elastic form factors and $N \to N^*$ transition electroexcitation amplitudes can also be used for the computation of pion electromagnetic form factors and PDFs within continuum QCD approaches. Hence, conclusions drawn about the dynamics of hadron mass generation through studies of the ground/excited-state nucleon structure can be validated via comparisons between experimental results on pion form factors/PDFs and the predictions from continuum QCD obtained with the same dressed quark mass function.

Studies of the pion elastic form factor and valence-quark PDFs using the Sullivan processes represent an important research thrust in Halls A/C during the JLab 12 GeV era [77]. Independent results on the pion PDFs are expected from pion-induced Drell-Yan reactions in upcoming measurements with the new AMBER hadron facility at CERN [659]. Future experiments with an EIC will further increase the kinematic coverage over Q^2 and x in exploration of the structure of the pion and other mesons consisting of heavier quarks. Furthermore, studies with the EIC will reveal details of the interference between competing contributions from the dressed quark masses and the attractive interaction between quarks and anti-quarks that is constrained by DCSB to produce the very small physical pion mass. These results are crucial for understanding the dual nature of the pion as (*i*) a bound quark system and (*ii*) the Goldstone boson emerging with DCSB [8].

Reliable information on the dressed quark mass function for light u and d quarks will be crucial in the exploration of the momentum dependence of the s quark mass function via experimental results on the kaon electromagnetic form factor and PDFs [8]. Kaon structure will be explored in Sullivan processes in Halls A/C at JLab. Continuum QCD analyses of these results using the dressed u-quark mass function determined in studies of the structure of pions and ground/excited state nucleons will allow the s quark mass function to be charted. Such exploration of the flavor dependence of hadron mass generation will deliver unique information on the evolution of hadron mass generating mechanisms from light u and d quarks, with the largest contributions from DCSB, to the heaviest t quark, for which the Higgs mechanism is overwhelmingly dominant. With continuum QCD predicting an approximate balance between the DCSB and Higgs-mechanism contributions to the s-quark mass, studies of the structure of hadrons with s-quarks are particularly interesting.

The evolution of hadron mass generation with quark flavor represents a novel direction in hadron physics. The dressed quark mass function for s and c quarks can be mapped out in studies of the elastic and transition form factors in the time-like region for the mesons and baryons that carry these quark flavors and are produced in exclusive photo-/electroproduction channels. Such experiments require a further increase of the electron beam energy beyond the available 12 GeV at JLab, while achieving a luminosity not less than 10^{35} cm^{-2}s^{-1} presently achieved with the CLAS12 detector in Hall B. Notably, this value of required luminosity is beyond that expected for the US Electron-Ion Collider. Further doubling of the JLab energy (up to 24 GeV) while maintaining the currently available luminosity in Hall B will pave a new avenue in hadron physics, *viz.* charting the evolution of the dynamics of hadron mass generation with quark flavor.

Synergistic efforts in the exploration of meson and baryon structure in both the space- and time-like regions are very important for resolving key open problems in the Standard Model; namely, solutions to the puzzles of: the emergence of hadron mass; the evolution of hadron mass generation dynamics with quark flavor; and understanding quark gluon confinement and its probable intimate connection with DCSB.

D. The Structure of Atomic Nuclei from Strong QCD

Studies of monopole, quadrupole, and rotational collective states of atomic nuclei have demonstrated the relevance of approximate SL(3,R) symplectic symmetry as the leading organizing principle for the structure of the atomic nuclei over a broad range of nuclear mass numbers A from light to intermediate ranges. The important expectation from this symmetry group supported by experimental studies in low-energy nuclear physics is that nuclear deformation and shape coexistence dominate the entire nuclear landscape [12, 361]. The above background on symmetry informed advances in *ab initio* approaches for studying the structure of atomic nuclei is coupled with progress in gaining a description of the ground state structure of nucleons from a strong QCD perspective within continuum QCD approaches. These studies address two important questions: (*i*) whether the ground state of a nucleon in its intrinsic frame is spherical or deformed, and (*ii*) how do the interactions between nucleons within nuclei driven by strong QCD generate the dynamic deformation found in atomic nuclei?

Empirical access to nucleon deformation is provided by the pretzelosity TMD-distribution, with a non-zero value of the zeroth-order pretzelosity moment indicating a nucleon deformed in its intrinsic frame.

Theoretically, continuum QCD approaches, using well-constrained dressed quark mass functions and diquark correlation amplitudes, mapped out in studies of experimental results on nucleon elastic form factors and $N \to N^*$ transition electroexcitation amplitudes, are capable of evaluating the nucleon's light-front wave function. This quantity can yield a complete theoretical description of the nucleon's shape in its intrinsic frame. Moreover, addressing the emergence of the dynamical deformation seen in the structure of atomic nuclei, continuum QCD approaches can also describe the pion-exchange part of the NN-interaction with a $NN\pi$ vertex inferred from strong QCD within the same framework used for the description of nucleon shape. Building with these results, theoretical approaches for the description of the structure of atomic nuclei as multi-nucleon bound systems can relate such expectations from continuum QCD to structural features of atomic nuclei, which are explored in low-energy nuclear physics experiments.

Synergistic efforts in the experimental studies of the ground state nucleon and N^* structure, as well as TMD-pretzelosity, combined with developments in continuum QCD approaches and the theory of atomic nuclear structure, pave the way towards understanding how the structure of atomic nuclei emerges from strong QCD. The predictions from these studies on particular features in the structure of light and medium-heavy atomic nuclei will promote experimental efforts in low-energy nuclear physics, motivating experiments at FRIB and at other nuclear physics facilities around the world.

E. The Longitudinal Structure of Nucleons

There are a number of recent and upcoming experiments at JLab to study nucleon longitudinal structure in the high x_B (valence quark) region, including measurements of the d/u ratio [127, 128, 660] and the spin asymmetries A_1^n [638, 645] and A_1^p (that allow extractions of $\Delta u/u$ and $\Delta d/d$). High-x_B provides a clean region to test theory and model predictions; in particular, to study the interplay between strong and perturbative QCD. These precision data will provide stringent tests of our understanding of strong QCD when comparing with theoretical calculations.

Moments of the spin structure functions can be directly compared to theoretical predictions through sum rules. Recent and forthcoming measurements [661, 662] of the zeroth moments (spin sum rules) and second moments (spin and color polarizabilities) provide direct comparisons with theoretical calculations (LQCD and chiral effective theory), helping to gain insight on chiral symmetry and its breaking pattern in QCD.

The progress achieved in the exploration of nucleon resonance electrocouplings opens up new prospects to gain insight into nucleon PDFs at large values of Bjorken x_B within the resonance excitation region. For the first time, the resonance contributions to the inclusive structure functions F_1 and F_2 have been evaluated from experimental results on the resonance electroexcitation amplitudes from CLAS [160]. Knowledge of the resonant contributions will enable us to extend results on the unpolarized, spin-averaged nucleon PDFs, summed over all parton flavors, toward large x_B in the resonance region. The inclusive F_1 and F_2 structure functions can be computed as the sum of the term evaluated from the parameterized PDFs [7] plus the resonant contribution evaluated with resonance electrocouplings from the CLAS results, as described in Ref. [160], and compared with experimental data. A combined fit of the PDF parameters to the data, both in the resonant and DIS regions, will make it possible to gain new information about the nucleon PDFs in the resonance region at the highest achievable x_B values, limited by the applicability of the factorization theorem.

These studies are strongly motivated by theory advances in the description of the nucleon PDFs starting from the QCD Lagrangian within the novel quasi- and pseudo-PDF concepts [17–19]. This new avenue can forge synergistic efforts between experimentalists, phenomenologists, and theorists toward understanding the emergence of the unpolarized, spin-averaged PDF from the QCD Lagrangian with coverage over x_B values in the resonance region for the first time. These studies will also reveal the interplay between the resonant and non-resonant contributions in inclusive structure functions, allowing exploration of quark-hadron duality and its evolution at distance scales from the regime of quark-gluon confinement to pQCD. Data taken during the 12 GeV era at JLab will establish the photon virtuality range within

which nucleon resonances remain a relevant contributor to inclusive electron scattering.

Light-front analyses have made interesting predictions on the presence of partons heavier than the u and d quarks in the ground state nucleon at large x_B. This prediction is based on the behavior of the light-front wave functions that support minimal off-shellness for these partons at large x_B [663, 664]. This effect was not expected from the usual gluon splitting mechanism. Studies of ϕ and J/ψ semi-inclusive meson electroproduction in experiments at the 12 GeV JLab and further extension of these efforts with the EIC offer prospects to check this important and novel prediction.

F. 3D Nucleon Structure and its Emergence from QCD

Advances in the exploration of DVCS and DVMP have already provided initial insight into the structure of the nucleon in the 3D space defined by x_B and the two spatial coordinates in the plane transverse to the virtual photon. This progress with DVCS [11] promises to deliver a chart of the pressure distribution in nucleons, extending access to the ground state nucleon energy-momentum tensor. Progress in SIDIS studies offers a complementary picture of the nucleon structure in 3D momentum space. 3D nucleon femtography represents a central direction in the JLab 12 GeV physics program. Synergistic interactions between different areas in hadron physics that use electromagnetic probes are of particular importance as attempts are made to extend the range of insights into the 3D structure of the nucleon and, potentially, its excited states; especially in connecting observations with emergent phenomena in QCD.

So far, GPD structure functions have been related to DVCS/DVMP observables assuming the contribution from handbag diagrams and, in the case of DVCS, also from the Bethe-Heitler amplitude. However, the DVCS/DVMP exclusive channels at $W < 2.5$ GeV should also include contributions from well-established resonances excited in the virtual photon/proton s-channel. Use of the resonance electroexcitation amplitudes determined independently from the CLAS/CLAS12 exclusive meson electroproduction data (see Section IV C) offers a realistic evaluation of the resonant contributions to the DVCS/DVMP processes at the amplitude level. Accounting for nucleon resonance contributions to DVCS/DVMP will allow for extension of the scope of the 3D nucleon structure studies toward smaller invariant masses of the virtual photon/proton system. Adding the resonant contributions to the diagrams traditionally used in DVCS/DVMP analyses will enable exploration of how stable the information on ground state nucleon GPD structure functions is against the implementation of the other relevant amplitudes. Moreover, these studies will reveal whether there is a need for further extension of the analysis frameworks used for the extraction of GPDs.

Available information on the 3D structure of the ground state nucleon will be augmented by novel results on the 3D structure of nucleon excited states as soon as the transition $N \to N^*$ GPDs are determined from exclusive $\gamma_v p \to N\pi\gamma_r$ electroproduction data. Studies with CLAS have demonstrated pronounced resonance-like peaks in the $N\pi$ invariant mass for these final states at mass values corresponding to the Δ resonance, and to the second and third resonance regions seen in inclusive/exclusive electroproduction. These structures in the $N\pi$ invariant mass are suggestive of contributions from the processes $\gamma_v p \to \gamma_r N^* \to N\pi\gamma_r$. The $\gamma_v p \to \gamma_r N^*$ amplitudes contain the transition $N \to N^*$ GPDs, allowing them to be constrained by fitting to observables in the $\gamma_v p \to \gamma_r N\pi$ exclusive channel. This activity requires input from theory on modeling the off-diagonal $N \to N^*$ transition GPDs. Experimental information on the N^* electroexcitation amplitudes from CLAS/CLAS12 will provide valuable constraints on the modeling of transition GPDs.

Continuum and lattice QCD approaches promise a connection between the 3D images of the nucleon, from the GPD and TMD distributions, and the strong QCD dynamics underlying formation of the ground state nucleon. Indeed, continuum QCD approaches are capable of computing the nucleon's light-front wave function by employing dressed quark mass functions and diquark correlation amplitudes evaluated with a traceable connection to the QCD Lagrangian. Such a step is valuable because all GPDs and TMDs can be evaluated from the nucleon's light-front wave function.

Studies of GPDs and TMDs within continuum QCD approaches may not only elucidate the emergence of hadron mass, but also allow for investigation of the relevance and emergence of diquark correlations in the structure of ground state nucleons. As was discussed in Section VI B, continuum QCD approaches predict particular features in the nucleon and Roper resonance PDAs related to the generation of two types of diquark correlation with spin-parities 0^+ and 1^+. In the computed PDAs, the momenta of two of the quarks are much closer in comparison with the momentum of the third quark, suggesting that two of the quarks are correlated and the third quark is uncorrelated. Furthermore, implementation of the two types of diquark correlations, 0^+ and 1^+, shifts the continuum QCD expectations for the PDA moments more into line with existing LQCD results (see details in Section VI B). Studies of ground state nucleon structure in 3D offer experimental opportunities to check these expectations, obtained within two conceptually different approaches to solving the problem posed by the QCD Lagrangian.

Knowledge of the ground state nucleon light-front wave function will allow us to evaluate the GPD and TMD structure functions. They can be then be inserted into the reaction models that relate the GPDs/TMDs to the DVCS/SIDIS observables. The successful description of

many different DVCS and TMD observables will validate the reaction models used in order to connect the GPDs and TMDs to the measured observables.

The first results on the pressure distribution in the nucleon and results on the moments from different combinations of GPDs will experimentally constrain many components of the energy-momentum tensor within the ground state nucleon. Sound theory predictions for these quantities are therefore much in demand. Meeting this requirement is a challenging task; but it is essential if science is to fully capitalize on planned experiments and facilities.

Completing a 3D femtography program relating to ground and excited state nucleons, including charting their mechanical properties, will considerably enhance understanding of the strong QCD dynamics underlying baryon generation. Success requires the combined efforts of experimentalists, phenomenologists, and theorists, both from N^* and DIS physics.

ACKNOWLEDGMENTS

We are grateful to the following people for constructive comments during the preparation of this manuscript: I. Aznauryan D. Binosi, L. Chang, X. Chen, F. De Soto, A. Deur, M. Ding, R. Ent, F.-X. Girod B.-L. Li, T. Liu, N. Markov, M. Nielsen, J. Papavassiliou, E. Pasyuk, K. Raya, E. Santopinto S.M. Schmidt, C. Shi, R.S. Sufian, S.-S. Xu, P.-L. Yin, S. Zafeiropoulos, J.-L. Zhang, and L. Zou.

We also express our gratitude to SURA/JSA and Deputy Director of Jefferson Lab R. McKeown for generous support of this workshop, as well as to the JLab Event Services group for their efficient help in the workshop organization. Work supported by: the United States Department of Energy under DOE Contracts DE-AC05-06OR23177 and DE-AC02-76SF00515; National Natural Science Foundation of China, under grant no. 11805097; Jiangsu Province Natural Science Foundation, under grant no. BK20180323; Jiangsu Province *Hundred Talents Plan for Professionals*; the Spanish Ministerio de Economía, Industria y Competitividad under contract No. FPA2017-86380-P and the Junta de Andalucía under contract No. UHU-1264517; the UK Science and Technology Facilities Council (STFC); and the European Research Council (ERC) under the European Union's Horizon 2020 Research and Innovation Rrogram (grant no. 647981, 3DSPIN).

[1] M. Tanabashi *et al.* [Particle Data Group], Phys. Rev. D **98**, 03001 (2018).
[2] V.D. Burkert and C.D. Roberts, Rev. Mod. Phys. **91**, 011003 (2019).
[3] T. Horn and C.D. Roberts, J. Phys. G. **43**, 073001 (2016).
[4] I.G. Aznauryan and V.D. Burkert, Prog. Part. Nucl. Phys. **67**, 1 (2012).
[5] V.I. Mokeev [CLAS Collaboration], Few Body Syst. **59**, 46 (2018).
[6] V.I. Mokeev, arXiv:1909.08746 [nucl-ex], (2019).
[7] A. Accardi *it al.*, Eur. Phys. J. A **52**, 268 (2016).
[8] A.C. Aguilar *et al.*, Eur. Phys. J. A **55**, 190 (2019).
[9] A. Bacchetta *et al.*, JHEP **06**, 81 (2017).
[10] R, Dupre, Eur. Phys. J. A **53**, 171 (2017).
[11] V.D. Burkert, L. Elouadrhiri, and F.-X. Girod, Nature **557**, no. 7705, 396 (2018).
[12] K.D. Launey, T. Dytrych, and J.P. Draayer, Prog. Part. Nucl. Phys. **89**, 101 (2016).
[13] J. Draayer, private communication
[14] A.V. Anisovich *et al.*, Phys. Rev. Lett. **119**, 062004 (2017).
[15] V.I. Mokeev *et al.*, Phys. Lett. B **805**, 135457 (2020).
[16] J. Segovia, I.C. Cloet, C.D. Roberts, and S.M. Schmidt, Few Body Syst. **55**, 1185 (2014).
[17] A.V. Radyushkin, Phys. Rev. D **96**, 034025 (2017).
[18] A.J. Chambers *et al.*, Phys. Rev. Lett. **118**, 242001 (2017).
[19] Yan-Qing Ma and Jian-Wei Qiu, Phys. Rev. D **98**, 074021 (2018).
[20] J. Segovia, B. El-Bennich, E. Rojas, I.C. Cloet, C.D. Roberts, S.-S. Xu, and H.-S. Zong, Phys. Rev. Lett. **115**, 171801 (2015).
[21] V.I. Mokeev *et al.*, Phys. Rev. C **93**, 025206 (2016).
[22] S.K. Choi *et al.*, Phys. Rev. Lett. **91**, 262001 (2003).
[23] S. Olsen *et al.*, EPJ Web of Conferences **202**, 01003 (2019).
[24] N. Brambilla *et al.*, arXiv:1907.07583 (2019).
[25] R.L. Jaffe, Phys. Rev. D **15**, 267 (1977).
[26] C. Adolph *et al.*, Phys. Rev. Lett. **115**, 082001 (2015).
[27] J. Dudek, Phys. Rev. D **84**, 074023 (2011).
[28] C.A. Meyer, E.S. Swanson, E.S., Prog. Part. Nucl. Phys. **82**, 21 (2015).
[29] B. Ketzer, B. Grube, and D. Ryabchikov, Progress in Particle and Nuclear Physics, 103755 (2020).
[30] S. Chandavar *et al.*, Phys. Rev. C **97**, 025203 (2017).
[31] H. Al Ghoul *et al.*, Phys. Rev. C **95**, 042201 (2017).
[32] S. Adhikari *et al.*, Phys. Rev. C **100**, 052201 (2019).
[33] A. Ali *et al.*, Phys. Rev. Lett. **123**, 072001 (2019).
[34] V.D. Burkert *et al.*, Nucl. Instrum. Methods A **959**, 163419 (2020).
[35] A. Acker *et al.*, Nucl. Instrum. Methods A **959**, 163475 (2020).
[36] V.D. Burkert, arXiv:1912.11400 [nucl-ex].
[37] J. Segovia *et al.*, Phys. Lett. B **662**, 33 (2008).
[38] K. Nakamura *et al.* [Particle Data Group], J. Phys. G, Nucl. Part. Phys. **37**, 075021 (2010).
[39] Z.P. Li, V. Burkert, and Z.J. Li, Phys. Rev. D **46**, 70 (1992).
[40] I.G. Aznauryan and V.D. Burkert, *Proceedings, 11th International Workshop on the Physics of Excited Nucleons (NSTAR 2017): Columbia, SC, USA, August 20-23, 2017*, Few Body Syst. **59**, 98 (2018).
[41] I.G. Aznauryan and V. Burkert, Phys. Rev. C **95**, no.

6, 065207 (2017).
[42] I.V. Anikin, V.M. Braun, and N. Offen, Phys. Rev. D **92**, no. 1, 014018 (2015).
[43] V.D. Burkert, Ann. Rev. Nucl. Part. Sci. **68**, 405 (2018).
[44] S. Chatterjee, D. Mishra, B. Mohanty, and S. Samanta, Phys. Rev. C **96**, no. 5, 054907 (2017).
[45] A. Bazavov *et al.*, Phys. Rev. Lett. **113**, no. 7, 072001 (2014).
[46] C.D. Roberts, J. Phys. Conf. Ser. **706**, 022003 (2016).
[47] D. Binosi, L. Chang, S.-X. Qin, J. Papavassiliou, and C.D. Roberts, Phys. Rev. D **93**, 096010 (2016).
[48] G. Eichmann, H. Sanchis-Alepuz, R. Williams, R. Alkofer, and C.S. Fischer, Prog. Part. Nucl. Phys. **91**, 1 (2016).
[49] C.S. Fischer, Prog. Part. Nucl. Phys. **105**, 1 (2019).
[50] D. Binosi, L. Chang, J. Papavassiliou, and C.D. Roberts, Phys. Lett. B **742**, 183 (2015).
[51] D. Binosi, C. Mezrag, J. Papavassiliou, C.D. Roberts, and J. Rodríguez-Quintero, Phys. Rev. D **96**, 054026 (2017).
[52] J. Rodríguez-Quintero, D. Binosi, C. Mezrag, J. Papavassiliou, and C.D. Roberts, Few Body Syst. **59**, 121 (2018).
[53] Z.-F. Cui *et al.*, arXiv:1912.08232 [hep-ph].
[54] A.C. Aguilar, D. Binosi, and J. Papavassiliou, Front. Phys. China **11**, 111203 (2016).
[55] A. Deur, V. Burkert, J.-P. Chen, and W. Korsch, Phys. Lett. B **650**, 244 (2007).
[56] A. Deur, V. Burkert, J.-P. Chen, and W. Korsch, Phys. Lett. B **665**, 349 (2008).
[57] A. Deur, S.J. Brodsky, and G.F. de Téramond, Prog. Part. Nucl. Phys. **90**, 1 (2016).
[58] Y.L. Dokshitzer, Sov. Phys. JETP **46**, 641 (1977).
[59] V.N. Gribov and L.N. Lipatov, Sov. J. Nucl. Phys. **15**, 438 (1972).
[60] L.N. Lipatov, Sov. J. Nucl. Phys. **20**, 94 (1975).
[61] G. Altarelli and G. Parisi, Nucl. Phys. B **126**, 298 (1977).
[62] M. Ding *et al.*, arXiv:1905.05208 [nucl-th] (2019).
[63] M. Ding *et al.*, Chin. Phys. C in press, arXiv:1912.07529 [hep-ph] (2020).
[64] J. Rodríguez-Quintero, L. Chang, K. Raya, and C.D. Roberts, arXiv:1909.13802 [nucl-th], in 27th International Nuclear Physics Conference (INPC 2019) Glasgow, Scotland, July 29-August 2, 2019, 2019.
[65] Y.L. Dokshitzer, hep-ph/9812252, in High-energy physics. Proceedings, 29th International Conference, ICHEP'98, Vancouver, Canada, July 23-29, 1998. Vol. 1, 2, pp. 305–324, 1998.
[66] Y. Nambu, Phys. Rev. **117**, 648 (1960).
[67] J. Goldstone, Nuovo Cim. **19**, 154 (1961).
[68] C.D. Roberts, in *27th International Nuclear Physics Conference (INPC 2019)*, Glasgow, Scotland, United Kingdom, July 29-August 2, 2019.
[69] G.P. Lepage and S.J. Brodsky, Phys. Lett. B **87**, 359 (1979).
[70] A.V. Efremov and A.V. Radyushkin, Phys. Lett. B **94**, 245 (1980).
[71] G.P. Lepage and S.J. Brodsky, Phys. Rev. D **22**, 2157 (1980).
[72] L. Chang, I.C. Cloët, C.D. Roberts, S.M. Schmidt, and P.C. Tandy, Phys. Rev. Lett. **111**, 141802 (2013).
[73] F. Gao, L. Chang, Y.-X. Liu, C.D. Roberts, and P.C. Tandy, Phys. Rev. D **96**, 034024 (2017).
[74] M. Chen, M. Ding, L. Chang, and C.D. Roberts, Phys. Rev. D **98**, 091505(R) (2018).
[75] J.D. Sullivan, Phys. Rev. D **5**, 1732 (1972).
[76] S.-X. Qin, C. Chen, C. Mezrag, and C.D. Roberts, Phys. Rev. C **97**, 015203 (2018).
[77] T. Horn *et al.*, Scaling Study of the L/T-Separated Pion Electroproduction Cross Section at 11 GeV, approved Jefferson Lab 12 GeV Experiment E12-07-105, 2007.
[78] M. Carmignotto *et al.*, Phys. Rev. C **97**, 025204 (2018).
[79] G. Huber *et al.*, Phys. Rev. C **78**, 045203 (2008).
[80] T. Horn *et al.*, Phys. Rev. Lett. **97**, 192001 (2006).
[81] T. Horn *et al.*, Phys. Rev. C **78**, 058201 (2008).
[82] T. Horn *et al.*, Studies of the L/T Separated Kaon Electroproduction Cross Section from 5-11 GeV, Approved Jefferson Lab 12 GeV Experiment, 2009.
[83] T. Horn *et al.*, Study of the L–T Separated Pion Electroproduction Cross Section at 11 GeV and Measurement of the Charged Pion Form Factor to High Q^2, approved Jefferson Lab experiment E12-19-006, 2019.
[84] X. Cao *et al.*, Nuclear Science and Technology – in press (2020), Electron Ion Collider in China (EicC).
[85] Z.F. Ezawa, Nuovo Cim. A **23**, 271 (1974).
[86] G.R. Farrar and D.R. Jackson, Phys. Rev. Lett. **35**, 1416 (1975).
[87] E.L. Berger and S.J. Brodsky, Phys. Rev. Lett. **42**, 940 (1979).
[88] J. Badier *et al.*, Phys. Lett. B **93**, 354 (1980).
[89] J. Badier *et al.*, Z. Phys. C **18**, 281 (1983).
[90] B. Betev *et al.*, Z. Phys. C **28**, 15 (1985).
[91] S. Falciano *et al.*, Z. Phys. C **31**, 513 (1986).
[92] M. Guanziroli *et al.*, Z. Phys. C **37**, 545 (1988).
[93] J.S. Conway *et al.*, Phys. Rev. D **39**, 92 (1989).
[94] R.J. Holt and C.D. Roberts, Rev. Mod. Phys. **82**, 2991 (2010).
[95] M.B. Hecht, C.D. Roberts, and S.M. Schmidt, Phys. Rev. C **63**, 025213 (2001).
[96] K. Wijesooriya, P.E. Reimer, and R.J. Holt, Phys. Rev. C **72**, 065203 (2005).
[97] M. Aicher, A. Schäfer, and W. Vogelsang, Phys. Rev. Lett. **105**, 252003 (2010).
[98] K.-F. Liu and S.-J. Dong, Phys. Rev. Lett. **72**, 1790 (1994).
[99] X. Ji, Phys. Rev. Lett. **110**, 262002 (2013).
[100] A.V. Radyushkin, Phys. Lett. B **767**, 314 (2017).
[101] J.-H. Zhang *et al.*, Phys. Rev. D **100**, 034505 (2019).
[102] N. Karthik *et al.*, PoS **LATTICE2018**, 109 (2018).
[103] J. Karpie, K. Orginos, A. Rothkopf, and S. Zafeiropoulos, JHEP **04**, 057 (2019).
[104] R.S. Sufian *et al.*, Phys. Rev. D **99**, 074507 (2019).
[105] B. Joó *et al.*, Phys. Rev. D **100**, 114512 (2019).
[106] R.S. Sufian *et al.*, Pion Valence Quark Distribution at Large x from Lattice QCD – arXiv:2001.04960 [hep-lat], (2020).
[107] D. Adikaram *et al.*, Measurement of Tagged Deep Inelastic Scattering (TDIS), approved Jefferson Lab experiment E12-15-006.
[108] D. Adikaram *et al.*, Measurement of Kaon Structure Function through Tagged Deep Inelastic Scattering (TDIS), approved Jefferson Lab experiment C12-15-006A.
[109] O. Denisov *et al.*, arXiv:1808.00848 [hep-ex] Letter of Intent (Draft 2.0): A New QCD facility at the M2 beam line of the CERN SPS.
[110] F.-X. Girod, M. Guidal, T. Horn, and C. Munoz-

Camacho, The Multi-Hall Deep Exclusive Scattering Program at 12 GeV, Pion L-T (E12-07-105/E12-06-101) – Complementarity document submitted to PAC40 in 2013, 2019.
[111] B. Berthou *et al.*, Eur. Phys. J. C **78**, 478 (2018).
[112] C. Mezrag *et al.*, Phys. Lett. B **741**, 190 (2015).
[113] C. Mezrag, H. Moutarde, and J. Rodríguez-Quintero, Few Body Syst. **57**, 729 (2016).
[114] N. Chouika, C. Mezrag, H. Moutarde, and J. Rodríguez-Quintero, Phys. Lett. B **780**, 287 (2018).
[115] S.-S. Xu, L. Chang, C.D. Roberts, and H.-S. Zong, Phys. Rev. D **97**, 094014 (2018).
[116] P. Jimenez-Delgado, W. Melnitchouk, and J.F. Owens, J. Phys. G: Nucl. Part. Phys. **40**, 093102 (2013).
[117] J. Blümlein, Prog. Part. Nucl. Phys. **69**, 28 (2013).
[118] S. Forte and G. Watt, Ann. Rev. of Nucl. Part. Sci. **63**, (2013).
[119] Jefferson Lab Angular Momentum (JAM) Collaboration, `http://www.jlab.org/jam`.
[120] N. Sato, W. Melnitchouk, S.E. Kuhn, J.J. Ethier, and A. Accardi, Phys. Rev. D **93**, 074005 (2016).
[121] N. Sato, J.J. Ethier, W. Melnitchouk, M. Hirai, S. Kumano, and A. Accardi, Phys. Rev. D **94**, 114004 (2016).
[122] J.J. Ethier, N. Sato, and W. Melnitchouk, Phys. Rev. Lett. **119**, 132001 (2017).
[123] N. Sato, C. Andres, J.J. Ethier, and W. Melnitchouk, arXiv:1905.03788 [hep-ph], to appear in Phys. Rev. D (2020).
[124] P.C. Barry, N. Sato, W. Melnitchouk, and C.R. Ji, Phys. Rev. Lett. **121**, 152001 (2018).
[125] W. Melnitchouk and A. W. Thomas, Phys. Lett. B **377**, 11 (1996).
[126] A. Accardi, L.T. Brady, W. Melnitchouk, J. F. Owens, and N. Sato, Phys. Rev. D **93**, 114017 (2016).
[127] S. Tkachenko *et al.*, Phys. Rev. C **89**, 045206 (2014).
[128] I.R. Afnan *et al.*, Phys. Rev. C **68**, 035201 (2003).
[129] T.J. Hobbs and W. Melnitchouk, Phys. Rev. D **77**, 114023 (2008).
[130] The SoLID (Solenoidal Large Intensity Device) Updated Preliminary Conceptual Design Report, [SoLID Collaboration], 2019.
[131] N. Kalantarians, C. Keppel, and M.E. Christy, Phys. Rev. C **96**, 032201 (2017).
[132] A. Accardi, F. Arleo, W.K. Brooks, D. D'Enterria, and V. Muccifora, Riv. Nuovo Cim. **32**, 439 (2010).
[133] A. Majumder and M. Van Leeuwen, Prog. Part. Nucl. Phys. A **66**, 41 (2011).
[134] M. Aaboud *et al.*, Eur. Phys. J. C **78**, 110 (2018).
[135] E.C. Aschenauer, I. Borsa, R. Sassot, and C. Van Hulse, Phys. Rev. D **99**, 094004 (2019).
[136] G. Aad *et al.*, JHEP 05 (2014) 068.
[137] C.A. Aidala, S.D. Bass, D. Hasch, and G.K. Mallot, Rev. Mod. Phys. **85**, 655 (2013).
[138] M. Anselmino, P. Gambino, and J. Kalinowski, Z. Phys. C **64**, 267 (1994).
[139] B. Joo, J. Karpie, K. Orginos, A. Radyushkin, D. Richards, and S. Zafeiropoulos, JHEP **1912**, 081 (2019).
[140] C. Alexandrou, K. Cichy, M. Constantinou, K. Hadjiyiannakou, K. Jansen, A. Scapellato, and F. Steffens, Phys. Rev. D **99**, 114504 (2019).
[141] J. Bringewatt, M. Constantinou, W. Melnitchouk, J. Qiu, N. Sato, and F. Steffens, *Combined QCD analysis of PDFs and lattice data*, in preparation (2020).
[142] J. Segovia, C. Chen, Z.F. Cui, Y. Lu, and C.D. Roberts, in *15th International Conference on Meson-Nucleon Physics and the Structure of the Nucleon (MENU 2019)*, Pittsburgh, PA, Jun. 2-7, 2019
[143] C.D. Roberts, *Proceedings, 11th International Workshop on the Physics of Excited Nucleons (NSTAR 2017): Columbia, SC, USA, August 20-23, 2017*, Few Body Syst. **59**, 72 (2018).
[144] Z.-F. Cui, C. Chen, D. Binosi, F. de Soto, C.D. Roberts, 2003.11655 [hep-ph], (2020).
[145] Y. Lu *et al.*, Phys. Rev. D **100**, 034001 (2019).
[146] C. Chen *et al.*, Phys. Rev. D **99**, 034013 (2019).
[147] J. Segovia and C.D. Roberts, Phys. Rev. C **94**, 042201(R) (2016).
[148] V.D. Burkert, *Proceedings, 11th International Workshop on the Physics of Excited Nucleons (NSTAR 2017): Columbia, SC, USA, August 20-23, 2017*, Few Body Sys. **59**, 57 (2018).
[149] I.G. Aznauryan and V.D. Burkert, Phys. Rev. C **85**, 055202 (2012).
[150] M.M. Giannini and E. Santopinto, Chin. J. Phys. **53**, 020301 (2015).
[151] G. Ramalho, *Proceedings, 11th International Workshop on the Physics of Excited Nucleons (NSTAR 2017): Columbia, SC, USA, August 20-23, 2017*, Few Body Syst. **58**, 92 (2018).
[152] M. Ronniger and B.C. Metcsh, Eur. Phys. J. **A49**, 8 (2013).
[153] D. Binosi, L. Chang, J. Papavassiliou, J. Papavassiliou, S.-X. Qin, and C.D. Roberts, Phys. Rev. D **95**, 031501 (2017).
[154] I.G. Aznauryan *et al.*, Int. J. Mod. Phys. E **22**, 1330015 (2013).
[155] CLAS Physics Database, `http://clasweb.jlab.org/physicsdb`.
[156] I.G. Aznauryan *et al.* [CLAS Collaboration], Phys. Rev. C **80**, 055203 (2009).
[157] K. Park *et al.* [CLAS Collaboration], Phys. Rev. C **91**, 045203 (2015).
[158] H. Denizli *et al.* [CLAS Collaboration], Phys. Rev. C **76**, 015204 (2007).
[159] V.I. Mokeev *et al.* [CLAS Collaboration], Phys. Rev. C **86**, 035203 (2007).
[160] A.N. Hiller Blin *et al.*, Phys. Rev. C **100**, 035201 (2019).
[161] V.I. Mokeev, V.D. Burkert, T.-S. H. Lee, L. Elouadrhiri, G.V. Fedotov, and B.S. Ishkanov, Phys. Rev. C **80**, 045212 (2009).
[162] E. Golovatch *et al.* [CLAS Collaboration], Phys. Lett. B **788**, 371 (2019).
[163] A.V. Radyushkin, arXiv:1912.04244 [hep-ph], (2019).
[164] J.-W. Qiu, *Proceedings, 8th International Conference on Quarks and Nuclear Physics (QNP2018): Tsukuba, Japan, November 13-17, 2018*, JPS Conf. Proc. **26**, 011010 (2019).
[165] J. Segovia, C. Chen, C.D. Roberts, and S. Wan, Phys. Rev. C **88**, 032201 (2013).
[166] I.T. Obukhovsky, A. Faessler, D.K. Fedorov, T. Gutsche, and V.E. Lyubovitskij, Phys. Rev. D **100**, 094013 (2019)
[167] D. Rönchen, M. Döring, H. Haberzettl, J. Haidenbauer, U.G. Meissner, and K. Nakayama, Eur. Phys. J. A **51**, 70 (2015).
[168] H. Kamano, *Proceedings, 11th International Workshop on the Physics of Excited Nucleons (NSTAR 2017): Columbia, SC, USA, August 20-23, 2017*, Few Body

Syst. **59**, 24 (2018).
[169] T. Gutsche, V.E. Lyubovitskij, and I. Schmidt, arXiv:1911.00076 [hep-ph], (2019).
[170] T. Gutsche, V.E. Lyubovitskij, and I. Schmidt, arXiv:1906.08641 [hep-ph], (2019).
[171] C.D. Roberts *12th International Workshop on the Physics of Excited Nucleons (NSTAR 2019) Bonn, Germany, June 10-14, 2019*, arXiv:1909.11102 [nucl-th], (2019).
[172] C.D. Roberts, private communication
[173] M. Burkardt, Int. J. Mod. Phys. A **18**, 173 (2003).
[174] A.V. Belitsky, X.D. Ji, and F. Yuan, Phys. Rev. D **69**, 074014 (2004).
[175] A.V. Belitsky, D. Mueller, and A. Kirchner, Nucl. Phys. B **629**, 323 (2002).
[176] X.D. Ji, Phys. Rev. D **55**, 7114 (1997).
[177] F.-X. Girod *et al.* [CLAS Collaboration], Phys. Rev. Lett. **100**, 162002 (2008).
[178] H.S. Jo *et al.* [CLAS Collaboration], Phys. Rev. Lett. **115**, no. 21, 212003 (2015).
[179] C.M. Camacho *et al.* [Jefferson Lab Hall A and Hall A DVCS Collaborations], Phys. Rev. Lett. **97**, 262002 (2006).
[180] S. Chen *et al.* [CLAS Collaboration], Phys. Rev. Lett. **97**, 072002 (2006).
[181] S. Pisano *et al.* [CLAS Collaboration], Phys. Rev. D **91**, no. 5, 052014 (2015).
[182] E. Seder *et al.* [CLAS Collaboration], Phys. Rev. Lett. **114**, no. 3, 032001 (2015); Addendum: [Phys. Rev. Lett. **114**, no. 8, 089901 (2015)].
[183] S. Stepanyan *et al.* [CLAS Collaboration], Phys. Rev. Lett. **87**, 182002 (2001).
[184] A. Airapetian *et al.* [HERMES Collaboration], Phys. Rev. Lett. **87**, 182001 (2001).
[185] JLab Experiment E12-11-003, `https://www.jlab.org/exp\_prog/proposals/proposal\_updates/E12-11-003\_Update\_pac38.pdf`
[186] R. Dupré, M. Guidal, S. Niccolai, and M. Vanderhaeghen, Eur. Phys. J. A **53**, no.8, 171 (2017).
[187] F.-X. Girod, private communication.
[188] P. Hagler *et al.* [LHPC Collaboration], Phys. Rev. D **77**, 094502 (2008).
[189] J. Bratt *et al.* [LHPC Collaboration], Phys. Rev. D **82**, 094502 (2010).
[190] C. Alexandrou *et al.*, Phys. Rev. D **101**, no.3, 034519 (2020).
[191] G.S. Bali, S. Collins, M. Gøckeler, R. Rødl, A.Schäfer, and A. Sternbeck, Phys. Rev. D **100**, no.1, 014507 (2019).
[192] A.V. Radyushkin, Phys. Rev. D **100**, no.11, 116011 (2019).
[193] M. Diehl, Phys. Rept. **388**, 41 (2003).
[194] I. Bedlinskiy *et al.* [CLAS Collaboration], Phys. Rev. Lett. **109**, 112001 (2012).
[195] I. Bedlinskiy *et al.* [CLAS Collaboration], Phys. Rev. C **90**, 025205 (2014).
[196] I. Bedlinskiy *et al.* [CLAS Collaboration], Phys. Rev. C **95**, 035202 (2017).
[197] M. Defurne *et al.* [Jefferson Lab Hall A], Phys. Rev. Lett. **117**, 262001 (2016).
[198] M. Mazouz *et al.* [Jefferson Lab Hall A], Phys. Rev. Lett. **118**, 222002 (2017).
[199] M. Alexeev *et al.* [COMPASS Collaboration], Phys. Lett. B **805**, 135454 (2020).
[200] S. Goloskokov and P. Kroll,, Eur. Phys. J. C **65**, 137 (2010).
[201] S. Goloskokov and P. Kroll, Eur. Phys. J. A **47**, 112 (2011).
[202] S. Ahmad, G. R. Goldstein, and S. Liuti, Phys. Rev. D **79**, 054014 (2009).
[203] G.R. Goldstein, J. Hernandez, and S. Liuti, Phys. Rev. D **84**, 034007 (2011).
[204] P. Schweitzer and C. Weiss, Phys. Rev. C **94**, 045202 (2016).
[205] V. Kubarovsky, Int. J. Mod. Phys. Conf. Ser. **40**, 1660051 (2016).
[206] V. Kubarovsky, PoS SPIN2018, 075 (2019).
[207] A. Radyushkin, Phys. Lett. B **449**, 81 (1999).
[208] M. Diehl and P. Hagler, Eur. Phys. J. C **44**, 87 (2005).
[209] M. Diehl and P. Kroll, Eur. Phys. J. C **73**, 2397 (2013).
[210] X. Ji, J.P. Ma, and F. Yuan, Phys. Rev. D **71**, 034005 (2005).
[211] S.M. Aybat and T.C. Rogers, Phys. Rev. D **83**, 114042 (2011).
[212] John Collins, Foundations of Perturbative QCD, Cambridge Monographs on Particle Physics, Nuclear Physics and Cosmology, Cambridge University Press, (2011). `http://books.google.it/books?id=0xGi1KW9vykC`.
[213] M.G. Echevarria, A. Idilbi, A. Schaefer, and I. Scimeni, Eur. Phys. J C **73**, 2636 (2013).
[214] P.J. Mulders and R.D. Tangerman, Nucl. Phys. B **461**, 197 (1996).
[215] D. Boer and P.J. Mulders, Phys. Rev. D **57**, 5780 (1998).
[216] A. Bacchetta *et al.*, Phys. Lett. **B797**, 134850 (2019).
[217] T.C. Rogers and P.J. Mulders, Phys. Rev. D **81**, 094006 (2010).
[218] Z.B. Kang, X. Liu, F. Finger, and H. Xing, JHEP **11**, 68 (2017).
[219] J.C. Collins, D.E. Soper, and G. Sterman, Nucl. Phys. B **250**, 199 (1985).
[220] A. Bacchetta *et al.*, arXiv:1912.07550, (2019).
[221] I. Scimemi and A. Vladimirov, arXiv:1912.06532, (2019).
[222] E. Laenen, G.F. Sterman, W. Vogelsang, Phys. Rev. Lett. **84**, 4296 (2000).
[223] G. Bozzi, S. Catani, D. de Florian, and M. Grazzini, Nucl. Phys. B **737**, 73 (2006).
[224] R. Angeles-Martinez *et al.*, Acta Phys. Polon. **B46**, 2501 (2015).
[225] J. Collins *et al.*, Phys. Rev. D **94**, 034014 (2016).
[226] L. Gamberg, A. Metz, D. Pitonyak, and A. Prokudin, Phys. Lett. B **781**, 443 (2018).
[227] M.G. Echevarria *et al.*, Phys. Lett. B **781**, 161 (2018).
[228] A. Signori, A. Bacchetta, M. Radici, and G. Schnell, JHEP **1311**, 194 (2013).
[229] A. Bacchetta *et al.*, Phys. Lett. B **788**, 542 (2019).
[230] J.O. Gonzalez-Hernandez, T.C. Rogers, N. Sato, and B. Wang, Phys. Rev. D **98**, 114005 (2018).
[231] M. Boglione *et al.*, JHEP **10**, 122 (2019).
[232] V. Bertone, I. Scimemi, and A. Vladimirov, JHEP **6**, 28 (2019).
[233] W.J. den Dunnen, J.P. Lansberg, C. Pisano, and M. Schlegel, Phys. Rev. Lett. **112**, 212001 (2014).
[234] D. Boer, P.J. Mulders, C. Pisano, and J. Zhou, JHEP **8**, 1 (2016).
[235] U. D'Alesio, F. Murgia, C. Pisano, and P. Taels, Phys. Rev. D **96**, 036001 (2017).

[236] U. D'Alesio, F. Murgian, C. Pisano, and S. Rajesh, Eur. Phys. J C **79**, 1029 (2019).
[237] A. Mukherjee and S. Rajesh, Eur. Phys. J. C **77**, 854 (2017).
[238] S. Rajesh, R. Kishore, and A. Mukherjee, Phys. Rev. D **98**, 014007 (2018).
[239] A. Bacchetta, D. Boer, C. Pisano, and P. Taels, Eur. Phys. J. C **80**, 72 (2020).
[240] Dennis W. Sivers, Phys. Rev. D **41**, 83 (1990).
[241] John C. Collins, Phys. Lett. B **536**, 43 (2002).
[242] L. Adamczyk *et al.*, Phys. Rev. Lett. **116**, 132301 (2016).
[243] M. Aghasyan *et al.*, Phys. Rev. Lett. **119**, 112002 (2017).
[244] M. Anselmino *et al.*, JHEP **4**, 46 (2017).
[245] W. Vogelsang and F. Yuan, Phys. Rev. D **72**, 054028 (2005).
[246] J.C. Collins *et al.*, Phys. Rev. D **73**, 014021 (2006).
[247] A. Bacchetta and M. Radici, Phys. Rev. Lett. **107**, 212001 (2011).
[248] M. Anselmino, M Boglione, and S. Melis, Phys. Rev. D **86**, 014028 (2012).
[249] S. Mert Aybat, A. Prokudin, and T.C. Rogers, Phys. Rev. Lett. **108**, 242003 (2012).
[250] P. Sun and F. Yuan, Phys. Rev. D **88**, 114012 (2013).
[251] Daniel Boer, Nucl. Phys. **B874**, 217 (2013).
[252] M.G. Echevarria, A. Idilbi, Z.B. Kang, and I. Vitev, Phys. Rev. D **89**, 074013 (2014).
[253] M. Boglione, U. D'Alesio, C. Flore, and J.O. Gonzalez-Hernandez, JHEP **7**, 148 (2018).
[254] A. Bacchetta, F. Delcarro, C. Pisano, and M. Radici, arXiv:2004.14278 [hep-ph], (2020).
[255] J.P. Chen, H. Gao, T.K. Hemmick, Z.E. Meziani, and P.A. Souder, "A White Paper on SoLID", arXiv:1409.7741, (2014)
[256] JLab E12-10-006, J.P. Chen, H. Gao, X. Jiang, and X. Qian, "Target Single Spin Asymmetry in Semi-Inclusive Deep-Inelastic $(e, e'\pi^{\pm})$ Reactions on a Transversely Polarized ^{3}He Target at 11 GeV", (2010).
[257] JLab E12-11-108, K. Allada, J.P. Chen, H. Gao, and Z.E. Meziani, "Target Single Spin Asymmetry in Semi-Inclusive Deep-Inelastic $(e, e', \pi^{\pm})$ Reactions on a Transversely Polarized Proton Target", (2011).
[258] R.L. Jaffe and X. Ji, Phys. Rev. Lett. **67**, 552 (1991).
[259] M. Anselmino *et al.*, Phys. Rev. D **87**, 094019 (2013).
[260] Z.B. Kang, A. Prokudin, P. Sun, and F. Yuan, Phys. Rev. D **93**, 014009 (2016).
[261] H.W. Lin *et al.*, Phys. Rev. Lett. **120**, 152502 (2018).
[262] L. Adamczyk *et al.*, Phys. Lett. **B780**, 332 (2018).
[263] Z.B. Kang, A. Prokudin, F. Ringer, and F. Yuan, Phys. Lett **B774**, 635 (2017).
[264] R.L. Jaffe, X. Jin, and J. Tang, Phys. Rev. Lett. **80**, 1166 (1998).
[265] A. Bianconi, S. Boffi, R. Jakob, and M. Radici, Phys. Rev. D **62**, 034008 (2000).
[266] M. Radici, R. Jakob, and A. Bianconi, Phys. Rev. D **65**, 074301 (2002).
[267] A. Bacchetta and M. Radici, Phys. Rev. D **67**, 094002 (2003).
[268] A. Bacchetta and M. Radici, Phys. Rev. D **70**, 094032 (2004).
[269] D. Boer, R. Jakob, and M. Radici, Phys. Rev. D **67**, 094003 (2003).
[270] A. Bacchetta, F.A. Ceccopieri, A. Mukherjee, and M. Radici, Phys. Rev. D **79**, 034029 (2009).
[271] A. Courtoy, A. Bacchetta, M. Radici, and A. Bianconi, Phys. Rev. D **85**, 114023 (2012).
[272] H.H. Matevosyan *et al.*, Phys. Rev. D **97**, 074019 (2018).
[273] A. Bacchetta, A. Courtoy, and M. Radici, Phys. Rev. Lett. **107**, 012001 (2011).
[274] A. Bacchetta, A. Courtoy, and M. Radici, JHEP **1303**, 119 (2013).
[275] M. Radici, A. Courtoy, A. Bacchetta, and M. Guagnelli, JHEP **05**, 123 (2015).
[276] M. Radici and A. Bacchetta, Phys. Rev. Lett. **120**, 192001 (2018).
[277] Z. Ye *et al.*, Phys. Lett. B **767**, 91 (2017).
[278] D. Dubbers and M.G. Schmidt, Rev. Mod. Phys. **83**, 1111 (2011).
[279] N. Yamanaka *et al.*, Eur. Phys. J. **A53**, 54 (2017).
[280] T. Liu, Z. Zhao, and H. Gao, Phys. Rev. D **97**, 074018 (2018).
[281] A. Airapetian *et al.*, Phys. Rev. Lett. **94**, 012002 (2005).
[282] A. Airapetian *et al.*, Phys. Rev. Lett. **103**, 152002 (2009).
[283] C. Adolph *et al.*, Phys. Lett. **B717**, 376 (2012).
[284] C. Adolph *et al.*, Phys. Lett **B717**, 383 (2012).
[285] B. Parsamyan, Phys. Part. Nucl. **45**, 158 (2014).
[286] X. Qian *et al.*, Phys. Rev. Lett. **107**, 072003 (2011).
[287] J. Huang *et al.*, Phys. Rev. Lett. **108**, 052001 (2012).
[288] Y. Zhang *et al.*, Phys. Rev. C **90**, 055209 (2014).
[289] JLab E12-11-007, J.P. Chen, J. Huang, and Y. Qiang, "Asymmetries in Semi-Inclusive Deep-Inelastic $(e, e', \pi^{\pm})$ Reactions on a Longitudinally Polarized ^{3}He Target at 8.8 and 11 GeV", (2011).
[290] R. Gupta *et al.*, Phys. Rev. D **98**, 091501 (2018).
[291] C. Alexandrou *et al.*, arXiv:1909.00485, (2019).
[292] N. Yamanaka, S. Hashimoto, T. Kaneko, and H. Ohki, arXiv:1805.10507 [hep-lat].
[293] C. Alexandrou *et al.*, Phys. Rev. D **95**, 114514 (2017); erratum: Phys. Rev. D **96**, 099906 (2017).
[294] J. Cammarota *et al.*, arXiv:2002.08384 [hep-ph], (2020).
[295] I.Y. Kobzarev and L.B. Okun, Zh. Eksp. Teor. Fiz. **43**, 1904 (1962); [Sov. Phys. JETP **16**, 1343 (1963)].
[296] H. Pagels, Phys. Rev. **144**, 1250 (1966).
[297] D. Müller, D. Robaschik, D. Geyer, F.M. Dittes, and J. Hořejši, Fortsch. Phys. **42**, 101 (1994).
[298] X.D. Ji, Phys. Rev. Lett. **78**, 610 (1997).
[299] A.V. Radyushkin, Phys. Lett. B **380**, 417 (1996).
[300] M.V. Polyakov, Phys. Lett. B **555**, 57 (2003).
[301] P.P. Avelino, Phys. Lett. B **795**, 627 (2019).
[302] A. Rajan, T. Gorda, S. Liuti, and K. Yagi, arXiv:1812.01479 [hep-ph].
[303] P.E. Shanahan and W. Detmold, Phys. Rev. Lett. **122**, no. 7, 072003 (2019).
[304] S.M. Troshin and N.E. Tyurin, Mod. Phys. Lett. A **34**, no. 32, 1950259 (2019).
[305] I.M. Dremin, Particles **2**, no. 1, 57 (2019).
[306] I.M. Dremin, Eur. Phys. J. C **80**, no. 2, 172 (2020).
[307] S.D. Campos, Int. J. Mod. Phys. A **34**, no. 10, 1950057 (2019).
[308] I.V. Anikin, J. Phys. Conf. Ser. **1435**, no. 1, 012002 (2020).
[309] I.V. Anikin, Phys. Rev. D **99**, no. 9, 094026 (2019).
[310] M.V. Polyakov and P. Schweitzer, Int. J. Mod. Phys. A **33**, no. 26, 1830025 (2018).
[311] C. Lorcé, H. Moutarde, and A.P. Trawinski, Eur. Phys.

J. C **79**, no. 1, 89 (2019).
[312] L. Elouadrhiri, J. Grames, W. Melnitchouk, T.A. Forest, and E. Voutier, "Positrons at Jefferson Lab", Proceedings International Workshop, (JPOS09), Newport News, USA, March 25-27, 2009, AIP Conf. Proc. **1160** (2009).
[313] Proceedings, International Workshop on Physics with Positrons at Jefferson Lab (JPOS17) : Newport News, VA, USA, September 12-15, 2017, AIP Conf. Proc. **1970**, no. 1 (2018).
[314] J. Segovia, C.D. Roberts, and S.M. Schmidt, Phys. Lett. B **750**, 100 (2015).
[315] A. Bender, C.D. Roberts, and L. von Smekal, Phys. Lett. B **380**, 7 (1996).
[316] M.S. Bhagwat, A. Höll, A. Krassnigg, C.D. Roberts, and P.C. Tandy, Phys. Rev. C **70**, 035205 (2004).
[317] R.T. Cahill, C.D. Roberts, and J. Praschifka, Phys. Rev. D **36**, 2804 (1987).
[318] P. Maris, Few Body Syst. **32**, 41 (2002).
[319] G. Eichmann, I.C. Cloët, R. Alkofer, A. Krassnigg, and C.D. Roberts, Phys. Rev. C **79**, 012202(R) (2009).
[320] G. Eichmann, C.S. Fischer, and H. Sanchis-Alepuz, Phys. Rev. D **94**, 094033 (2016).
[321] Y. Lu *et al.*, Phys. Rev. C **96**, 015208 (2017).
[322] C. Chen *et al.*, Phys. Rev. D **97**, 034016 (2018).
[323] C. Chen, G. I. Krein, C.D. Roberts, S. M. Schmidt, and J. Segovia, Phys. Rev. D **100**, 054009 (2019).
[324] P.-L. Yin *et al.*, Phys. Rev. D **100**, 034008 (2019).
[325] C.D. Roberts, R.J. Holt, and S.M. Schmidt, Phys. Lett. B **727**, 249 (2013).
[326] J. Segovia *et al.*, Few Body Syst. **55**, 1 (2014).
[327] C. Mezrag, J. Segovia, L. Chang, and C.D. Roberts, Phys. Lett. B **783**, 263 (2018).
[328] E.P. Segarra *et al.*, (2019), Flavor dependence of the nucleon valence structure from nuclear deep inelastic scattering data – arXiv:1908.02223 [nucl-th].
[329] C. Alexandrou, Ph. de Forcrand, and B. Lucini, Phys. Rev. Lett. **97**, 222002 (2006).
[330] T. DeGrand, Z. Liu, and S. Schaefer, Phys. Rev. D **77**, 034505 (2008).
[331] R. Babich *et al.*, Phys. Rev. D **76**, 074021 (2007).
[332] Y. Bi *et al.*, Chin. Phys. C **40**, 073106 (2016).
[333] P. Maris, Few Body Syst. **35**, 117 (2004).
[334] H.L.L. Roberts, A. Bashir, L.X. Gutiérrez-Guerrero, C.D. Roberts, and D.J. Wilson, Phys. Rev. C **83**, 065206 (2011).
[335] M. Anselmino, E. Predazzi, S. Ekelin, S. Fredriksson, and D.B. Lichtenberg, Rev. Mod. Phys. **65**, 1199 (1993).
[336] I. Aznauryan, V. Burkert, T.-S. Lee, and V. Mokeev, J. Phys. Conf. Ser. **299**, 012008 (2011).
[337] V.D. Burkert and T.S. H. Lee, Int. J. Mod. Phys. E **13**, 1035 (2004).
[338] R.T. Cahill, C.D. Roberts, and J. Praschifka, Austral. J. Phys. **42**, 129 (1989).
[339] H. Reinhardt, Phys. Lett. B **244**, 316 (1990).
[340] G.V. Efimov, M.A. Ivanov, and V.E. Lyubovitskij, Z. Phys. C **47**, 583 (1990).
[341] G. Eichmann, R. Alkofer, A. Krassnigg, and D. Nicmorus, Phys. Rev. Lett. **104**, 201601 (2010).
[342] S.-X. Qin, C.D. Roberts, and S.M. Schmidt, Few Body Syst. **60**, 26 (2019).
[343] R.G. Edwards, J.J. Dudek, D.G. Richards, and S.J. Wallace, Phys. Rev. D **84**, 074508 (2011).
[344] M. Ripani *et al.*, Phys. Rev. Lett. **91**, 022002 (2003).
[345] V.D. Burkert, EPJ Web Conf. **37**, 01017 (2012).
[346] H. Kamano, S.X. Nakamura, T.S.H. Lee, and T. Sato, Phys. Rev. C **88**, 035209 (2013).
[347] V. Crede and W. Roberts, Rept. Prog. Phys. **76**, 076301 (2013).
[348] V.I. Mokeev, I. Aznauryan, V. Burkert, and R. Gothe, EPJ Web Conf. **113**, 01013 (2016).
[349] H.-X. Chen, W. Chen, X. Liu, and S.-L. Zhu, Phys. Rept. **639**, 1 (2016).
[350] Y.-R. Liu, H.-X. Chen, W. Chen, X. Liu, and S.-L. Zhu, Prog. Part. Nucl. Phys. **107**, 237 (2019).
[351] S.-S. Xu *et al.*, Eur. Phys. J. A **55**, 113 (Lett.) (2019).
[352] E.V. Souza *et al.*, Eur. Phys. J. A in press (2019), arXiv:1909.05875 [nucl-th].
[353] A. Trivedi, Few Body Syst. **60**, 5 (2019).
[354] V.D. Burkert, V.I. Mokeev, and B.S. Ishkhanov, Moscow Univ. Phys. Bull. **74**, 243 (2019), [Vestn. Mosk. Univ. Ser. III Fiz. Astron. **74** (2019) pp.28-38].
[355] H.F. Jones and M.D. Scadron, Annals Phys. **81**, 1 (1973).
[356] S. Capstick and B.D. Keister, Phys. Rev. D **51**, 3598 (1995).
[357] I.G. Aznauryan and V.D. Burkert, Phys. Rev. C **92**, 035211 (2015).
[358] I.G. Aznauryan and V.D. Burkert, arXiv:1603.06692 [hep-ph], (2016).
[359] M.B. Hecht *et al.*, Phys. Rev. C **65**, 055204 (2002).
[360] D.J. Rowe, Rep. Prog. Phys. **48**, 1419 (1985).
[361] T. Dytrych, K.D. Sviratcheva, J.P. Draayer, C. Bahri, and J.P. Vary, J. Phys. G **35**, 123101 (2008).
[362] T. Dytrych *et al.*, Phys. Rev. Lett. **111**, 252501 (2013).
[363] O. Gayou *et al.*, Phys. Rev. C **64**, 038202 (2001).
[364] V. Punjabi *et al.*, Phys. Rev. C **71**, 055202 (2005), [Erratum-ibid. C **71**, 069902 (2005)].
[365] A.J.R. Puckett *et al.*, Phys. Rev. Lett. **104**, 242301 (2010).
[366] A.J.R. Puckett *et al.*, Phys. Rev. C **85**, 045203 (2012).
[367] G.A. Miller, Nucl. Phys. News **18**, 12 (2008).
[368] N. Isgur and G. Karl, Phys. Rev. D **18**, 4187 (1978).
[369] S. Capstick and N. Isgur, Phys. Rev. D **34**, 2809 (1986).
[370] S. Capstick, Phys. Rev. D **46**, 2864 (1992).
[371] S. Capstick and W. Roberts, Phys. Rev. D **49**, 4570 (1994).
[372] M. Ronniger and B.C. Metsch, Eur. Phys. J. A **47**, 162 (2011).
[373] G. Ramalho and M.T. Peña, Phys. Rev. D **84**, 033007 (2011).
[374] B. Golli and S. Širca, Eur. Phys. J. A **49**, 111 (2013).
[375] C. Jayalath, J.L. Goity, E. González de Urreta, and N.N. Scoccola, Phys. Rev. D **84**, 074012 (2011).
[376] C.D. Roberts and A.G. Williams, Prog. Part. Nucl. Phys. **33**, 477 (1994).
[377] C.D. Roberts, Prog. Part. Nucl. Phys. **61**, 50 (2008).
[378] D.J. Wilson, I.C. Cloët, L. Chang, and C.D. Roberts, Phys. Rev. C **85**, 025205 (2012).
[379] C. Chen, L. Chang, C.D. Roberts, S. Wan, and D.J. Wilson, Few Body Syst. **53**, 293 (2012).
[380] U.-G. Meißner and J.A. Oller, Nucl. Phys. A **673**, 311 (2000).
[381] E.E. Kolomeitsev and M.F.M. Lutz, Phys. Lett. B **585**, 243 (2004).
[382] C. García Recio, M.F.M. Lutz, and J. Nieves, Phys. Lett. B **582**, 49 (2004).
[383] M. Döring, E. Oset, and D. Strottman, Phys. Rev. C

73, 045209 (2006).
[384] M. Döring, Nucl. Phys. A **786**, 164 (2007).
[385] M. Döring, E. Oset, and U.-G. Meißner, Eur. Phys. J. A **46**, 315 (2010).
[386] M. Döring and K. Nakayama, Phys. Lett. B **683**, 145 (2010).
[387] B. Borasoy, U.-G. Meißner, and R. Nißler, Phys. Rev. C **74**, 055201 (2006).
[388] M. Mai, P.C. Bruns, and U.-G. Meißner, Phys. Rev. D **86**, 094033 (2012).
[389] A. Gasparyan and M.F.M. Lutz, Nucl. Phys. A **848**, 126 (2010).
[390] E.J. Garzón and E. Oset, Eur. Phys. J. A **48**, 5 (2012).
[391] K.P. Khemchandani, A. Martínez Torres, H. Nagahiro, and A. Hosaka, Int. J. Mod. Phys. Conf. Ser. **26**, 1460060 (2014).
[392] J.-J. Wu, R. Molina, E. Oset, and B.S. Zou, Phys. Rev. C **84**, 015202 (2011).
[393] S. Dürr *et al.*, Science **322**, 1224 (2008).
[394] T. Burch, C. Gattringer, L.Y. Glozman, C. Hagen, D. Hierl, C.B. Lang, and A. Schäfer, Phys. Rev. D **74**, 014504 (2006).
[395] C. Alexandrou *et al.* [European Twisted Mass Collaboration], Phys. Rev. D **78**, 014509 (2008).
[396] J. Bulava, R.G. Edwards, E. Engelson, B. Joo, H-W. Lin, C. Morningstar, D.G. Richards, S.J. Wallace, Phys. Rev. D **82**, 014507 (2010).
[397] B.J. Menadue, W. Kamleh, D.B. Leinweber, and M.S. Mahbub, Phys. Rev. Lett. **108**, 112001 (2012).
[398] W. Melnitchouk *et al.*, Phys. Rev. D **67**, 114506 (2003).
[399] R.G. Edwards, N. Mathur, D.G. Richards, and S.J. Wallace, Phys. Rev. D **87**, 054506 (2013).
[400] G.P. Engel *et al.* (BGR Collaboration), Phys. Rev. D **87**, 074504 (2013).
[401] C.B. Lang and V. Verduci, Phys. Rev. D **87**, 054502 (2013).
[402] C. Pelissier and A. Alexandru, Phys. Rev. D **87**, 014503 (2013).
[403] C. Alexandrou, J.W. Negele, M. Petschlies, A. Strelchenko, and A. Tsapalis, Phys. Rev. D **88**, 031501 (2013).
[404] M. Döring, B. Hu, and M. Mai, Phys. Lett. B **782**, 785 (2018).
[405] M. Mai and M. Döring, Eur. Phys. J. A **53**, 240 (2017).
[406] M. Mai and M. Döring, arXiv:1807.04746 [hep-lat], submitted to Phys. Rev. Lett.
[407] G. Höhler, Landoldt-Börnstein Vol. **I/9b2**, ed. by H. Schopper (Springer-Verlag, Berlin, 1983).
[408] R.E. Cutkosky *et al.*, Phys. Rev. D **20**, 2839 (1979); R.E. Cutkosky in *Proceedings of the 4th Conference on Baryon Resonances*, ed. N. Isgur (Toronto, 1980).
[409] R.A. Arndt, W.J. Briscoe, I.I. Strakovsky, and R.L. Workman, Phys. Rev. C **74**, 045205 (2006).
[410] M. Shrestha and D.M. Manley, Phys. Rev. C **86**, 055203 (2012).
[411] D. Drechsel, S.S. Kamolov, and L. Tiator, Eur. Phys. J. A **34**, 69 (2007).
[412] I. Aznauryan, Phys. Rev. C **67**, 015209 (2003).
[413] R.L. Workman, M.W. Paris, W.J. Briscoe, I.I. Strakovsky, Phys. Rev. C **86**, 015202 (2012).
[414] O. Hanstein, D. Drechsel, L. Tiator, Nucl. Phys. A **632**, 561 (1998).
[415] A.V. Anisovich, R. Beck, E. Klempt, V.A. Nikonov, A.V. Sarantsev, U. Thoma, Eur. Phys. J. A **48**, 15 (2012).
[416] J. Nys, V. Mathieu, C. Fernández-Ramirez, A.N. Hiller Blin, A. Jackura, M. Mikhasenko, A. Pilloni, A.P. Szczepaniak, G. Fox, J. Ryckebusch, Phys. Rev. D **95**, 034014 (2017).
[417] V. Shklyar, H. Lenske, U. Mosel, Phys. Lett. B **650**, 172 (2007).
[418] M. Hilt, B.C. Lehnhart, S. Scherer, and L. Tiator, Phys. Rev. C **88** 055207 (2013).
[419] L. Tiator, R.L. Workman, Y. Wunderlich, and H. Haberzettl, Phys. Rev. C **96**, no. 2, 025210 (2017).
[420] V. Dmitrasinovic, T.W. Donnelly, and F. Gross, in *Research Program at CEBAF (III), RPAC III,* ed. by F. Gross (CEBAF, Newport News, 1988), p.547.
[421] C. Carlson, Phys. Rev. D **34**, 2704 (1986).
[422] S.X. Nakamura, H. Kamano, and T. Sato, Phys. Rev. D **92**, 074024 (2015).
[423] P.E. Bosted *et al.* [CLAS Collaboration], Phys. Rev. C **95**, 035207 (2017)
[424] P.E. Bosted *et al.* [CLAS Collaboration], Phys. Rev. C **95**, no. 3, 035206 (2017)
[425] X. Zheng *et al.* [CLAS Collaboration], Phys. Rev. C **94**, no. 4, 045206 (2016).
[426] S. Stajner *et al.*, Phys. Rev. Lett. **119**, no. 2, 022001 (2017).
[427] H. Merkel *et al.* [A1 Collaboration], Phys. Rev. Lett. **99**, 132301 (2007).
[428] P. Achenbach *et al.* [A1 Collaboration], Eur. Phys. J. A **53**, no. 10, 198 (2017).
[429] R. Nasseripour *et al.* [CLAS Collaboration], Phys. Rev. C **77**, 065208 (2008).
[430] V. Mokeev (JLab), private communication.
[431] R.A. Thompson *et al.* [CLAS Collaboration], Phys. Rev. Lett. **86**, 1702 (2001).
[432] M. Gabrielyan *et al.* [CLAS Collaboration], Phys. Rev. C **90**, 035202 (2014).
[433] D.S. Carman *et al.* [CLAS Collaboration], Phys. Rev. C **87**, 025204 (2013).
[434] D.S. Carman *et al.* [CLAS Collaboration], Phys. Rev. C **79**, 065205 (2009).
[435] P. Ambrozewicz *et al.* [CLAS Collaboration], Phys. Rev. C **75**, 045203 (2007).
[436] D.S. Carman *et al.* [CLAS Collaboration], Phys. Rev. Lett. **90**, 131804 (2003).
[437] The online SAID facility provides data bases and analyses in a web-site based format (`http://gwdac.phys.gwu.edu`) and via ssh (ssh -X said@said.phys.gwu.edu).
[438] R. Gothe *et al.*, Proposal E12-09-003 approved by the PAC34 committee, `https://www.jlab.org/exp_prog/proposals/09/PR12-09-003.pdf`.
[439] D.S. Carman *et al.*, approved run group proposal E12-06-108A, `https://www.jlab.org/exp_prog/proposals/14/E12-06-108A.pdf`.
[440] D.S. Carman *et al.*, approved run group proposal E12-16-010A, `https://misportal.jlab.org/pacProposals/proposals/1263/attachments/92759/Proposal.pdf`.
[441] B. Julia-Díaz, H. Kamano, T.-S.H. Lee, A. Matsuyama, T. Sato, and N. Suzuki, Phys. Rev. C **80**, 025207 (2009).
[442] L. Tiator, M. Döring, R.L. Workman, M. Hadžimehmedović, H. Osmanović, R. Omerović, J. Stahov, and A. Švarc, Phys. Rev. C **94**, no. 6, 065204 (2016).
[443] R.A. Arndt, I.I. Strakovsky, and R.L. Workman, PiN

Newsletter **16**, 150 (2002).
[444] W.-T. Chiang, S.N. Yang, L. Tiator, and D. Drechsel, Nucl. Phys. A **700**, 429 (2002).
[445] T. Corthals, T. Van Cauteren, P. Van Craeyveld, J. Ryckebusch, and D.G. Ireland, Phys. Lett. B **656**, 186 (2007).
[446] M. Vanderhaeghen, M. Guidal, and J.M. Laget, Phys. Rev. C **57**, 1454 (1998).
[447] T. Vrancx, J. Ryckebusch, and J. Nys, Phys. Rev. C **89**, 065202 (2014).
[448] H. Haberzettl, X.-Y. Wang, and J. He, Phys. Rev. C **92**, 055503 (2015)
[449] T. Mart, C. Bennhold, and H. Haberzettl, PiN Newsletter **16**, 86 (2002).
[450] O.V. Maxwell, Phys. Rev. C **90**, 034605 (2014).
[451] I.G. Aznauryan, V.D. Burkert, G.V. Fedotov, B.S. Ishkhanov, and V.I. Mokeev, Phys. Rev. C **72**, 045201 (2005).
[452] E.L. Isupov *et al.* [CLAS Collaboration], Phys. Rev. C **96**, no. 2, 025209 (2017).
[453] T.A. Gail and T.R. Hemmert, Eur. Phys. J. A **28**, 91 (2006)
[454] M. Dorati, T.A. Gail, and T.R. Hemmert, PoS LATTICE **2007**, 071 (2007)
[455] M. Döring, D. Jido, and E. Oset, Eur. Phys. J. A **45**, 319 (2010)
[456] D. Jido, M. Döring, and E. Oset, Phys. Rev. C **77**, 065207 (2008)
[457] M. Hilt, T. Bauer, S. Scherer, and L. Tiator, Phys. Rev. C **97**, 035205 (2018).
[458] T. Bauer, S. Scherer, and L. Tiator, Phys. Rev. C **90**, no. 1, 015201 (2014).
[459] P.T. Mattione *et al.* [CLAS Collaboration], Phys. Rev. C **96**, 035204 (2017).
[460] D. Ho *et al.* [CLAS Collaboration], Phys. Rev. Lett. **118**, no. 24, 242002 (2017)
[461] P. Collins *et al.* [CLAS Collaboration and M. Döring, D. Ronchen, D. Sadasivan], Phys. Lett. B **771**, 213 (2017)
[462] D. Ronchen, M. Döring, and U.G. Meissner, Eur. Phys. J. A **54**, no. 6, 110 (2018).
[463] A.V. Anisovich *et al.*, Eur. Phys. J. A **52**, no. 9, 284 (2016).
[464] R.L. Workman, L. Tiator, Y. Wunderlich, M. Döring, and H. Haberzettl, Phys. Rev. C **95**, no. 1, 015206 (2017).
[465] Y. Wunderlich, A. Švarc, R.L. Workman, L. Tiator, and R. Beck, Phys. Rev. C **96**, 025210 (2017).
[466] A. Švarc, Y. Wunderlich, H. Osmanović, M. Hadžimehmedović, R. Omerović, J. Stahov, V. Kashevarov, K. Nikonov, M. Ostrich, L. Tiator, and R. Workman, Phys. Rev. C **97**, 054611 (2018).
[467] J. Nys, A.N. Hiller Blin, V. Mathieu, C. Fernandez-Ramirez, A. Jackura, A. Pilloni, J. Ryckebusch, A.P. Szczepaniak, and G. Fox [JPAC Collaboration], Phys. Rev. D **98**, 034020 (2018).
[468] V. Mathieu, J. Nys, A. Pilloni, C. Fernández-Ramirez, A. Jackura, M. Mikhasenko, V. Pauk, A.P. Szczepaniak, G. Fox, 1708.07779, (2018).
[469] V. Mathieu, M. Albaladejo, C. Fernández-Ramírez, A.W. Jackura, M. Mikhasenko, A. Pilloni, and A.P. Szczepaniak, Phys. Rev. D **100**, 054017 (2019).
[470] [JPAC Collaboration] and A. Rodas, A. Pilloni, M. Albaladejo, C. Fernandez-Ramirez, A. Jackura, V. Mathieu, M. Mikhasenko, J. Nys, V. Pauk, B. Ketzer, and A. Szczepaniak, Phys. Rev. Lett. **122**, 042002 (2018).
[471] [LHCb Collaboration], Phys. Rev. Lett. **122**, 222001 (2019).
[472] A.N. Hiller Blin, C. Fernández-Ramírez, A. Jackura, V. Mathieu, V.I. Mokeev, A. Pilloni, and A.P. Szczepaniak, Phys. Rev. D **94**, 034002 (2016).
[473] [JPAC Collaboration] and D. Winney, C. Fanelli, A. Pilloni, A.N. Hiller Blin, C. Fernandez-Ramirez, M. Albaladejo, V. Mathieu, V.I. Mokeev, and A.P. Szczepaniak, Phys. Rev. D **100**, 034019 (2019).
[474] Xiangdong Ji, Sci. China Phys. Mech. Astron. **57**, 1407 (2014).
[475] Keh-Fei Liu, Proceedings, 33rd International Symposium on Lattice Field Theory (Lattice 2015): Kobe, Japan, July 14-18, 2015, PoS LATTICE2015, 115 (2016).
[476] K. Orginos, A. Radyushkin, J. Karpie, and S. Zafeiropoulous, Phys. Rev. D **96**, 095403 (2017).
[477] Yan-Qing Ma and Jian-Wei Qui, Phys. Rev. Lett. **120**, 022003 (2018).
[478] B. Joo *et al.*, JHEP **12**, 81 (2019).
[479] T. Izubuchi *et al.*, Phys. Rev. D **100**, 034516 (2019).
[480] M. Luscher, Nucl. Phys. B **354**, 531 (1991).
[481] M.T. Hansen and S.R. Sharpe, Phys. Rev. D **86**, 016007 (2012).
[482] R.A. Briceno and Z. Davoudi, Phys. Rev. D **87**, 094507 (2013).
[483] R.A. Briceno and M.T. Hansen, Phys. Rev. D **94**, 013008 (2016).
[484] R.A. Briceno *et al.*, Phys. Rev. D **97**, 054513 (2018).
[485] R.A. Briceno *et al.*, Phys. Rev. D **93**, 114508 (2016).
[486] C.W. Andersen, J. Bulava, B. Horz, and C. Morningstar, Phys. Rev. D **97**, 014506 (2018).
[487] W. Detmold *et al.*, Eur. Phys. J A **55**, 193 (2019).
[488] B. Joo *et al.* [USQCD Collaboration], Eur. Phys J. A **55**, 199 (2019).
[489] L.D. Faddeev, Sov. Phys. JETP **12**, 1014 (1961), [Zh. Eksp. Teor. Fiz. **39** (1960) 1459].
[490] S.-X. Qin, C.D. Roberts, and S.M. Schmidt, Phys. Rev. D **97**, 114017 (2018).
[491] S.-x. Qin, L. Chang, Y.-X. Liu, C.D. Roberts, and D.J. Wilson, Phys. Rev. C **85**, 035202 (2012).
[492] M.S. Bhagwat, M.A. Pichowsky, C.D. Roberts, and P.C. Tandy, Phys. Rev. C **68**, 015203 (2003).
[493] P.O. Bowman *et al.*, Phys. Rev. D **71**, 054507 (2005).
[494] M.S. Bhagwat and P.C. Tandy, AIP Conf. Proc. **842**, 225 (2006).
[495] M. Gell-Mann, Phys. Lett. **8**, 214 (1964).
[496] G. Zweig, (1964), An $SU(3)$ model for strong interaction symmetry and its breaking. Parts 1 and 2 (CERN Reports No. 8182/TH. 401 and No. 8419/TH. 412).
[497] Q.-W. Wang, S.-X. Qin, C.D. Roberts, and S.M. Schmidt, Phys. Rev. D **98**, 054019 (2018).
[498] T. Bhattacharya *et al.*, Phys. Rev. D **94**, 054508 (2016).
[499] S.-S. Xu *et al.*, Phys. Rev. D **92**, 114034 (2015).
[500] H. He and X. Ji, Phys. Rev. D **52**, 2960 (1995).
[501] V.M. Braun *et al.*, Phys. Rev. D **89**, 094511 (2014).
[502] G.S. Bali *et al.*, JHEP **02**, 070 (2016).
[503] L. Chang *et al.*, Phys. Rev. Lett. **110**, 132001 (2013).
[504] C. Shi *et al.*, Phys. Rev. D **92**, 014035 (2015).
[505] V.M. Braun *et al.*, Phys. Rev. D **92**, 014504 (2015).
[506] F. Gao, L. Chang, and Y.-X. Liu, Phys. Lett. B **770**, 551 (2017).
[507] J.-H. Zhang, J.-W. Chen, X. Ji, L. Jin, and H.-W. Lin,

Phys. Rev. D **95**, 094514 (2017).
[508] J.-H. Zhang *et al.*, Nucl. Phys. B **B939**, 429 (2019).
[509] B.L. Li *et al.*, Phys. Rev. D **93**, 114033 (2016).
[510] B.-L. Li, L. Chang, M. Ding, C.D. Roberts, and H.-S. Zong, Phys. Rev. D **94**, 094014 (2016).
[511] M.K. Jones *et al.*, Phys. Rev. Lett. **84**, 1398 (2000).
[512] O. Gayou *et al.*, Phys. Rev. Lett. **88**, 092301 (2002).
[513] G. Cates, C. de Jager, S. Riordan, and B. Wojtsekhowski, Phys. Rev. Lett. **106**, 252003 (2011).
[514] C.F. Perdrisat, V. Punjabi, and M. Vanderhaeghen, Prog. Part. Nucl. Phys. **59**, 694 (2007).
[515] A. Akhiezer and M. Rekalo, Sov. J. Part. Nucl. **4**, 277 (1974), [Fiz. Elem. Chast. Atom. Yadra **4**, 662 (1973)].
[516] R. Arnold, C.E. Carlson, and F. Gross, Phys. Rev. C **23**, 363 (1981).
[517] J.J. Kelly, Phys. Rev. C **70**, 068202 (2004).
[518] R. Bradford, A. Bodek, H.S. Budd, and J. Arrington, Nucl. Phys. Proc. Suppl. **159**, 127 (2006).
[519] Y.-Z. Xu *et al.*, Phys. Rev. D **100**, 114038 (2019).
[520] S.J. Brodsky and J.R. Hiller, Phys. Rev. D **46**, 2141 (1992).
[521] H. Haberzettl, Phys. Rev. D **100**, 036008 (2019).
[522] J. Singh, Phys. Rev. D **31**, 1097 (1985).
[523] P.J.A. Bicudo, J.E. F.T. Ribeiro, and R. Fernandes, Phys. Rev. C **59**, 1107 (1999).
[524] L. Chang, Y.-X. Liu, and C.D. Roberts, Phys. Rev. Lett. **106**, 072001 (2011).
[525] J.-J. Wu, T.S.H. Lee, and B.-S. Zou, arXiv:1906.05375 [nucl-th].
[526] R. Wang and X. Chen, arXiv:1912.12040 [hep-ph], Extraction of QCD trace anomaly of proton from near threshold J/ψ photoproduction data at JLab.
[527] Y. Tian and R.W. Gothe, Few Body Syst. **59**, 130 (2018).
[528] L. Schlessinger and C. Schwartz, Phys. Rev. Lett. **16**, 1173 (1966).
[529] L. Schlessinger, Phys. Rev. **167**, 1411 (1968).
[530] R.A. Tripolt, I. Haritan, J. Wambach, and N. Moiseyev, Phys. Lett. B **774**, 411 (2017).
[531] D. Binosi and R.-A. Tripolt, Phys. Lett. B **801**, 135171 (2020).
[532] P. Maris and C.D. Roberts, Phys. Rev. C **58**, 3659 (1998).
[533] E. Witten, Nucl. Phys. B **160**, 57 (1979).
[534] E. Witten, Nucl. Phys. B **223**, 433 (1983).
[535] D. Diakonov, V.Y. Petrov, and P.V. Pobylitsa, Nucl. Phys. B **306**, 809 (1988).
[536] C.V. Christov, A. Blotz, H.-Ch. Kim, P. Pobylitsa, T. Watabe, T. Meissner, E. Ruiz Arriola, and K. Goeke, Prog. Part. Nucl. Phys. **37**, 91 (1996).
[537] D. Diakonov, hep-ph/9802298.
[538] D. Diakonov and V.Y. Petrov, Nucl. Phys. B **272**, 457 (1986).
[539] D. Diakonov, V. Petrov, P. Pobylitsa, M.V. Polyakov, and C. Weiss, Nucl. Phys. B **480**, 341 (1996).
[540] G.S. Yang, H.-Ch. Kim, M.V. Polyakov, and M. Praszaowicz, Phys. Rev. D **94**, 071502 (2016).
[541] D. Diakonov, arXiv:1003.2157 [hep-ph].
[542] N. Isgur and M.B. Wise, Phys. Lett. B **232**, 113 (1989).
[543] N. Isgur and M.B. Wise, Phys. Rev. Lett. **66**, 1130 (1991).
[544] H. Georgi, Phys. Lett. B **240**, 447 (1990).
[545] A.V. Manohar and M.B. Wise, Camb. Monogr. Part. Phys. Nucl. Phys. Cosmol. **10**, 1 (2000).
[546] J.Y. Kim, H.-Ch. Kim, and G.S. Yang, Phys. Rev. D **98**, no. 5, 054004 (2018).
[547] J.Y. Kim and H.-Ch. Kim, arXiv:1909.00123 [hep-ph].
[548] H.-Ch. Kim, J. Korean Phys. Soc. **73**, no. 2, 165 (2018).
[549] A. Blotz, D. Diakonov, K. Goeke, N.W. Park, V. Petrov, and P.V. Pobylitsa, Nucl. Phys. A **555**, 765 (1993).
[550] G.S. Yang and H.-Ch. Kim, Prog. Theor. Phys. **128**, 397 (2012).
[551] H.-Ch. Kim, A. Blotz, M.V. Polyakov, and K. Goeke, Phys. Rev. D **53**, 4013 (1996).
[552] A. Silva, D. Urbano, T. Watabe, M. Fiolhais, and K. Goeke, Nucl. Phys. A **675**, 637 (2000).
[553] T. Ledwig, A. Silva, and M. Vanderhaeghen, Phys. Rev. D **79**, 094025 (2009).
[554] J.Y. Kim and H.-Ch. Kim, Eur. Phys. J. C **79**, no. 7, 570 (2019).
[555] H.-Ch. Kim, M. Polyakov, M. Praszalowicz, G.S. Yang, and K. Goeke, Phys. Rev. D **71**, 094023 (2005).
[556] A. Silva, H.-Ch. Kim, D. Urbano, and K. Goeke, Phys. Rev. D **72**, 094011 (2005).
[557] T. Ledwig, H.-Ch. Kim, and K. Goeke, Phys. Rev. D **78**, 054005 (2008).
[558] A. Silva, H.C. Kim, and K. Goeke, Phys. Rev. D **65**, 014016 (2002), Erratum: [Phys. Rev. D **66**, 039902 (2002)].
[559] A. Silva, H.-Ch. Kim, D. Urbano, and K. Goeke, Phys. Rev. D **74**, 054011 (2006).
[560] A. Silva, D. Urbano, and H.-Ch. Kim, PTEP **2018**, no. 2, 023D01 (2018).
[561] H.-Ch. Kim, M.V. Polyakov, and K. Goeke, Phys. Rev. D **53**, 4715 (1996).
[562] H.-Ch. Kim, M.V. Polyakov, and K. Goeke, Phys. Lett. B **387**, 577 (1996).
[563] T. Ledwig, A. Silva, and H.C. Kim, Phys. Rev. D **82**, 034022 (2010).
[564] T. Ledwig, A. Silva, and H.-Ch. Kim, Phys. Rev. D **82**, 054014 (2010).
[565] T. Ledwig and H.-Ch. Kim, Phys. Rev. D **85**, 034041 (2012).
[566] K. Goeke *et al.*, Phys. Rev. D **75**, 094021 (2007).
[567] H.-Ch. Kim, M. Praszalowicz, and K. Goeke, Phys. Rev. D **61**, 114006 (2000).
[568] T. Ledwig, A. Silva, H.-Ch. Kim, and K. Goeke, JHEP **0807**, 132 (2008).
[569] G.S. Yang and H.-Ch. Kim, Phys. Rev. C **92**, 035206 (2015).
[570] D. Diakonov, V.Y. Petrov, P.V. Pobylitsa, M.V. Polyakov, and C. Weiss, Phys. Rev. D **56**, 4069 (1997).
[571] A.V. Efremov, K. Goeke, and P. Schweitzer, Eur. Phys. J. C **35**, 207 (2004).
[572] A.V. Efremov, K. Goeke, M.V. Polyakov, and D. Urbano, Phys. Lett. B **478**, 94 (2000).
[573] H.D. Son, A. Tandogan, and M.V. Polyakov, arXiv:1911.01955 [hep-ph].
[574] J.Y. Kim and H.-Ch. Kim, Phys. Rev. D **97**, no. 11, 114009 (2018).
[575] J.Y. Kim and H.-Ch. Kim, arXiv:1912.01437 [hep-ph].
[576] H.-Ch. Kim, M.V. Polyakov, and M. Praszaowicz, Phys. Rev. D **96**, no. 1, 014009 (2017), Addendum: [Phys. Rev. D **96**, no. 3, 039902 (2017)]
[577] H.-Ch. Kim, M.V. Polyakov, M. Praszałowicz, and G.S. Yang, Phys. Rev. D **96**, no. 9, 094021 (2017), Erratum: [Phys. Rev. D **97**, no. 3, 039901 (2018)].
[578] K. Goeke, M.V. Polyakov, and M. Vanderhaeghen,

Prog. Part. Nucl. Phys. **47**, 401 (2001).
[579] D. Diakonov, V. Petrov, and A.A. Vladimirov, Phys. Rev. D **88**, no. 7, 074030 (2013).
[580] B. Golli, W. Broniowski, and G. Ripka, Phys. Lett. B **437**, 24 (1998).
[581] G.F. de Téramond and S.J. Brodsky, Phys. Rev. Lett. **102**, 081601 (2009).
[582] S.J. Brodsky, G.F. de Téramond, and H.G. Dosch, Phys. Lett. B **729**, 3 (2014).
[583] G.F. de Téramond, H.G. Dosch, and S.J. Brodsky, Phys. Rev. D **91**, no. 4, 045040 (2015).
[584] H.G. Dosch, G.F. de Téramond, and S.J. Brodsky, Phys. Rev. D **91**, no. 8, 085016 (2015).
[585] S.J. Brodsky, H.C. Pauli, and S.S. Pinsky, Phys. Rept. **301**, 299 (1998).
[586] S.J. Brodsky, G.F. de Téramond, H.G. Dosch, and J. Erlich, Phys. Rept. **584**, 1 (2015).
[587] L. Zou and H.G. Dosch, arXiv:1801.00607 [hep-ph].
[588] E. Witten, Nucl. Phys. B **188**, 513 (1981).
[589] J. Polchinski and M.J. Strassler, Phys. Rev. Lett. **88**, 031601 (2002).
[590] S.J. Brodsky and G.R. Farrar, Phys. Rev. Lett. **31**, 1153 (1973).
[591] V.A. Matveev, R.M. Muradian, and A.N. Tavkhelidze, Lett. Nuovo Cim. **7**, 719 (1973).
[592] J. Polchinski and M.J. Strassler, JHEP **0305**, 012 (2003).
[593] S.D. Drell and T.M. Yan, Phys. Rev. Lett. **24**, 181 (1970).
[594] G.B. West, Phys. Rev. Lett. **24**, 1206 (1970).
[595] P.A.M. Dirac, Rev. Mod. Phys. **21**, 392 (1949).
[596] S.J. Brodsky and G.F. de Téramond, Phys. Rev. Lett. **96**, 201601 (2006).
[597] D.E. Soper, Phys. Rev. D **15**, 1141 (1977).
[598] M. Burkardt, Phys. Rev. D **62**, 071503 (2000); Phys. Rev. D **66**, 119903 (2002).
[599] S.J. Brodsky and G.F. de Téramond, Phys. Rev. D **78**, 025032 (2008).
[600] G.F. de Téramond and S.J. Brodsky, AIP Conf. Proc. **1296**, 128 (2010).
[601] G.F. de Téramond, H.G. Dosch, and S.J. Brodsky, Phys. Rev. D **87**, 075005 (2013).
[602] P. Breitenlohner and D.Z. Freedman, Annals Phys. **144**, 249 (1982).
[603] I. Kirsch, JHEP **0609**, 052 (2006).
[604] Z. Abidin and C.E. Carlson, Phys. Rev. D **79**, 115003 (2009).
[605] V. de Alfaro, S. Fubini, and G. Furlan, Nuovo Cim. A **34**, 569 (1976).
[606] A. Karch, E. Katz, D.T. Son, and M.A. Stephanov, Phys. Rev. D **74**, 015005 (2006).
[607] S. Fubini and E. Rabinovici, Nucl. Phys. B **245**, 17 (1984).
[608] Long before the advent of supersymmetry Miyazawa [609] postulated a symmetry between baryons and mesons based on the quark model. But it could not explain the large mass differences of the lowest lying meson and baryon states.
[609] H. Miyazawa, Prog. Theor. Phys. **36**, 1266 (1966).
[610] S.J. Brodsky, G.F. de Téramond, H.G. Dosch, and C. Lorcé, Phys. Lett. B **759**, 171 (2016).
[611] S.J. Brodsky and G.F. de Téramond, Proceedings of the International School of Subnuclear Physics, Vol. **45** (World Scientific Publishing Co., 2009), arXiv:0802.0514 [hep-ph].
[612] It is interesting to note that in Ref.[613] mesons, baryons and tetraquarks belong to the same multiplet.
[613] S. Catto and F. Gursey, Nuovo Cim. A **86**, 201 (1985).
[614] L. Zou, H.G. Dosch, G.F. de Téramond, and S.J. Brodsky, Phys. Rev. D **99**, 114024 (2019).
[615] H.G. Dosch, G.F. de Téramond, and S.J. Brodsky, Phys. Rev. D **92**, no. 7, 074010 (2015).
[616] H.G. Dosch, G.F. de Téramond, and S.J. Brodsky, Phys. Rev. D **95**, no. 3, 034016 (2017).
[617] M. Nielsen and S.J. Brodsky, Phys. Rev. D **97**, no. 11, 114001 (2018).
[618] M. Nielsen, S.J. Brodsky, G.F. de Téramond, H.G. Dosch, F.S. Navarra, and L. Zou, Phys. Rev. D **98**, no. 3, 034002 (2018).
[619] S.J. Brodsky, G.F. de Téramond, and A. Deur, Phys. Rev. D **81**, 096010 (2010).
[620] A. Deur, S.J. Brodsky, and G.F. de Téramond, Phys. Lett. B **750**, 528 (2015).
[621] A. Deur, S.J. Brodsky, and G.F. de Téramond, Phys. Lett. B **757**, 275 (2016).
[622] A. Deur, S.J. Brodsky, and G.F. de Téramond, J. Phys. G **44**, 105005 (2017).
[623] R.S. Sufian, G.F. de Téramond, S.J. Brodsky, A. Deur, and H.G. Dosch, Phys. Rev. D **95**, no. 1, 014011 (2017).
[624] G.F. de Téramond, T. Liu, R.S. Sufian, H.G. Dosch, S.J. Brodsky, and A. Deur, Phys. Rev. Lett. **120**, 182001 (2018).
[625] T. Liu, R.S. Sufian, G.F. de Téramond, H.G. Dosch, S.J. Brodsky, and A. Deur, Phys. Rev. Lett. **124**, no. 8, 082003 (2020).
[626] G. Veneziano, Nuovo Cim. A **57**, 190 (1968).
[627] M. Ademollo and E. Del Giudice, Nuovo Cim. A **63**, 639 (1969).
[628] P.V. Landshoff and J.C. Polkinghorne, Nucl. Phys. B **19**, 432 (1970).
[629] R.S. Sufian, T. Liu, G.F. de Téramond, H.G. Dosch, S.J. Brodsky, A. Deur, M.T. Islam, and B.Q. Ma, Phys. Rev. D **98**, no. 11, 114004 (2018).
[630] R.S. Sufian *et al.*, arXiv:2003.01078 [hep-lat].
[631] S.J. Brodsky, F.G. Cao, and G.F. de Téramond, Phys. Rev. D **84**, 075012 (2011).
[632] G.F. de Téramond and S.J. Brodsky, AIP Conf. Proc. **1432**, no. 1, 168 (2012).
[633] G. Ramalho and D. Melnikov, Phys. Rev. D **97**, 034037 (2018).
[634] R.D. Ball *et al.* [NNPDF Collaboration], J. High Energy Phys. **04**, 040 (2015).
[635] L.A. Harland-Lang, A.D. Martin, P. Motylinski, and R.S. Thorne, Eur. Phys. J. C **75**, 204 (2015).
[636] S. Dulat *et al.*, Phys. Rev. D **93**, 033006 (2016).
[637] E.R. Nocera, R.D. Ball, S. Forte, G. Ridolfi, and J. Rojo, Nucl. Phys. B **887**, 276 (2014).
[638] X. Zheng *et al.* [Jefferson Lab Hall A Collaboration], Phys. Rev. Lett. **92**, 012004 (2004).
[639] X. Zheng *et al.* [Jefferson Lab Hall A Collaboration], Phys. Rev. C **70**, 065207 (2004).
[640] D.S. Parno *et al.* [Jefferson Lab Hall A Collaboration], Phys. Lett. B **744**, 309 (2015).
[641] K.V. Dharmawardane *et al.* [CLAS Collaboration], Phys. Lett. B **641**, 11 (2006).
[642] A. Airapetian *et al.* [HERMES Collaboration], Phys. Rev. Lett. **92**, 012005 (2004).
[643] A. Airapetian *et al.* [HERMES Collaboration], Phys.

Rev. D **71**, 012003 (2005).
[644] M.G. Alekseev *et al.* [COMPASS Collaboration], Phys. Lett. B **693**, 227 (2010).
[645] JLab experiment E12-06-110, spokespersons: X. Zheng (contact), G. Cates, J.-P. Chen, and Z.-E. Meziani.
[646] JLab experiment E12-06-122, spokespersons: B. Wojtsekhowski (contact), J. Annand, T. Averett, G. Cates, N. Liyanage, G. Rosner, and X. Zheng.
[647] C. Adolph *et al.*, Phys. Lett. B **740**, 303 (2015).
[648] A. Rodas *et al.*, Phys. Rev. Lett. **122**, 04002 (2019).
[649] P. Guo *et al.*, Phys. Rev. D **78**, 056003 (2008).
[650] A. Esposito, A. Pilloni, and A.D. Polosa, Phys. Rept. **668**, 1 (2017).
[651] X.-D. Ji, Phys. Rev. D **52**, 271 (1995).
[652] C.D. Roberts, Few Body Syst. **58**, 5 (2017).
[653] C. Lorcé, Eur. Phys. J. C **78**, 120 (2018).
[654] D. Kharzeev, Quarkonium interactions in QCD, nucl-th/9601029.
[655] D. Kharzeev, H. Satz, A. Syamtomov, and G. Zinovjev, J/ψ photoproduction and the gluon structure of the nucleon, Eur. Phys. J. C **9**, 459 (1999).
[656] JLab E12-12-006, K. Hafidi, Z.E. Meziani, X. Qian, and Z. Zhao and SoLID Collaboration, "Near Threshold Electroproduction of J/ψ at 11 GeV", (2012).
[657] JLab E12-12-001, P. Nadel-Turonski, M. Guidal, T. Horn, R. Paremuzyan, and S. Stepanyan and CLAS Collaboration, "Timelike Compton Scattering and J/ψ photoproduction on the proton in e^+e^- pair production with CLAS12 at 11 GeV ", (2012).
[658] S. Joosten and Z.E.Meziani, PoS QCDEV2017 (2018) 017, hep-ex/1802.02616.
[659] `https://indico.cern.ch/event/880248/`
[660] Jefferson Lab Experiment E12-10-007 [SoLID Collaboration], P. Souder, spokesperson.
[661] V. Sulkosky *et al*, Phys. Lett. B **805**, 135428 (2020).
[662] J.-P. Chen, Int. J. Mod. Phys. E **19**, 1893 (2010).
[663] S.J. Brodsky, P. Hoyer, C. Peterson, and N. Saklai, Phys. Lett. B **93**, 451 (1980).
[664] S.J. Brodsky and B.Q. Ma, Phys. Lett. B **381**, 317 (1996).